Chapter 8
Carbon Nanomaterials Derived from Graphene and Graphene Oxide Nanosheets

Ling Bing Kong, Wenxiu Que, Kun Zhou, Sean Li and Tianshu Zhang

8.1 Brief Introduction

Graphene is one of the hottest two-dimensional (2D) materials, which has attracted much attention all around the world and was first used to stand for isolated single atom thick carbon sheet [1], while it now represents all 2D carbon materials with sheet-like or flake-like structures [2, 3]. Besides monolayer (single atomic layer) graphene, ultrathin multilayered carbon materials derived from graphite through exfoliation are also called graphene or graphene-based materials. Furthermore, graphene oxide and various chemically modified graphenes have emerged abruptly [3]. Graphene and graphene oxide have been developed into various one-dimensional (1D),

L.B. Kong (✉)
School of Materials Science and Engineering, Nanyang Technological University, 50 Nanyang Avenue, 639798 Singapore, Singapore
e-mail: elbkong@ntu.edu.sg

W. Que (✉)
Electronic Materials Research Laboratory, School of Electronic and Information Engineering, Xi'an Jiaotong University, 710049 Xi'an, Shaanxi, People's Republic of China
e-mail: wxque@xjtu.edu.cn

K. Zhou
School of Mechanical & Aerospace Engineering, Nanyang Technological University, 639798 Singapore, Singapore
e-mail: kzhou@ntu.edu.sg

S. Li
School of Materials Science and Engineering, The University of New South Wales, Sydney, Australia
e-mail: sean.li@unsw.edu.au

T. Zhang
Anhui Target Advanced Ceramics Technology Co. Ltd., Hefei, Anhui, People's Republic of China
e-mail: 13335516617@163.com

Z.H. Khan (ed.), *Recent Trends in Nanomaterials*,
Advanced Structured Materials 83, DOI 10.1007/978-981-10-3842-6_8

two-dimensional (2D), and three-dimensional (3D) architectures [4, 5]. Among them, 1D structures are also known as fibers or yarns, while 2D ones are called papers or sheets.

Graphene fibers (GFs) have been fabricated by using various methods. They have numerous unique properties, such as high mechanical flexibility, low density, and potential functionalization capability [6]. These special properties make them potential candidates for various applications in different areas, such as photovoltaic cells, supercapacitors, flexible fiber-type actuators, and so on. Graphene-based 2D materials have been reported in the open literature [7–9].

Besides, some applications, e.g., energy storage, environmental protection, and biological issues, required 3D structures [10–13]. The 3D structured graphene materials could have high specific surface areas, strong mechanical properties and rapid mass, and charge transport kinetics, due to the synergistic effect of the 3D porous structures and the intrinsic high conductivity of graphene. 3D graphene structures have also various other names, such as networks, foams, sponges, hydrogels, and aerogels, which will not be specifically emphasized in this chapter and just follow the original references.

8.2 Graphene Fibers (1D)

8.2.1 Solution Processing from Graphene Oxide (GO)

It was found that liquid crystals (LCs) could be formed in suspensions of soluble chemically oxidized graphene or GO nanosheets, which follow a twist-grain-boundary (TGB) phase-like model, with simultaneous lamellar ordering and long-range helical frustrations, so that they can be continuously spun into macroscopic GO fibers [14–17]. The presence of the lamellar structures makes the GO LCs to achieve concentrations that are sufficiently high for efficient alignment and effective coagulation. For instance, a simple syringe injection method has been developed to fabricate GO fibers, which were through 5 wt% NaOH–methanol solution as the coagulation bath [14]. GFs could be obtained by simply reducing the GO fibers in hydroiodic acid. The GFs exhibited a mechanical strength of 140 MPa at an ultimate elongation of 5.8% and a high conductivity of 2.5×10^4 S m^{-1}. In addition, the GFs displayed high mechanical flexibility, so that they could be used to fabricate special patterns and complex textiles.

Experimental results indicated that concentration of the GO LCs played a crucial role in determining whether fibers could be spun out or not [14]. For example, the GO LCs with a concentration of 0.76 led to brittle fibers, while the 2.0% samples were collapsed belts. To obtain continuous fibers, the LC dispersions should have a sufficiently high concentration, e.g., $\varphi = 5.7\%$. In addition, diameters of the fibers could be controlled in the range 50–100 μm, while the spinning rate was hundreds of centimeters per minute, by adjusting the size of nozzle and the drawing speed,

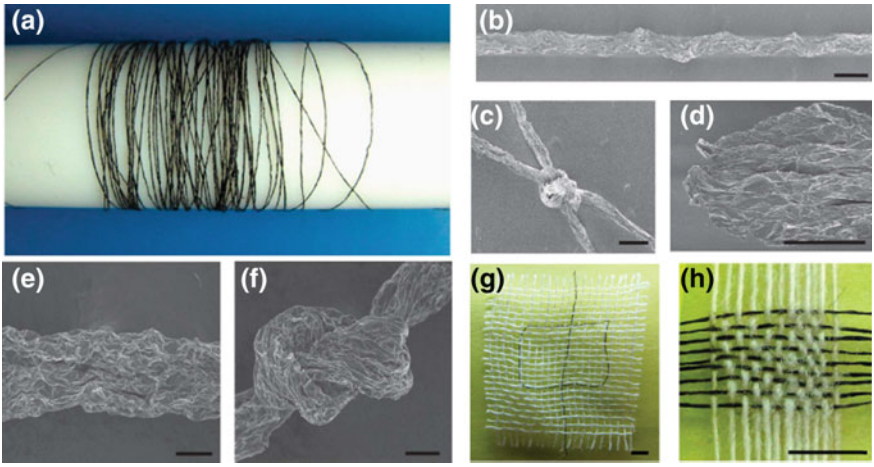

Fig. 8.1 Macroscopic GO fibers and chemically reduced graphene fibers. **a** Photograph of four-meter-long GO fiber wound on a Teflon drum (diameter = 2 cm). **b** SEM image of the fiber and **c** typical tighten knots. **d** Fracture morphology of the GO fiber after tensile tests. The surface-winkled morphology (**e**) and the tighten knot (**f**) of the graphene fiber. **j** A Chinese character ('中', Zhong) pattern knitted in the cotton network (*white*) using two graphene fibers (*black*). **k** A mat of graphene fibers (*horizontal*) woven together with cotton threads (*vertical*). Scale bars = 50 μm (**b**–**f**) and 2 mm (**g**, **h**). Reproduced with permission from [14], Copyright © 2011, Macmillan Publishers Limited

with examples shown in Fig. 8.1a, b. Figure 8.1c demonstrated that the fibers were not broken as the knots were tightened. As compared to the traditional carbon fibers, the GO fibers had much higher flexibility and torsion resisting capability.

The GO fibers exhibited a typical plastic deformation at room temperature, which was attributed to the possible stretching of the crumbled GO nanosheets, as well as the displacements of the GO nanosheets, as shown in Fig. 8.1d. The fibers possessed a Young's modulus of 5.4 GPa at small deformation in the elastic region and demonstrated fracture elongations of 6.8–10.1%, which were greater than those of filtrated GO papers (~0.4%) by more than one order of magnitude [18]. Also, the GO fibers showed a fracture strength of 102 MPa, which was within the range of filtrated GO papers, i.e., 70–130 MPa [4].

After the GO fibers were reduced through chemical reduction in 40% hydroiodic acid, the fiber shrunk in diameter, accompanied by the presence of a gray metallic luster. Meanwhile, the interlayer spacing was decreased from 8.9 Å ($2\theta = 9.86°$) to 3.7 Å ($2\theta = 24.25°$), according to XRD analysis results, with the latter to be close to the interlayer spacing of graphite (3.35 Å). The reduction led to an increase in both the Young's modulus (7.7 GPa) and fracture strength (140 MPa), while a fracture elongation of about 5.8% was also retained. The enhancement in mechanical strength was attributed to the stronger interactions between the graphene nanosheets, due to the much denser layer stacking. Similarly, crumbled graphene nanosheets were stretched when subject to tensile stress, which resulted in

the high fracture elongation of the graphene fiber, as shown in Fig. 8.1e. High flexibility of the graphene fibers was clearly shown in Fig. 8.1f–h.

This approach has also been applied to GO aerogel fibers, which had a "porous core–dense shell" structure, by combining spinning and ice-templating, from GO LCs [19]. Due to the interior uniform alignment of the GO nanosheets, the fibers possessed high tensile strength and high compression strength. The porous GO fibers could be reduced through chemical reduction and annealing process to obtain graphene fibers, without losing the porous structure, while gaining high electrical conductivity. This unique type of fibers had both high porosity and high mechanical strength and electrical conductivity, which could not be possible in most general materials.

Unique biomimetic composite fibers have been fabricated by using wet-spinning method combined with the liquid crystal self-templating (LCST) approach [20]. In the composite fibers, guest compounds, such as polymers and inorganic nanoparticles, could be homogeneously dispersed in the interchannels of LC GO nanosheets. The nacre-mimetic fibers exhibited a highly ordered hierarchical structure. The concurrent effect of ultrahigh aspect ratio, well-preserved alignment of the GO nanosheets, uniform single-molecule interlayer of polymers, and the presence of hydrogen bonding arrays ensured the formation of the macroscopic-assembled artificial nacre, with a high σ of 555 MPa and toughness of 18 MJ m^{-3}, which were 2–17 times higher than those of natural nacre (80–135 MPa and 0.1–1.8 MJ m^{-3}) [21, 22]. With an ultralow density of 1.0 g m^{-3}, the fibers possessed an optimal specific strength of as high as 652 N m g^{-1}, which was nearly two times that of most metals and alloys. The reduced composite fibers possessed a high electrical conductivity of 5261 S m^{-1}.

A one-step method is used to fabricate graphene fibers at large scale, through in situ reduction in basic coagulation baths [23]. Liquid crystallinity of the suspension was dependent on concentration and size of the GO nanosheets, which had a directional effect on processability of the LCs. Two types of fiber wet-spinning systems were employed to develop the graphene fibers. Spinability of the GO dispersions was evaluated by using the "petri dish method," in which the GO dispersion was injected at the flow rate of 5–10 ml h^{-1} into a rotating petri dish with coagulation bath that was rotated at 30–60 rpm. A custom-built wet-spinning apparatus was also used to study the continuous wet-spinning process. All the as-spun gel fibers were washed with 25 vol% ethanol–water and then air-dried at room temperature under tension, so as to obtain dried GO fibers. Two methods, i.e., (i) overnight annealing at 220 °C in vacuum and (ii) hydrazine vapor treatment at 80 °C for 3 h, were conducted to reduce the GO fibers to rGO fibers.

Figure 8.2a shows a POM image of the GO gel fibers, with birefringence being clearly observed, confirming the highly ordered GO domains that were retained during from the LC suspensions. It is well known that the formation of mono-domains of GO nanosheets requires a long timescale, if no external driving force is applied. One way to promote the alignment of LC GO is the application of external magnetic field. In this case, it took 5 h to form uniform LCs [23]. In contrast, macroscopic alignment during wet-spinning occurred almost immediately

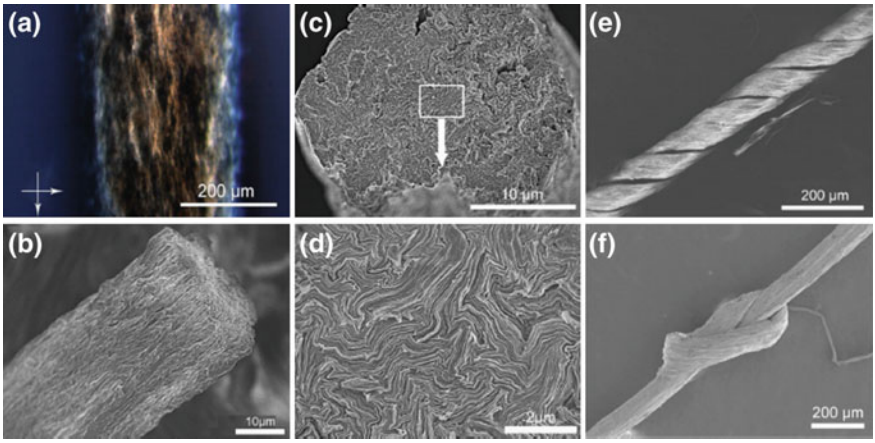

Fig. 8.2 **a** Polarized optical microscopy (POM) image of the as-spun GO gel fiber showing birefringence that confirmed the presence of ordered LC domains, with the *arrows* indicating the direction of polarizers. SEM images of as-spun GO fibers: **b** corrugated surface and **c** near-circular cross section. **d** Close view SEM image of cross section of the GO fiber shown in (**b**) revealing GO nanosheet planes that were oriented along the fiber axis. **e**, **f** SEM images of the crumpled and knotted rGO yarns (reduced by annealing) showing their high flexibility. Reproduced with permission from [23], Copyright © 2013, WILEY-VCH Verlag GmbH & Co. KGaA, Weinheim

(within several seconds), which was ascribed to the action of the shear stress generated through the spinneret, because of the 2D feature of the GO nanosheets. Microstructure analysis indicated that, in the dry fibers, the GO nanosheets were stacked in a layer-by-layer way, with only a slight degree of folding. Meanwhile, they were orientated in the direction of the fiber axis, as shown in Fig. 8.2b–d.

A similar wet-spinning assembly approach was reported to fabricate graphene fibers with GO solutions combined with chemical reduction [24]. GO fibers were developed by spinning GO dispersions in a coagulation bath of hexadecyltrimethyl ammonium bromide (CTAB) solution. This is the first report in which the assembly of GO nanosheets into macroscopic fibers was realized at low GO concentrations. The assembly mechanism of the GO fibers was clarified. The graphene fibers exhibited promising mechanical strength, high electrical conductivity, and high flexibility. Multifunctionality could be achieved through in situ or post-synthesis integration of various functional nanomaterials into the GO fibers.

In a separate study, graphene fibers were fabricated by using the wet-spinning and coagulation process, with focus on the understanding of the processing structure–property relationship [25]. Processing parameters include graphene dimension, spinning conditions, fiber density, and orientation in achieving optimum properties. It was found that both mechanical strength and electrical conductivity of the graphene fibers were closely related to the degree of orientation of graphene nanosheets in the fibers. The interaction between graphene nanosheets could be enhanced by using the solution of high GO concentration graphene nanosheets of

large size, which led to fibers with high electrical and mechanical properties. Also, mechanical properties of the fibers were more strongly influenced by the fiber packing density-related defects.

Because of the intrinsic alignment of the GO nanosheets along the long axis direction of the fibers, these wet-spun GO fibers generally have a low-tensile modulus. To address this problem, it is necessary to use large GO nanosheets as the building blocks to assemble fibers [26]. By doing this, modulus could be increased by one order of magnitude. For example, two types of GO nanosheets are used: (i) large flake GO (LFGO) nanosheets, with an average diameter of 22 μm; and (ii) small flake GO (SFGO) nanosheets, with an average diameter of 9 μm. Expectedly, the LFGO fibers demonstrated much higher mechanical performances than the SFGO fibers, in specific stress, specific modulus, and elongation by 178, 188, and 278%, respectively.

A coaxial two-capillary spinning strategy was developed to continuously to fabricate graphene-based hollow fibers (HFs) with well-controlled morphology [27]. Continuous GO-HFs and necklace-like HFs (nGO-HFs) could be spun out directly from concentrated GO suspensions. Graphene HFs (G-HFs) could be obtained through chemical reduction. The GO-HFs had a tensile strength of 140 MPa. They exhibited a typical elongation at break of about 2.8%, which was attributed to the possible displacement of the GO nanosheets within the walls. Furthermore, simultaneous functionalization of the GO-HFs could be achieved by introducing functional components directly into the core flow or mixing them with the initial GO suspension. By using thermal annealing, the GO-HFs could be converted to G-HFs, whereas their flexibility was not influenced while mechanical strength was improved.

A modified wet-spinning method was reported to produce graphene fibers by applying a shear stress [28]. The fibers fabricated in this way exhibited a macroscopic ribbon-like structure with high flexibility. Such ribbon-like graphene fibers could find a wide range of applications, such as elastic strain sensors, flexible counter electrodes for fiber solar cells, and fabric electrodes for supercapacitors. Figure 8.3a shows a schematic diagram of the spinning setup. The GO nanosheets with few layers were several micrometers in size. Aqueous GO suspension had a concentration of 6 mg ml^{-1}, which was injected by using a syringe pump into a chitosan solution placed on a stage that was rotated constantly at a speed of 10 rpm. The GO ribbons were collected by using a glass rod placed vertically in the chitosan solution.

During the spinning, the fluid flow direction was controlled to be perpendicular to the direction in which the GO suspension was injected (downward). Continuous ribbons were produced due to the presence of the shear stress. The ribbons exhibited a flat morphology, with a width-to-thickness ratio of up to 100, as shown in Fig. 8.3b. Photographs of the experimental setup, together with the glass rod, are shown in Fig. 8.3c–e. There were two reasons responsible for the formation of the ribbon structure, i.e., (i) electrostatic interaction between the GO nanosheets and chitosan in the coagulation bath, and (ii) the larger shear fluid velocity compared with the injection rate of the GO suspension. The width of the ribbons in the range

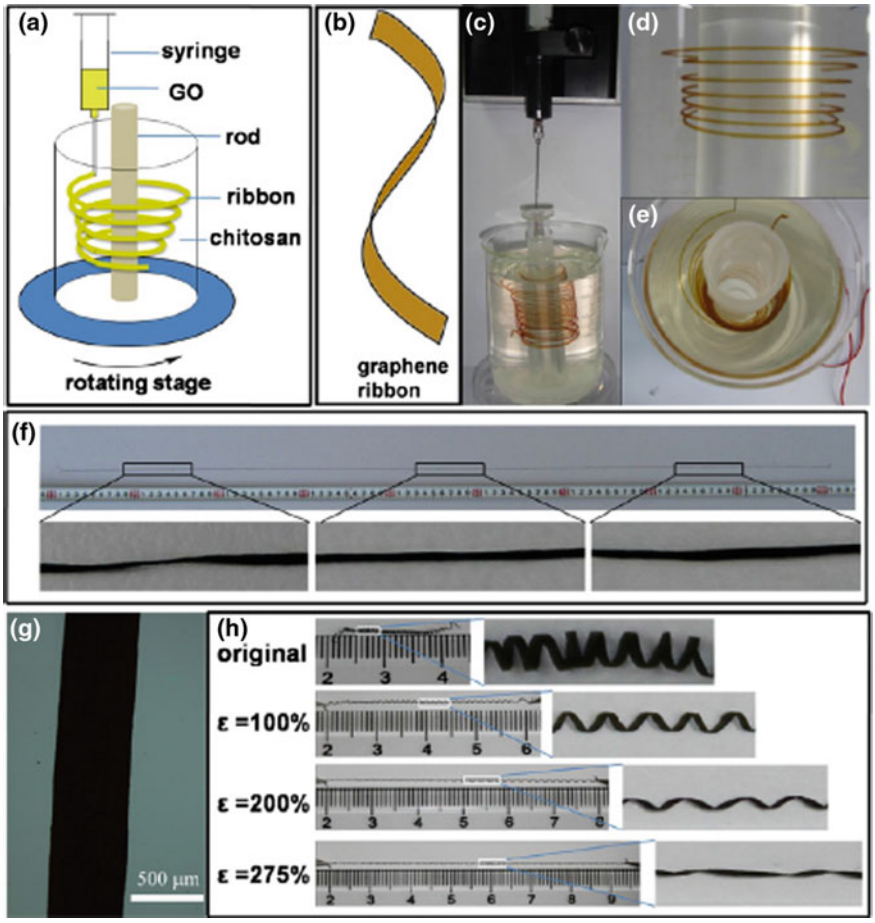

Fig. 8.3 Fabrication process and microstructures of the continuous graphene ribbons. **a** Schematic diagram of the wet-spinning setup. **b** Illustration of the flexible ribbon structure. **c** Photograph of the setup with a uniform GO ribbon spun in the chitosan solution. **d** Photograph of a single ribbon rotated around the collecting rod. **e** Top view of the setup. **f** Photograph of a 1-m-long and 300-μm-wide graphene ribbon after chemical reduction. **g** Optical image of a 500-μm-wide ribbon. **h** A ribbon made into spiral shape and then stretched to large strains. Reproduced with permission from [28], Copyright © 2013, American Chemical Society

of 200–500 μm was determined by the diameter of the tilted opening of a needle. Other factors included concentration of the GO suspension and chitosan, injection rate of the GO suspension and rotation speed of chitosan, which could be optimized to tailor morphology and property of the final ribbons.

Chemical reduction in hydroiodic acid was used to convert GO ribbons to rGO ribbon, accompanied by a color change from brown to black, as shown in Fig. 8.3f, g. The rGO ribbons possessed conductivities of 100–150 S cm^{-1}.

Figure 8.3h indicated that rGO ribbons showed very high flexibility. Wet ribbons could be wound onto a thin glass capillary to form a stable helical item after drying. When the spring-like structure was stretched, the twisted ribbon was not fractured and the shape could be recovered to a large extent.

Mechanical properties of the graphene ribbons had a close relation with orientation of the wrinkles. According to uniaxial tension testing results, oriented samples exhibited a relatively small failure strain of $\varepsilon < 4\%$, while those with random wrinkles demonstrated larger failure strain of $\varepsilon > 9\%$. In the oriented samples, the presence of tensile stress during the drying process triggered the alignment of the graphene nanosheets, thus leading to a denser stacking between the graphene layers and hence higher strengths (>100 MPa). In contrast, the highly wrinkled structure of the samples with random wrinkles possessed a lower strength due to larger intersheet distance, corresponding to a moderate tensile strain (up to about 14%) before fracture. It was also found that thickness of the ribbons was decreased with increasing fluid velocity, and the tensile strength of the graphene ribbons was increased with decreasing thickness over the range 7–1.5 μm. This was simply because thicker ribbons had more voids or defects.

8.2.2 Hydrothermal Approach

Hydrothermal treatment can facilitate spontaneous assembly and reduction in GO nanosheets, leading to graphene network via the strong interlayer π–π stacking between the graphene nanosheets [13]. A simple one-step dimensionally confined hydrothermal method was used to produce graphene fibers from aqueous GO suspensions [29]. A glass pipeline with an interdiameter of 0.4 mm was used as the reactor. GO suspension with a concentration of 8 mg ml^{-1} was injected into the glass pipeline, with the two ends being sealed, which was then treated at 230 °C for 2 h. Graphene fibers fit with the geometry of the pipeline were finally formed, with a diameter of 150 μm in wet state. The graphene fibers were collected from the pipeline by using N_2 flow and then air-dried. After drying, length of the fibers was not changed, while they were shrunk in diameter to $\sim$35 μm, due to the loss of water. The graphene fibers exhibited a very high flexibility, so that they could be woven into meshwork-like and cloth-like structures manually. The graphene fibers network could also be embedded into polydimethylsiloxane (PDMS) matrix by casting a mixed and degassed PDMS prepolymer on graphene fiber meshes, followed by thermal curing.

Figure 8.4a shows a graphene fiber with a length of 63 cm and a diameter of 33 μm. The process was very productive, where 1 ml GO suspension of 8 mg ml^{-1} yield graphene fiber of >6 m. Also, diameter and length of the fibers could be readily controlled either by using pipelines with different lengths and inner diameters or adopting GO suspensions with different concentrations. The large shrinkage

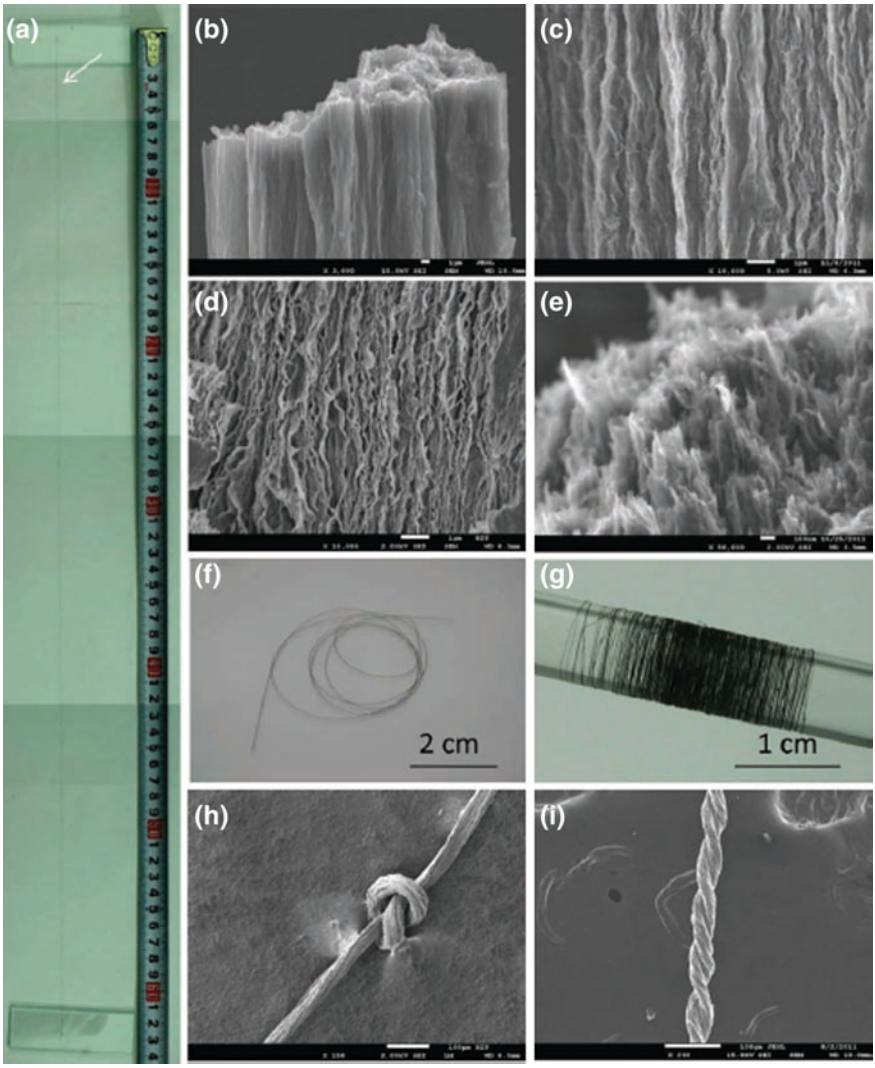

Fig. 8.4 Morphology and flexibility of the graphene fibers. **a** Photograph of a dry graphene fiber with a diameter of ~33 μm and a length of 63 cm. **b** SEM image of the broken part of a graphene fiber (scale bar = 1 μm). **c**, **d** Axial external surface and inner cross section SEM images of the graphene fiber, respectively (scale bars = 1 μm). **e** High-resolution SEM image of the broken section in (**b**) (scale bar = 100 nm). **f** Photograph of a wet graphene fiber coiled individually in water. **g** Photograph of dry graphene fibers coiled into bundle around a glass rod. **h**, **i** SEM images of the knotted and two-ply graphene fibers (scale bars = 100 μm). Reproduced with permission from [29], Copyright © 2012, WILEY-VCH Verlag GmbH & Co. KGaA, Weinheim

in diameter of the fibers during the drying process would produce surface tension forces that could promote spontaneous orientation of graphene nanosheets. The capillary force caused by the evaporation of water molecules led to a close packing of the porous graphene nanosheets. As a result, the fibers were densely packed and certainly aligned in the direction of axis, of the fibers, as shown in Fig. 8.4b–e. Figure 8.4e shows SEM image of a broken fiber, with the individual graphene nanosheets and their packing entanglement being clearly observed.

The dried graphene fibers had a Raman ratio of about 6:1, while the ratio of the wet fibers was close to 1:1, which further implied that the graphene nanosheets in the dried fibers were highly aligned parallel to the axis. Because no aggregation and preformed orientation were observed in initial GO suspensions before and after they were injected into the pipeline, the alignment of the graphene nanosheets in the direction of fiber axis was mainly ascribed to the effect of capillary-induced shear force and surface tension induced during dry process. The graphene fibers could be curved into coils and enlaced in bundles in wet and dry states, as shown in Fig. 8.4f, g. The fiber was not broken as the knot was tightened (Fig. 8.4h), while two-ply yarn could be made by twisting two fibers (Fig. 8.4i).

The hydrothermally as-derived graphene fibers possessed tensile strength of up to 180 MPa, which was increased to 420 MPa after they were thermally treated at 800 °C for 2 h in vacuum. Due to their relatively density of 0.23 g cm^{-3}, the fibers reached a density-normalized failure stress of 782 MPa (g $cm^{-3})^{-1}$. Typical elongations at the beak of the graphene fibers were in the range 3–6%. The graphene fibers exhibited an electrical conductivity of $\sim$10 S cm^{-1}. The electrical conductivity was nearly not affected when the fibers were bent over 1000 cycles. Due to their high flexibility and mechanical strength, the graphene fibers could be shaped to various geometries. In addition, functional components could be incorporated into the graphene fibers to further amplify their functionality. Because the as-obtained wet graphene fibers were highly porous, they can be used as host to incorporate other components during the drying process.

Another hydrothermal method led to a dually geometric confinement approach, which enabled meter-long hollow GFs (hGFs) with tunable diameters [30]. The hGFs were microtubings (μGTs), which could find potential applications for fluidics, catalysis, purification, separation, sensing, and environmental protection. The meter-long μGTs had diameters tunable in the range 40–150 μm. The μGTs could be shaped to have hierarchical multichannels. In addition, selectively site-specific functionalization could be realized on outer wall, inner wall, outer/inner wall, and within wall, in a well-controlled way, which made it possible to create μGTs with desired properties for targeted applications, such as stimulus-responsive devices and self-powered micromotors. The μGTs had stable flexibility and strong mechanical strength. The wet μGTs could have various predesigned configurations realized through the Cu wires. The predesigned structures were well retained after drying.

8.2.3 *Chemical Vapor Deposition (CVD)*

Chemical vapor deposition (CVD) graphene films have been used to fabricate graphene fivers through self-assembly [31]. The graphene fibers were porous and continuous with tunable diameter and pore distribution. They were also mechanically flexible with high electrical conductivity. Graphene films were grown on Cu foils by a CVD method, with methane as the precursor. Four steps were involved in the 2D film to 1D fiber transformation process, as shown in Fig. 8.5a–d. Firstly, free-standing CVD graphene films were made to float in water after the substrates

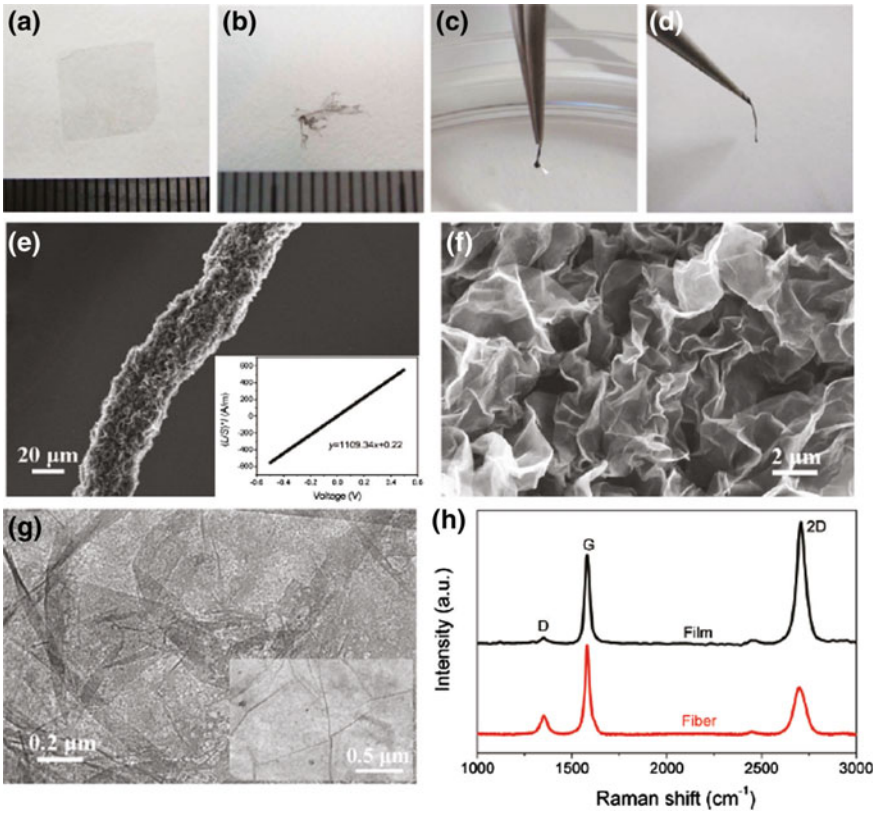

Fig. 8.5 Graphene fibers through the film to fiber self-assembly. **a** Free-standing graphene film on deionized water surface. **b** Scrolled and wrapped graphene film when transferred onto ethanol. **c** Graphene fiber drawn out of ethanol. **d** Porous and wrinkled structure of the dried fibers. **e** Low-magnification SEM image of a graphene fiber, with the inset showing the current density–voltage curve, yielding a conductivity of 1000 S m^{-1}. **f** SEM and **g** TEM images of the graphene fiber, showing wrinkled and porous structure, with the *inset* showing TEM image of pristine graphene film. **h** Raman spectra of the graphene film and the fiber. Reproduced with permission from [31], Copyright © 2011, American Chemical Society

were etched (Fig. 8.5a). Secondly, the graphene films were collected and transferred onto the surface of ethanol. Once the graphene films were put on ethanol, their edges immediately scrolled up, thus leading to agglomerates, which sank into the liquid (Fig. 8.5b). Thirdly, the graphene films were picked out (Fig. 8.5c), which shrank into fibers after the evaporation of ethanol (Fig. 8.5d). Eventually, graphene fibers were obtained after drying.

Figure 8.5e indicated that the fibers obtained from 1 cm^2 films had a diameter of 20–50 μm. Geometric size of the fibers was mainly determined by the size of the original graphene films and could be controlled to change other parameters, e.g., the drawing rate. The graphene fibers were mechanically flexible, so that they could be conveniently manipulated. They exhibited an electrical conductivity of 1000 S m^{-1}, as shown in the inset of Fig. 8.5e, due to the high quality of the CVD-derived graphene nanosheets. Figure 8.5f shows SEM image of the fibers, which were wrinkled and highly porous. The porous structure forms upon ethanol evaporation during the drying process. The pores were formed by the scrolled graphene nanosheets, as shown in Fig. 8.5g. Figure 8.5h shows typical Raman spectra of the graphene film and the fiber.

The self-assembly process experienced two stages, i.e., (i) scrolling of the film to form the fiber and (ii) shrinking of the fiber. The scrolling process was facilitated by the surface tension. Generally, because graphene films are relatively hydrophobic, they can be wetted by most organic solvents. Once being contacted with ethanol, the graphene film became very flexible. At the same time, solvent evaporation played an important role in the formation of graphene porous structure. After the fiber was formed, its surface was still covered by a liquid layer of ethanol. Pore size of the porous graphene fibers could be controlled by controlling the rate of solvent evaporation. Due to their porous structure, the graphene fibers could be used as electrodes of electrochemical devices. They could also be further functionalized by incorporating other components.

A similar CVD method has been employed to directly grow graphene layers on Cu meshes [32]. After deposition, the Cu wires were etched out with $FeCl_3$/HCl aqueous solution, so that hGFs with a network configuration were developed, which was named as graphene-based woven fabrics (GWFs). The GWFs could be transferred onto polydimethylsiloxane (PDMS) substrates, thus forming graphene-based woven fabric/PDMS hybrid films, which could find various applications. The GWFs possessed various special structural and characteristic features. Firstly, they exhibited high structural integrity, with much higher mechanical strength than polycrystalline graphene films. Secondly, there were micron-sized holes present in the GWFs, so that they were highly permeable, as compared with graphene monolayers. Also, they had unique exponential resistive response to external loadings, which could be used to develop strain sensors. Two applications have been demonstrated by using the GWFs, i.e., (i) GWFs/polymer composites and (ii) GWFs/semiconductor solar cells.

3D graphene networks have been obtained through substrate-assisted reduction and assembly of GO (SARA-GO) [33]. GO nanosheets were reduced and assembled into 3D networks on various substrates, including active metals of Zn, Fe, and

Cu, inert metals of Ag, Pt, and Au, semiconducting Si wafer, nonmetallic carbon-based films and even indium-tin oxide (ITO)-coated glass. Various graphene assemblies have been developed, including microtubes, four-way pipes, spiral tubes, multichannel networks, and micropatterns, which could be used to fabricate binder-free rechargeable lithium-ion batteries (LiBs).

8.2.4 Graphene Ribbon Fibers from Unzipped CNTs

Graphene nanoribbons with high aspect ratios can be obtained by unzipping CNTs [34–37]. These graphene ribbons have been used to prepare graphene fibers. A scalable method has been developed to fabricate long and narrow graphene nanoribbons, with which large graphene nanoribbon sheets were assembled and aligned first, while macroscopic neat graphene nanoribbon fibers were then obtained by twisting the sheets [38]. The graphene ribbon fibers showed high conductivity and good mechanical performance. The graphene ribbons were prepared by unzipping aligned nanotubes through oxidation, which were then reduced through thermal reduction. The graphene nanoribbons were highly aligned before and after the reduction process, which was confirmed by polarized infrared spectra. The graphene nanoribbon yarns exhibited a much higher electrochemical performance than the conventional twist-spun MWCNT yarns, which was attributed to incomplete reduction in the graphene nanoribbons. Most importantly, the conversion process could be scaled up for industrial production for applications as woven electrodes of fuel cells, supercapacitors and batteries.

Similarly, GONRs and chemically reduced graphene nanoribbons can also be dispersed with high concentrations in chlorosulfonic acid to form anisotropic LC phases for wet spinning of GFs [39]. The graphene oxide nanoribbons (GONRs) were prepared by unzipping MWCNTs through oxidation. The GONRs fibers could be thermally reduced (tr) into trGNR fibers. Alternatively, GONRs could be chemically reduced (cr) with hydrazine to crGNRs, with which were crGNR fibers were fabricated through spinning. As the crGNR fibers were further annealed (a), a-crGNR fibers were obtained.

Both the crGNRs and GONRs could be dispersed in chlorosulfonic acid to form anisotropic liquid crystal phases at room temperature. Diethyl ether (boiling point b_p = 35 °C, viscosity = 0.224 cP at 25 °C) was used as the coagulation bath solvent. The spinning apparatus included a spinning chamber with a piston. The piston was connected to a pressure controller at one end of the chamber, while a spinneret (capillary tube) was affixed to the other end of the chamber. The lyotropic materials were extruded, through the small spinneret, into the coagulation bath with an air gap to produce aligned ribbons within the as-spun fibers. The ribbons had an average length of 4 μm and widths of >100 nm. AFM analysis indicated that the height of the ribbon was about 1.2 nm, implying that the ribbons were single-layer graphene. 2 wt% GONRs and crGNRs were studied by using polarized optical microscope (POM).

It has been demonstrated that cross-sectional shape of wet-spun fibers is closely related to the coagulation conditions. A coagulation bath should meet certain requirements. For example, the GONRs should not be soluble in the coagulation bath. The cross-sectional shape of the wet-spun fibers is determined by the deformability of the coagulated layers and the mass transfer rate difference. It means that the coagulation rate should be sufficiently high, so that the coagulated layers will have low gradient at the interface near the surface layer. In this case, the coagulated outer layers will not collapse toward the core, thus leading to fibers with a circular shape. The mass transfer rate difference should be sufficiently low, in order to maintain a state where the solvent diffusion rate out of the fiber should be similar to the absorption rate of the nonsolvent. If the two rates are largely different, an irregular cross-sectional shape will likely be produced. Also, the viscosity of the bath should be as sufficiently low, to avoid surface etching of the fibers when going through the bath, thus leading to desirable surface morphology.

Water was first tested to prepare GONR solutions, due to the fact that it is easier to handle as compared to chlorosulfonic acid. Liquid crystal phase was observed in 5 wt% GONR aqueous solution. Ethyl acetate, methyl acetate, and diethyl ether were used as the coagulation bath, which all could not result in fibers with promising morphologies. Therefore, water was not suitable to develop GONR fibers. Instead, chlorosulfonic acid had to be employed as the solvent.

Figure 8.6 shows SEM images of the GONR fibers spun from 8 wt% chlorosulfonic acid solution, with diethyl ether solvent as the coagulant bath, clearly indicating that the fiber possessed a nearly perfect circular cross-sectional shape. The GONR fibers spun with different air gaps had an average diameter of 54 μm, tensile strength of 33.2 MPa, modulus of 3.2 GPa, and elongation of 1.64%. They were highly flexible. As shown in Fig. 8.2c, the fiber could be easily knotted into a loop with a minimum diameter of about 1 mm. The as-spun GONR fiber had porosity, measured by using the BET method, corresponding to a surface area of 58 $m^2\ g^{-1}$.

Surface morphologies of the 1050 °C trGNR with 1.3 g force (gf) pretension are shown in Fig. 8.7a, b. The diameter of the fiber was decreased because the oxygen

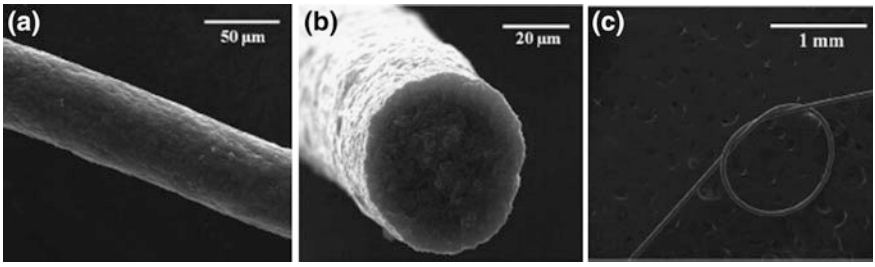

Fig. 8.6 Morphologies of the GONR fibers spun from the 8 wt% suspension. **a** Surface morphology of the as-spun fiber. **b** Transverse cross-sectional morphology. **c** Fiber knotted into a loop. Reproduced with permission from [39], Copyright © 2013, American Chemical Society

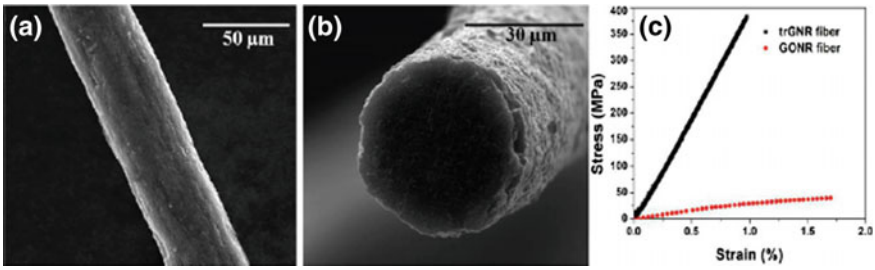

Fig. 8.7 **a** Surface morphology of the 1050 °C annealed trGNR fiber. **b** Cross-sectional morphology of the 1050 °C annealed trGNR fiber. **c** Typical stress–strain curve of the as-spun GONR fiber (12-cm air gap) and 1050 °C annealed trGNR fiber (12-cm air gap) with 1.3-gf pretension. Reproduced with permission from [39], Copyright © 2013, American Chemical Society

functional groups and some voids were removed due to the thermal reduction. Optimized mechanical performances of the fiber included a tensile strength of 383 MPa, a modulus of 39.9 GPa and an elongation to break of 0.97%. A representative stress–strain curve is shown in Fig. 8.7c. The tensile strength and modulus were increased by nearly one order of magnitude, when compared with the as-spun GONR fibers. Higher molecular alignment leads to higher tensile modulus. The trGNR fibers showed higher tensile modulus than the graphene fibers fabricated by using other methods ($\sim$10 GPa), as discussed before [14, 24, 29]. Due to the presence of residual microvoids, density of annealed trGNR fiber was 0.88 g cm^{-3}, which was less than half of that of conventional carbon fibers of 1.75–2.2 g cm^{-3} [40]. As a result, specific strength of the trGNR fiber was 430 kN * m kg^{-1}. Microstructure of the fibers could be improved by using high-temperature thermal annealing. Electrical conductivity of the fibers could be significantly increased by removing the oxygen groups and aligning graphene ribbons.

8.2.5 Other Methods

An electrophoretic self-assembly method was used to fabricate polymer-free and surfactant-free fibers from rGO nanoribbons [41]. Because no additive was contained in the fibers, it was possible to monitor the state of oxidation as the graphene oxide nanoribbons (GONRs) were reduced. This state could be correlated to the property of the fibers for different applications. Electrical and field emission properties of the fibers as a function of oxidation state of the GO nanosheets were evaluated. Especially for field emission, the rGONR fibers exhibited a low threshold electric field of 0.7 V μm^{-1} and a giant current density of 400 A cm^{-2}. Additionally, the fibers were stable at a high current density of 300 A cm^{-2}.

The GONRs were prepared by unzipping CVD-produced carbon MWCNTs with solution of $KMnO_4$ in sulfuric acid. The optimal concentration of $KMnO_4$, in order

to unzip the MWCNTs with a diameter of about 10 nm in the axis direction, was in the range 800–900 wt%, with respect to the amount of the MWCNTs. For example, 30 mg of MWCNTs powder was dispersed in 30 ml H_2SO_4, in which 250 mg $KMnO_4$ was added. The mixture was then heated at 55 °C for 30 min first. After that, the temperature was increased to 65 °C so that oxidation reaction was completed, which was then increased to 70 °C, followed by cooling to room temperature. The GONRs were collected after thorough washing and drying. The dried GONRs were dispersed in a mixture solvent of DMF/H_2O with a volumetric ratio of 9:1. Chemical reduction in GONRs was achieved with hydrazine monohydrate (1 μl for 3 mg GO) at 80 °C for 12 h. Well-dispersed colloidal solutions were obtained after ultrasonication for 10 min.

A graphitic tip was used as a positive electrode which was immersed into the chemically reduced GONR colloidal suspension in a Teflon vessel in which a counter electrode was embedded. The immersed tip was separated by about 5 mm away from the counter electrode. A constant voltage in the range 1–2 V was applied between the electrodes during the withdrawal process of the graphitic tip, which was at 0.1 mm min^{-1}, at 20–25 °C and 18–23% relative humidity. For thermal reduction, the chemically reduced GONR fibers treated in Ar at atmospheric pressure, at temperatures of 200, 500, and 800 °C for 1 h. The rGONRs had widths of 15–35 nm and thicknesses of 2.5–6.0 nm, corresponding to few-layer stacks. Also, rGONR fibers could be derived directly from reduced GONR solution.

A scalable self-assembly method at the liquid/air interface was reported to prepare GO fibers from aqueous GO suspensions, without using any polymer or surfactant [42]. The GO fibers were mechanically flexible, while their electrical conductivity could be significantly increased by using a low-temperature hydrothermal treatment at 180 °C for 5 h. When stable GO suspensions were kept a beaker of 2000 ml at room temperature, GO fibers were assembled and grew at the liquid/air interface in two-week time. The GO fibers were stable, free-standing, and floating on surface of the GO solution, which could be transferred onto arbitrary substrates. After washing and drying, dried GO fibers were obtained, which were intertwined into GO fiber films before they were transferred onto SiO_2/Si substrates. The GO fiber films were hydrothermally treated together with the SiO_2/Si substrates. Diameter and length of the fibers were controlled by either changing the size of the containers or controlling the times of ultrasonic treatment and self-assembly process.

8.3 Graphene-Based Free-Standing Papers (2D)

Free-standing papers or membranes based on graphene nanosheets have attracted much attention, due to their potential applications, especially in flexible electronic and energy storage devices [18, 43, 44]. Among various methods, vacuum filtration of G/GO suspensions through a porous membrane filter has been the most widely used technique to fabricate G/GO papers [45–95]. Other methods included solution

casting [96–102], tape casting [103], electrospray deposition (ESD) [104], electrophoretic deposition (EPD) [105], interface self-assembly [106, 107], cryogel [108], pyrolyzed asphalt [109], hydrothermal synthesis [70], and chemical vapor deposition (CVD) [110, 111],

8.3.1 Membrane Vacuum Filtration

Membrane vacuum filtration is the simplest and most straightforward method to prepare G/GO papers. Solvents are passed through the porous membranes, while G/GO nanosheets are blocked by the membranes as films. The films are then peeled off as free-standing papers after a certain degree of drying. For instance, GO papers with thicknesses in the range 1–30 μm have been fabricated by using this technique [18]. Structural characterization of GO paper indicated that the compliant GO nanosheets were interlocked/tiled together parallel in the horizontal direction, i.e., the formation of the ordered structures was attributed to the flow-directed assembly process. The GO paper exhibited high flexibility and strong mechanical properties. Compared with the conventional carbon- and clay-based papers, the extraordinary mechanical properties of the GO paper were originated from the strong van der Waals interactions and hydrogen bonding within GO nanosheets.

GO nanosheets were dispersed in water to form GO suspension at a concentration of 3 mg ml^{-1}. Thickness of the GO papers was controlled by adjusting the volume of the colloidal suspension. The GO paper prepared in this way could be cut by using a razor blade. The papers were uniform, while they were dark brown under transmitted white light and almost black in reflection as the thickness was > 5 μm, as shown in Fig. 8.8a–c. SEM images revealed that the highly oriented nanolayers were closely packed through almost the entire cross section of the papers, with less densely packed "wavy" skin layers with thicknesses in the range 100–200 nm, as shown in Fig. 8.8e–g. The layered structure was also confirmed by XRD patterns. Layer-to-layer distance or *d*-spacing of the GO papers was about 0.83 nm, corresponding to the presence of one-molecule-thick layer of water interacting with the GO nanosheets through hydrogen bonding [112]. Average dimension of the ordered stack of GO nanosheets in the papers oriented perpendicularly to the diffracting plane was about 5.2 ± 0.2 nm, corresponding to 6–7 stacked GO nanosheets.

With three regimes of deformation in the stress–strain curves, i.e., straightening, almost linear (or "elastic"), and plastic, mechanical behavior of the GO papers was similar to that of most paper-like or foil-like materials, but had very high stiffness. Despite the presence of different levels of wrinkling and "waviness" in the GO papers at different length scales, the initial straightening during the tensile loading was not very pronounced. During the rupture of the GO papers that were loaded beyond the "elastic" regime, no pull-out of their lamellae was observed. Instead, nearly straight and flat fracture surfaces were formed, as shown in Fig. 8.8e–g. This was attributed to

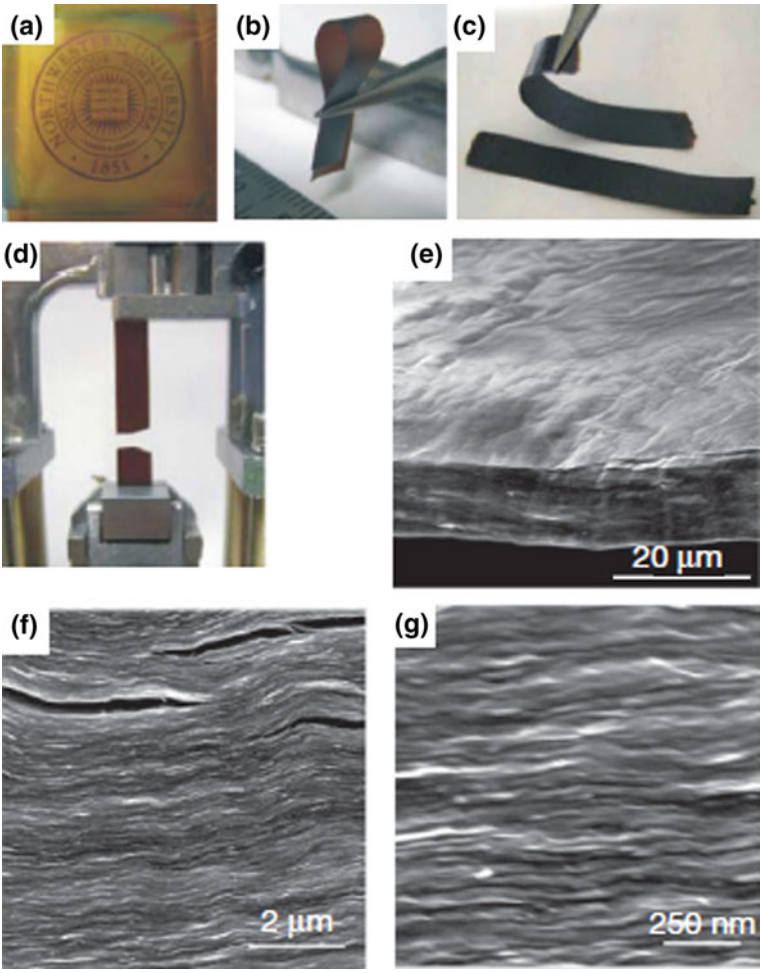

Fig. 8.8 Morphology and structure of the GO papers. **a**–**d** Photographs of the GO papers: **a** about 1-μm-thick film, **b** folded about 5-μm-thick semi-transparent film, **c** folded about 25-μm-thick strip and **d** strip after fracture after tensile loading. **e**–**g** Low-, middle-, and high-resolution SEM side-view images of the ~10-μm-thick papers. Reproduced with permission from [18], Copyright © 2007, Macmillan Publishers Limited

their high homogeneity and strong interlayer interaction. The GO papers exhibited an average modulus of 32 GPa, with the highest value to 42 ± 2 GPa.

Because GO papers are nonconductive, which cannot be directly used for some applications, e.g., electrodes of LiBs and supercapacitors, where high electrical conductivity is critical to maintain a high performance. As a result, it is desired to reduce GO papers into rGO papers. Various reduction methods have been employed to reduce GO papers, including hydrazine hydrate reduction [83],

photothermal reduction [113], supercritical ethanol reduction [106], and thermal reduction [114, 115].

Due to the highly conjugated structure, graphene and graphene-based materials have extraordinary electrical properties, which thus could be controlled by manipulating the degree of the in-sheet conjugation. This approach has been applied to graphene papers, whose conductivities could vary over a wide range of 0.001–100 S cm^{-1} [84]. The objective was achieved at the molecular level, through either covalent bonding or π–π stacking interactions by using either monofunctional or bifunctional molecules. Functional molecules, including monoaryl diazonium salts (MDS), bifunctional aryl diazonium salts (BDS), and bipyrene terminal molecular wire (BPMW), have been used for such a purpose. It was found that both MDS ad BDS led to a decrease in conductivity of the graphene papers, with BDS having a finer modification effect. In contrast, the graphene papers modified with BPMW had higher electrical conductivity that of the other two groups of samples.

Graphene papers consist of tightly stacked graphene nanosheets, thus leading to poor permeability, which could limit their applications where high permeability and tunable layer spacing are required. A simple method was developed to modulate the layer spacing of GO papers, by using the temperature-dependent decomposition reaction of ammonium nitrate (AN, NH_4NO_3) [85]. Different form the commonly used intercalation method, this approach could tailor the layer spacing of GO papers over a very large range of 123–20,000%, but without the presence of any guest molecules. With such a wide range of expansion amplitude, the GO papers could find various applications, such as highly efficient exclusion of small organic molecules, separation of ultrathin nanoparticles, and loading of polar and nonpolar guest molecules. Moreover, once the GO papers were reduced to rGO papers, with high electrical conductivity, the papers could be used for flexible paper-based electrochemical devices.

Besides wet-chemical exfoliated GO and graphene nanosheets, chemical vapor deposition (CVD)-derived graphenes have also been used to fabricate graphene papers by using vacuum membrane filtration [74]. The graphene papers from the CVD-derived graphene exhibited superior electrochemical performances, with a capacity of 1200 mAh g^{-1} at 50 mA g^{-1} as electrodes of supercapacitors and excellent cycling characteristics as anodes of lithium-ion rechargeable batteries. The CVD graphene nanosheets had a lateral size at the order of hundreds of micrometers, with a production at gram scale, by using a layered Fe containing natural mineral, expanded vermiculite, as template. Due to the large sheet size of the CVD graphene nanosheets, the obtained graphene papers were highly flexible with a loose stacking state. Moreover, graphene-carbon nanotube (G-CNT) hybrids could also be synthesized in just one step.

Graphene quantum dots (GQDs) have been proposed to be a stabilizer to achieve aqueous dispersions of graphene nanosheets [70]. GQDs have both special atomic structure and surface chemistry, with one- to few-layered graphene nanosheets that have a lateral dimension smaller than 100 nm [116–118]. Due to the 2D sp^2 carbon structure, GQDs are expected to be able to strongly attach to the basal plane of graphene nanosheets through van der Waals attractions, i.e., π–π stacking. Also,

GQDs contain same hydrophilic surface groups, such as carboxyl, hydroxyl, and epoxy groups, as GO, due to the similarity in their synthetic processing [119, 120]. Owing to the presence of these hydrophilic groups, GQDs have high solubility in water, so that they could promote the dispersion of the intrinsically hydrophobic graphene nanosheets. With the incorporation of GQDs, commercially available graphene powder could be well dispersed in water, which led to highly flexible and highly conductive graphene papers by using the vacuum filtration technique.

The graphene dispersions were prepared involving three steps: (i) dispersing graphene powder in GQDs solution, (ii) removing excess GQDs, and (iii) re-dispersing the graphene slurry. In this case, the presence of the GQDs played was a crucial requirement to stabilize the graphene nanosheets in water. There could be two mechanisms governing the enhanced dispersion of graphene. Firstly, the surface of the graphene was modified due to the absorption of the GQDs, so that the graphene nanosheets became to be negatively charged and thus electrostatically stabilized in water. Secondly, the GQDs were uniformly distributed to surround the graphene nanosheets, so that they were blocked from one another. As a consequence, agglomeration of the graphene nanosheets was effectively prevented.

Figure 8.9a shows a photograph of the free-standing graphene papers with a diameter of about 3.8 cm, which were highly flexible and bendable. A free-standing and bendable paper with a diameter of about 3.8 cm (Fig. 8.9a) was obtained after peeling off the membrane. Cross-sectional SEM images of the graphene papers are shown in Fig. 8.9b, c, at low- and high-magnifications. The graphene nanosheets were highly oriented in the plane of the papers, which suggested that the graphene nanosheets were deposited on the filter membrane in parallel direction. The completely dried graphene papers had apparent densities in the range 1.22–1.51 g cm^{-3}.

The presence of partially π–π stacking between the adjacent graphene nanosheets is confirmed by the XRD results, as shown in Fig. 8.9d. The graphene papers had a relatively strong peak at 23.7°, corresponding to plane spacing of d_{002} = 0.37 nm. Electric conductivity of the graphene paper was up to 7240 S m^{-1} at room temperature. It was found that the average conductivity was decreased from 7240 to 2506 S m^{-1}, as the content of the GQDs was increased from 7.0 to 28.8%. Therefore, the content of the GQDs in the graphene papers should be controlled at a sufficiently low level. For a graphene paper with a thickness of 18.0 μm, tensile strength, ultimate tensile strain, and Young's modulus were 91.2 MPa, 1.7% and 5.3 GPa, respectively. Therefore, this approach could be a new route to develop flexible graphene papers with controllable properties.

Graphene or GO papers have a nanoscale "brick-and-mortar" structure, in which the interaction between adjacent nanosheets could be mediated by intercalated solvents [121–123]. There have been reports on mechanical properties of the papers, together with strategies to improve their mechanical strength [121, 124]. However, in order to realize "materials design" for such special paper materials, it is necessary to clearly understand the formation mechanisms. As seen in the above discussion, vacuum membrane filtration has been the major technique to develop various G/GO papers, which involves the flow-directed assembly of graphene or GO nanosheets, as their suspensions are filtered over a supporting membrane.

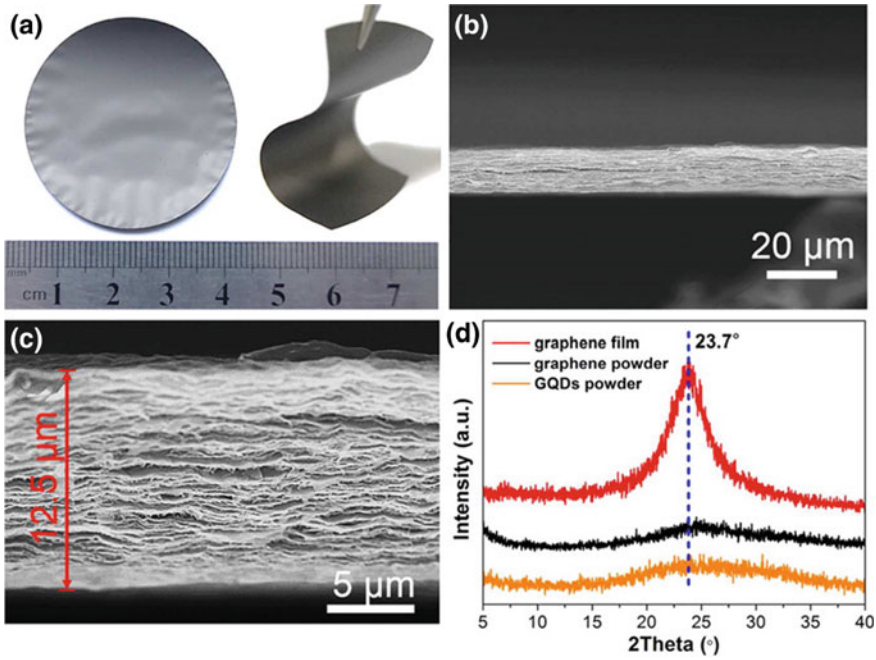

Fig. 8.9 **a** Photographs of the flexible graphene papers with metallic luster. **b**, **c** Low- and high-magnification cross-sectional SEM images of the graphene papers, illustrating the uniform thickness (12.5 μm) and layered structure. **d** XRD patterns of the graphene paper, graphene powder, and GQDs, with a peak observed for the graphene paper confirming the π–π stacking of the graphene nanosheets formed during the paper filtration process. Reproduced with permission from [74], Copyright © 2015, American Chemical Society

Obviously, the papers with well-aligned G/GO nanosheets are derived from suspensions in which all the nanosheets are entirely randomly distributed. Also, it has been observed that the layered structures could be swelled by several solvent molecules without destroying the layered structures [112, 125], while the swelling is reversible, i.e., after drying in air the original structures are completely recovered [69, 94].

It has been suggested that a gelation process of the graphene nanosheets took place at the solution–filter membrane interface during filtration, which was related to the formation of mechanically strong, highly conductive, and anisotropic graphene papers [50]. More importantly, various organic or inorganic components could be incorporated into the graphene papers to form composites or hybrids [126, 127].

In a separate study, three formation mechanisms have been considered to explain the wide range of possible ordering sequences during the fabrication of GO papers through vacuum membrane filtration [53]. In brief, they were two extreme cases, i.e., highly ordered layering and complete disordering, together with the cases in

between the two extreme two. At the highly ordered layering end, order structure was developed as the nanosheets were deposited. At the other end, the GO nanosheets were randomly distributed during the filtration process, until they were aligned due to the geometric confinement caused by the removal of the solvents. The third mechanism was known as semi-ordered accumulation, which resulted in the formation of loosely stacked nanosheets at surface of the filter membranes. During the removal of the solvents, the semi-ordered layers were transferred to layered structures, owing to the filtration-induced compression. Experimental results suggested that the semi-ordered accumulation mechanism has governed the formation of GO papers through vacuum membrane filtration.

8.3.2 Other Methods

8.3.2.1 Solvent Direct Evaporation

A direct solvent evaporation method was used to fabricate GO papers from GO suspension with mild heating [100]. The GO thin papers had an average thickness of about 8.4 μm, which exhibited excellent EMI shielding effectiveness of 20 dB and high in-plane thermal conductivity of 1100 W m^{-1} K^{-1}, as well as high mechanical flexibility and structure integrity withstanding repeated bending. Figure 8.10a shows a schematic diagram describing fabrication process of the GO thin papers through direct evaporation. GO suspensions were poured into Teflon dishes, which were heated gently at 50–60 °C to evaporate the water, so that flexible dark brown GO papers were formed. Obviously, thickness of the papers could be well controlled from microns to ten microns by controlling the volume and concentration of the GO suspensions. Also, this method has no limit in size of the GO papers. In this respect, it was advantageous over the vacuum membrane filtration method discussed above.

Figure 8.10b shows photograph of the GO paper with a dimension of about 400 cm^2 made simply by using a mold of that size. The GO papers were sufficiently flexible, so that they could be rolled and folded, as shown in Fig. 8.10c. SEM observations indicated that the GO papers had smooth with a few thin ripples, as shown in Fig. 8.10d. The multilayered structure was maintained through almost the entire cross sections, as shown in Fig. 8.10e, f, without difference from that of their vacuum filtration counterparts. During the evaporation of water, concentration of the GO suspensions was gradually increased, so that the sheet-to-sheet interactions were facilitated, thus leading to self-alignment of the GO nanosheets due to their relatively large lateral dimension.

The GO papers were thermally annealed at 2000 °C for further reduction and graphitization, which resulted in graphene papers (denoted as GF-2000) [128, 129]. The GF-2000 sample exhibited almost no variation in physical dimension as compared the as-obtained GO papers, whereas it became darker and black with a shiny metallic luster, as observed in Fig. 8.10c. Figure 8.10d shows SEM image of

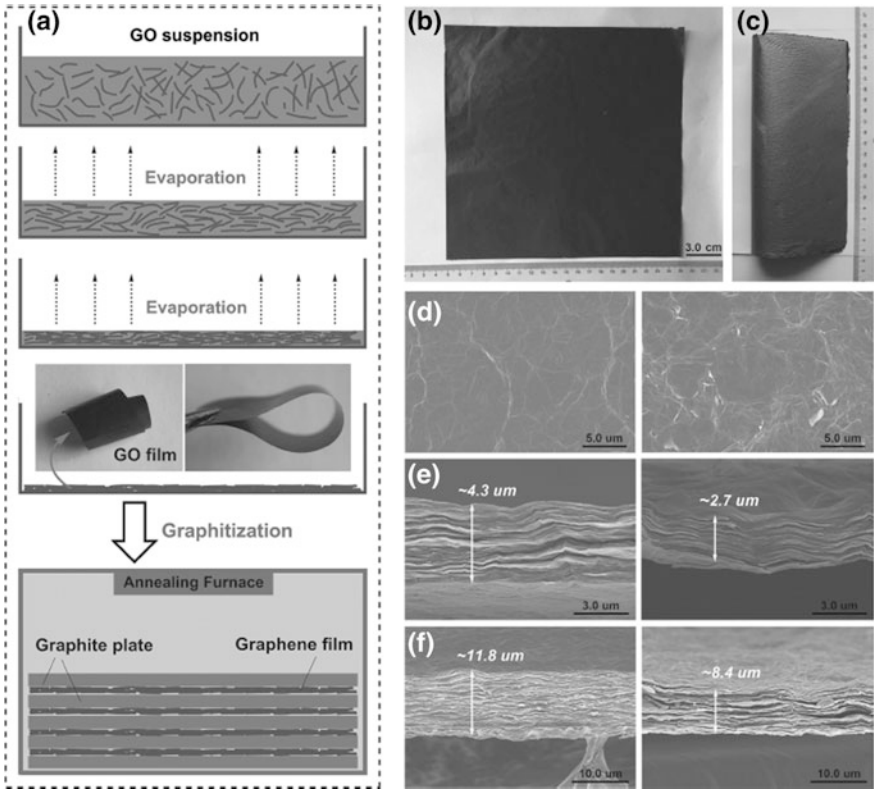

Fig. 8.10 **a** Schematic diagram of the self-assembly process to obtain the GO papers through evaporation and thermal graphitization treatment. The *inset* shows photographs of the flexible GO papers. **b** Photograph of the free-standing and dark brown GO paper with a dimension of 20 cm × 20 cm. **c** Photograph of the free-standing and shiny metallic GF-2000 (20 cm × 20 cm) folded on a paper. **d** Surface SEM images of the GO paper (*left*) and GF-2000 sample (*right*). **e**, **f** Cross-sectional SEM images of the GO paper and GF-2000 sample (with different thicknesses). Reproduced with permission from [100], Copyright © 2014, WILEY-VCH Verlag GmbH & Co. KGaA, Weinheim

the GF-2000 sample, indicating its smooth surface and the presence of ripples. Cross-sectional SEM images of the GF-2000 sample are shown in Fig. 8.10e, f, illustrating the highly oriented multilayer stacking of the graphene nanosheets. The thicknesses were decreased from 4.3 and 11.8 μm to 2.7 and 8.4 μm, respectively, due to the removal of the oxygen groups and water molecules.

8.3.2.2 Tape Casting

Most of the methods that have been available in the open literature to fabricate G/GO papers are limited only at the laboratory scale. Tape casting is a promising

candidate that can be used to address this problem, as demonstrated in a recent study [103]. Polymer graphene composite tapes were prepared first, while the polymer was subsequently removed through thermolysis, which led to large-scale graphene papers with a network structure. The graphene tapes exhibited high surface area, excellent electrical conductivity, and promising mechanical strength.

Figure 8.11 shows the process of tape casting, in which the colloidal suspension was cast through a slit by moving the substrate relative to a doctor blade. The graphene used in the tape casting should have sufficiently large quantities, which was produced through the simultaneous thermal exfoliation and reduction in GO powder. Besides the oxygen-containing functionalities as stated earlier, the graphene network contained lattice defects and vacancies, as shown in the inset of Fig. 8.11. The functionalized graphene nanosheets (FGSs) could be distinguished according to their oxygen contents, which was expressed as carbon-to-oxygen ratio (C/O in mol/mol). Wrinkles were formed on the graphene nanosheets, due to the presence of the defects and oxygen-containing groups, which decreased the contact area in between the adjacent graphene nanosheets and also prevented the re-stacking. This happening could be an advantage for applications that require high surface area. Moreover, chemical activity of the FGSs was increased because of the defect sites and the functional groups, which could find applications in electrochemical sensors, catalysts, and fuel cells.

To fabricate graphene tapes with high surface areas by using the tape casting method, the pre-requirement was to prepare highly dispersed suspensions of FGSs. A triblock copolymer surfactant (ethylene oxide)$_{100}$-(propylene oxide)$_{65}$-(ethylene oxide)$_{100}$, or $EO_{100}PO_{65}EO_{100}$ in short, was used to disperse the FGSs in water. The amount of the surfactant needed to disperse the nanosheets was determined according to the concentrations of the FGSs in the supernatant of suspensions containing different amounts of surfactants, which were compared with the initial overall suspension concentrations. The amount of FGSs in the supernatant was increased with increasing concentration of the surfactant, corresponding to a

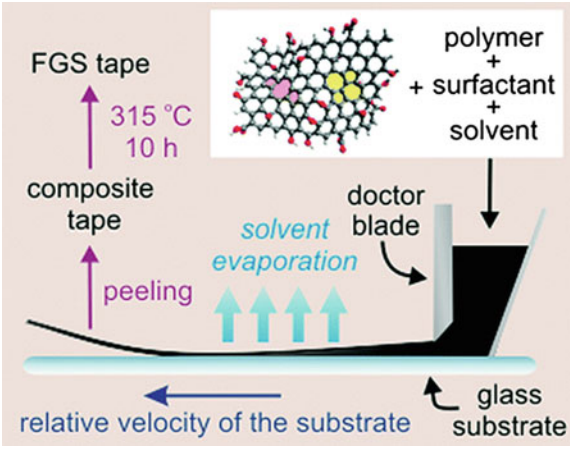

Fig. 8.11 Schematic diagram describing the fabrication of the FGS tapes with tape casting. The FGS schematic shows defective and wrinkled structure of the graphene nanosheets. Oxygen functional groups are shown in *red*, with a 5-8-5 defect in *pink* and a 5-7-7-5 defect in *yellow*. Reproduced with permission from [103], Copyright © 2011, American Chemical Society

continuous enhancement in stability of the suspensions. As the surfactant-to-FGSs ratio reached 1 (g/g), the concentration of the FGSs was saturated, implying that they were sterically stabilized suspensions, i.e., the suspension stability was increased as the surface coverage of the particles increased [130].

Hydrophobic PO chains of the $EO_{100}PO_{65}EO_{100}$ molecules were adsorbed on surfaces of the graphene nanosheets, while their hydrophilic EO chains were extended into water [131]. Due to the high solubility of EO in water, the EO chains with strong repulsive interaction among themselves acted as a barrier which prevented the FGSs from aggregation. As the surfactant molecules could not fully cover the FGSs, the strong van der Waals forces would bring them together to form aggregation. Once the FGSs were entirely covered by the surfactant molecules, their dispersion concentration would be saturated. The decrease in supernatant concentration over time implied the sedimentation of the FGSs in the suspensions. This result suggests aggregation of FGSs. This observation was mainly attributed to the van der Waals interactions if the weakly adsorbed surfactant molecules were desorbed. Because the time used for both the tape casting and drying processes was sufficiently short, and the negative effect of desorption of the triblock copolymer from the FGSs was not observed.

Besides the requirement of high-quality dispersions during the casting process, the suspensions should also have a good flowing behavior to pass through the gap between the blade and substrate under shear, as shown in Fig. 8.11. At the same time, the shape and thickness of the cast tape should be maintained as the shearing force disappeared after passing through the blade. Although these behaviors are closely related to the properties of the suspensions, effects of the substrate wettability and the contact line pinning are also significant to a certain degree. It was found that, under the shear rates used in the casting, i.e., about 100 s^{-1}, the suspensions indeed exhibited shear thinning behavior. This was simply because both the PEO solutions and the FGS suspensions had shear thinning behavior, owing to the disentanglement of the PEO molecules, the break-up of the FGS network, and the shear-induced orientation of both the FGSs and the PEO molecules [132, 133].

Viscosities of the FGS tape casting suspensions were variable over one order of magnitude at a given strain rate. The higher the concentration of FGSs, the lower the viscosity that suspensions would have. The viscosity was also increased with increasing content of PEO, so that the PEO solution with higher viscosity could be used as a thickening agent to adjust viscosity of the suspensions. As the shear rate was decreased from 100 to 1 s^{-1}, the viscosity of the suspension required 1–2 s to return. As a result, the viscosity of the suspensions was increased suddenly in several seconds when they were cast. If nonwetting substrates were used, the contact line could not be effectively pinned [134]. Consequently, the suspension would be pulled away from the substrate, thus being condensed into a formless puddle. Therefore, it is necessary to use wetting substrates to maintain the shape of tapes during evaporation of the solvents.

8.3.2.3 Electro-spray Deposition

Another approach to large area free-standing graphene papers is called direct electro-spray deposition (ESD), by combining a continuous roll-to-roll process and simple water exfoliation from highly hydrophilic aluminum substrates [104]. ESD has been widely used to deposit various thin films, because of its advantages, such as mass scale capacity, less material loss, and high precision of property controlling [135–137]. Charged mono-dispersed fine droplets are generated due to the repulsion forces among them. Size of the droplets can be well controlled by adjusting the flow rate and electric field applied to the injection nozzles and substrates, with smallest diameter to be hundreds of nanometers. The graphene papers fabricated in this way can have a wide range of thickness from hundreds of nanometers to hundreds of micrometers. They can be deposited on various substrates [138, 139].

The assembly and alignment of the graphene nanosheets in the final papers could be well controlled by controlling the ESD processing parameters and further improved through mechanical compaction upon water exfoliation. In addition, thermal annealing was employed to heal the structural defects and remove the functional groups in the graphene nanosheets, so that their thermal and electrical properties were further improved [140, 141]. It was found that the optimal thermal annealing temperature was 2200 °C, which led to defect-free, highly aligned, and light-weight (density ≈ 2.1 g cm^{-3}) graphene papers. The annealed graphene papers exhibited thermal and electrical conductivities of 1238.3 W m^{-1} K^{-1} and 1.57×10^5 S m^{-1}, respectively.

Well-dispersed graphene suspensions were used to deposit the graphene papers by using the ESD process. During the deposition, an electric voltage of 11.5 kV was applied between the injection nozzle and substrate which were separated by 2–3.5 cm to maintain a stable cone-jet mode. The graphene suspension was pushed through the nozzle at flow rates of 50–100 μl min^{-1}, by using a syringe pump, so as to generate well-dispersed fine droplets that were then deposited on the heated substrate to form a uniform film. By controlling the solution concentration and the time of deposition, films with desired thicknesses would be readily obtained. After deposition, the Al foils coated with the graphene films were immersed into water, so that free-standing graphene papers were peeled off from the substrate, as shown in Fig. 8.12a–g. The graphene papers had well-retained geometry without visible fracture.

Due to the difference in surface properties and wettability, the graphene papers could be easily peeled off from the Al foils. The Al foil was more hydrophilic than the graphene papers, as shown in Fig. 8.12j, k. When the graphene-coated Al foils were immersed in water, water molecules could penetrate the graphene films to reach the Al-graphene interface. Therefore, wet films were at the interface between the graphene layers and the hydrophilic Al substrate, so that the graphene papers were obtained when they were separated from the Al substrate.

The ESD system could be integrated with a continuous roll-to-roll process [104]. Graphene strips and graphene rolls could be produced by using the integrated system. Although the large area free-standing graphene papers were derived

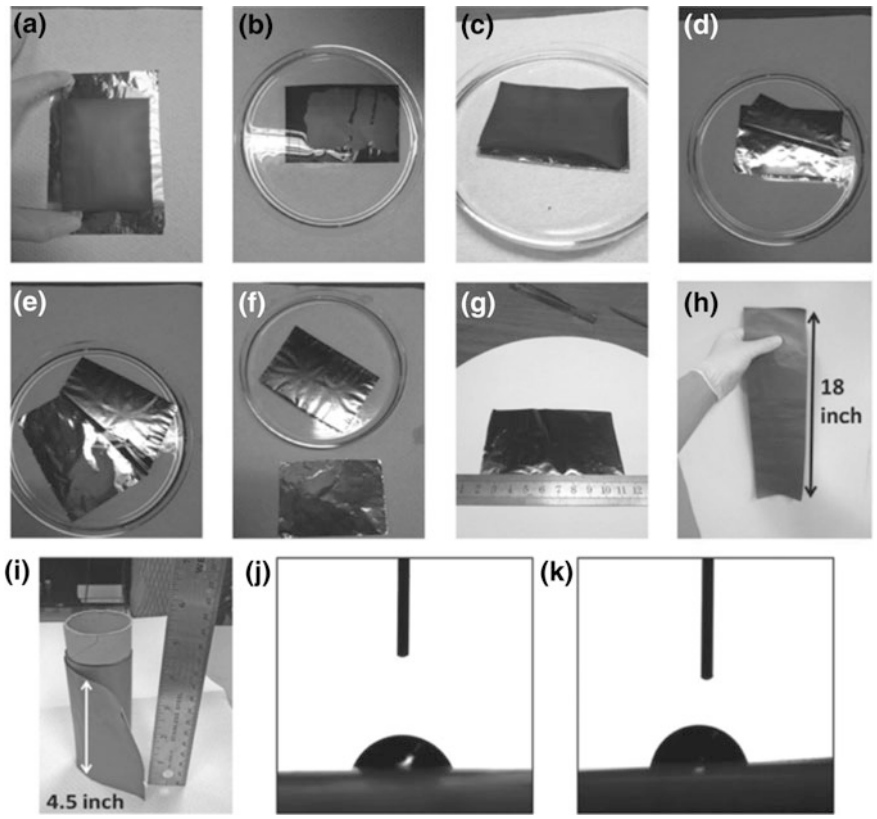

Fig. 8.12 **a** Electrospray deposited (ESD) graphene films on Al foils. **b–f** Photographs of the samples immersed in water for different time durations: **b** 30 s, **c** 2 min, **d** 4 min, **e** 7 min, and **f** 9 min. **g** Photograph of a graphene paper (9 × 6 cm^2) peeled off from the Al foil and dried at room temperature. **h**, **i** Photographs of a 18 in. graphene paper strip (**h**) and a paper roll with 4.5 in. width (**i**) made by using the ESD integrated with roll-to-roll process. **j**, **k** Contact angle measurements of the Al substrate (64°, **j**) and the graphene paper (78°, **k**). Reproduced with permission from [104], Copyright © 2014, WILEY-VCH Verlag GmbH & Co. KGaA, Weinheim

without using polymer binders, they had pretty high flexibility, so that they could be rolled without the presence of visible damage, as shown in Fig. 8.12h, i. Due to their high flexibility, the graphene papers could be processed into different shapes, with desired dimensions and geometries.

8.3.2.4 Interface Self-Assembly

Interface-induced self-assembly is also a promising method to construct graphene papers [142–145]. In this respect, the amphiphilic characteristic of GO nanosheets is beneficial to form an oriented packing at the liquid–air interface. As the thickness

is sufficiently large, free-standing GO papers could be obtained. This method has several advantages. Firstly, it is time saving and low energy consuming. For example, the GO membranes could be formed within 1 h. In contrast, the vacuum filtration method needs to take hours or even days to achieve similar thickness. Secondly, the GO suspensions could be repeatedly used, as long as the concentrations meet the requirement of membrane formation. Therefore, this process is sustainable and thus cost-effective. Thirdly, the thickness can be readily controlled by controlling the assembly time duration, while the size of the membrane simply determined by the area of the liquid–air interface, i.e., the dimension of the reactors.

A facile self-assembly approach has been reported to obtain macroscopic GO membranes at a liquid–air interface by evaporating GO hydrosols [142]. In the experiment, 200 ml GO suspension in water with a concentration of 2 mg ml^{-1} was treated ultrasonically for 30 min, followed by high-speed centrifugation at 5000 rpm for 20 min to remove impurities, as shown in Fig. 8.13a. By heating a stable hydrosol of GO to 353 K, a smooth and condensed GO thin film was formed at the liquid–air interface, as shown in Fig. 8.13b. Further drying and reduction

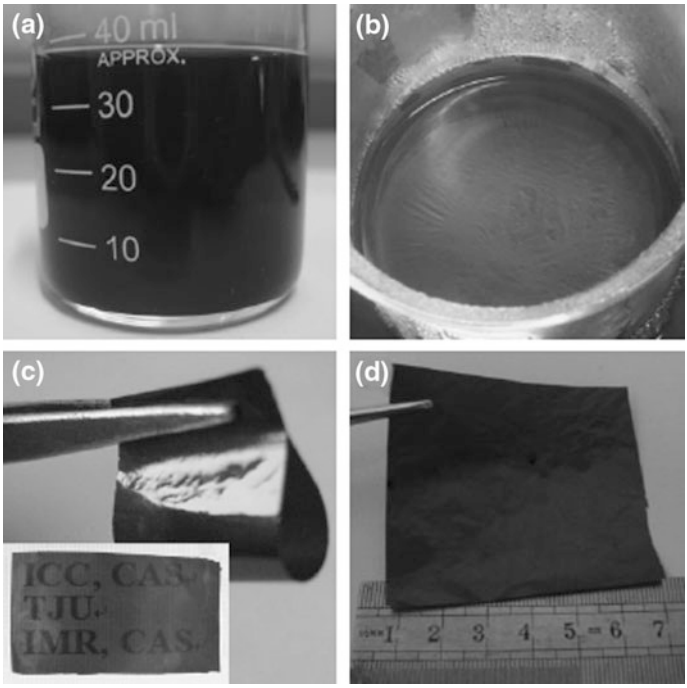

Fig. 8.13 **a** Photograph of the GO colloid suspension with a concentration of 2 mg ml^{-1} kept stable for two weeks. **b** A film self-assembled at the liquid–air interface after heating at 80 °C for 15 min. **c** Photograph of a flexible and semi-transparent GO paper (15 mm × 30 mm). **d** Photograph of a large-area (about 60 mm × 60 mm) GO paper. Reproduced with permission from [142], Copyright © 2009, WILEY-VCH Verlag GmbH & Co. KGaA, Weinheim

treatment yielded a flexible, semi-transparent, and free-standing graphene papers with thicknesses in the range 0.5–20 μm, which could be tailored by controlling the evaporation time of the hydrosol, as shown in Fig. 8.13c. For example, GO papers with thicknesses of 5 and 10 μm were obtained after heating for 20 and 40 min, respectively. The size of the flexible GO paper was only limited by the area of the liquid/air interface, so that large papers could be easily obtained by using large reaction vehicles (Fig. 8.13d).

As the hydrosol was heated, Brownian motion of the GO nanosheets was sped up in the suspension. Due to the evaporation of water, the liquid level of the hydrosol gradually decreased, so that collision and interaction among the GO nanosheets became more frequently and stronger. As a result, they migrated up to the liquid–air interface as the water molecules escaped from the hydrosol. The liquid–air interface offered a smooth space to host the 2D GO nanosheets. As the GO nanosheets reached the interface, they tended to aggregate to form a multi-layered structure. This layer would become thicker and thicker, as new GO nanosheets were transferred near to the interface and accumulated, due to the strong interlayer van der Waals interactions. XRD results indicated that the average thickness of the ordered stack was 8.2 ± 0.1 nm, implying that the stacking structure consisted of 10–11 layers of graphene oxide nanosheets. Finally, macroscopic membranes with a thickness of several micrometers were developed over the whole liquid–air interface.

8.3.2.5 Chemical Vapor Deposition (CVD)

A chemical vapor deposition (CVD) process was used to fabricate graphene papers [110]. Firstly, graphene pellets were synthesized by the CVD method, with inexpensive nickel powder as the catalyst. The graphene pellets were then processed into graphene papers by using mechanical pressing. The graphene papers exhibited high electrical conductivity of up to 1136 ± 32 S cm^{-1} and a breaking stress at 22 ± 1.4 MPa. Moreover, the graphene paper with a thickness of 50 μm demonstrated 60 dB electromagnetic interference (EMI) shielding effectiveness.

Nickel powder with average particle size of 2–3 μm and specific surface area of 0.68 m^2 g^{-1} in was pressed into pellets of 6.4 cm in diameter. The nickel pellet was placed on a quartz platform inside a quartz tube to grow graphene nanosheets by using CVD. The nickel pellet was heated up to 1000 °C in a tube furnace in Ar (1000 sccm). H_2 (325 sccm) was then purged into the tube for 15 min, to eliminate any metal catalyst oxide. After that, CH_4 was introduced for 5 min. Various hydrocarbon flow rates were tested, including 12, 15, 18, 25, and 28 sccm, corresponding to concentrations of 0.9, 1.1, 1.3, 1.9, and 2.1 vol%, respectively. The furnace was then cooled to room temperature at a rate of 100 °C min1 in Ar (1000 sccm) and H_2 (325 sccm). The nickel pellet was shrunk by about 30% after the CVD synthesis. The final 3D graphene structure in the form of the pellet was obtained by etching out the nickel from the graphene–nickel pellet with HCl (3 M) at 80 °C for 10 h. The graphene pellet was washed with water to remove residual

acid and dried at room temperature. Graphene paper was obtained by compressing the graphene pellet with a presser between two flat steel plates. Thickness of the graphene papers was controlled by controlling the compression load.

Another example of CVD processing is the development of freestanding, flexible, and transparent graphene paper (FFT-GP) from prism-like graphene (PLG) building blocks [111]. This freestanding paper possessed a large-area PLG structure, which could be transferred onto any other substrates. The PLG building blocks were connected in a face-to-face way and homogeneously aligned on silicon substrates. A single piece of FFT-GP were both highly transparent and flexible. It also maintained the electrical and physical properties of 2D graphene nanosheet, i.e., high electrical conductivity and large surface area. Such FFT-GP could find potential applications in transparent and stretchable supercapacitors.

8.4 Graphene 3D Monoliths

8.4.1 Solution Processes

For practical applications, small graphene nanosheets usually need to be constructed or assembled into macroscopic materials [146–151]. However, due to the extremely large aspect ratio, graphene nanosheets tend to aggregate or restack into the graphitic structure as they are brought together, which has been a critical issue encountered in this process. If these problems cannot be addressed, the advantageous structures and properties of graphene nanosheets cannot be well utilized as macroscopic materials. Therefore, it has been widely accepted that integration of 2D graphene nanosheets into 3D macroscopic structures, such as porous films, scaffolds, and networks, is the first step toward high-performance graphene-based materials in terms of their practical applications [10–13, 152]. In this section, the main strategies that have been used to 3D graphene architectures will be summarized.

8.4.1.1 Gelation of GO

According to polymer science and physical chemistry, CMGs are 2D amphiphilic-conjugated polyelectrolytes that consist of hydrophobic basal planes attached with hydrophilic oxygenated functional groups [153]. There is a hydrophilic–hydrophobic balance between the interplanar van der Waals force and the electrostatic repulsion, which determines the properties and thus their self-assembly behaviors of the CMGs solutions or suspensions. As discussed previously, in general, GO is soluble in water, while graphene (or rGO) nanosheets are insoluble. However, it has been found that rGO aqueous dispersion was stable at certain concentrations [154]. For example, there was a critical concentration of 0.5 mg ml^{-1}, below which stable

rGO solutions were obtained, while gelation occurred once the concentration was above this critical value. Currently, solution-based self-assembly, following the principles of colloid chemistry, has been one of the most versatile techniques reported in the open literature to develop 3D graphene architectures with hierarchical structures and special properties [152].

Gelation of GO dispersions has been acknowledged to be a simple yet feasible approach to fabricate porous 3D GO networks [155–162]. As stated earlier, GO nanosheets soluble in water due to the edge-bound carboxyl moieties, together with the large amount of hydrophilic epoxy and hydroxyl groups on their basal planes [163]. GO stable aqueous dispersion can reach concentrations of up to 10 mg ml^{-1} [164].

To promote the gelation of GO nanosheets in water suspension, various additives have been explored. One example is poly(vinyl alcohol) (PVA), which is water soluble and a widely available polymer [155]. It acted as a cross-linking agent to boost the interactions of the 2D GO nanosheets, so as to enhance the GO gelation. GO/PVA hybrid hydrogels could be derived from the mixtures of GO and PVA aqueous solutions, which were heavily shaked for 10 s and then sonicated for 20 min. The strong hydrogen bonding interaction between the hydroxyl-rich PVA chains and oxygen-containing groups on the GO nanosheets facilitated the formation of the cross-linking between the two species. Because the number of cross-linking sites was sufficiently large, stable GO composite hydrogels were produced by forming GO networks.

The gelation process was strongly influenced by the concentration of the cross-linking agent used in the experiments. GO/PVA mixtures containing 5 mg ml^{-1} GO and PVA with various weight ratios, $r_{P/G}$, were studied. For PVA, there were low critical gelation concentrations and high critical gelation concentrations. A small amount of PVA, i.e., $r_{P/G}$ = 1:20, would be able to significantly increase the viscosity of the GO solution. For the GO/PVA mixtures with 5 mg ml^{-1} GO, the gelation was only observed as the $r_{P/G}$ was in the range between 1:10 and 1:2. Further increasing the PVA content would facilitate a gel–sol transition. As $r_{P/G}$ = 1:1, viscosity of the GO/PVA mixture was close to that of pure GO solution. This observation implied that the interactions between the GO nanosheets and the PVA molecules were different in the mixtures with low and high PVA concentrations.

Pure GO, GO/PVA mixed solutions, and typical gels were lyophilized for morphological study. The freeze-dried sample derived from the 5 mg ml^{-1} GO retained its original shape and volume, while the sample from the 1 mg ml^{-1} GO demonstrated an obvious shrinkage caused by the lyophilization. Therefore, the 5 mg ml^{-1} GO suspension was like a semi-diluted solution, so that the GO volume fraction was sufficiently large to form a GO network, after all water was removed.

Figure 8.14a shows SEM image of the GO network of sheets. Similarly, all the samples with PVA could retain their volumes after the lyophilization process. If only a small amount of PVA was added into the GO solution, e.g., $r_{P/G}$ = 1:20, the morphology of lyophilized sample was not changed, i.e., the GO nanosheets were in extended states, as shown in Fig. 8.14b. The lyophilized gel derived from the

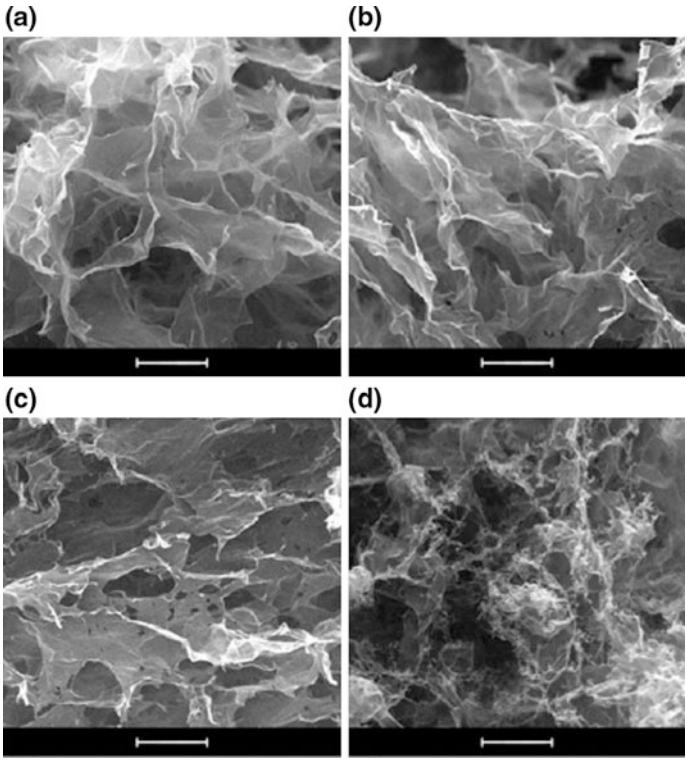

Fig. 8.14 SEM images of lyophilized 5 mg ml^{-1} GO (**a**) and GO/PVA blends (**b**–**d**) with different ratios $r_{P/G}$: **b** 1:20, **c** 1:5 and **d** 1:1. Scale bar = 5 μm. Reproduced with permission from [155], Copyright © 2010, The Royal Society of Chemistry

mixture with $r_{P/G}$ = 1:5 had a similar morphology, as shown in Fig. 8.14c. As the $r_{P/G}$ was increased to 1:1, the sample would have a different morphology after lyophilization, as shown in Fig. 8.14d. There were wire-like structures in the sample, implying that the GO nanosheets were rolled up either in the solution or during the lyophilization process.

There have been other cross-linkers for GO gelation, such as DNA [156], protein [158], synthetic polymers with cationic charges and hydrogen bonding acceptors [157, 160], small quaternary ammonium salts, and metal ions [157], through regulating the balance between the electrostatic repulsion, hydrophobic interactions, and hydrogen bonding of GO-based colloidal suspensions. In this regard, DNA is an important category of biological building blocks, which could be used to noncovalently functionalize or promote the assembly of GO nanosheets. In GO/DNA composite assemblies, single-stranded DNA (ssDNA) chains flatly would lay on surface of the GO nanosheets through π–π stacking interactions [165–167]. A simple and efficient approach was developed to trigger 3D self-assembly of GO nanosheets into multifunctional hydrogels by using in situ-formed ssDNA chains

[156]. The GO/DNA composite self-assembled hydrogels (GO/DNA SH) had a high water content of 99%. They were mechanically strong, had self-healing ability, and showed high environmental stability and dye-loading capacity.

A strategy has been developed to obtain ultralight chemically converted graphene aerogels with high compressibility [168]. In order to prevent the restacking of graphene nanosheets during the assembly progress, a functionalization-lyophilization-microwave treatment approach was strategically adopted. GO nanosheets were functionalized in a controllable way, which were then assembled into monolithic functionalized graphene hydrogel (FGH) in ethylenediamine (EDA) aqueous solution. Finally, microwave irradiation (MWI) was employed to remove the functional groups, in order to produce ultralight graphene aerogel (ULGA) that exhibited outstanding elasticity. Such aerogel could find potential applications in the areas of energy dissipation and vibration damping.

Figure 8.15a shows the synthesis steps of the graphene aerogel with extremely low density. Firstly, a basic and weak reducing agent, i.e., EDA, was mixed into the GO colloidal solution to realize the functionalization of the GO nanosheets, so that would self-assembly into 3D network. The GO suspension initially became black, then turned into sticky, and finally converted into hydrogel, as shown in Fig. 8.15b. It was observed that the final hydrogel experienced almost zero volume shrinkage after gelation. After the lyophilization process, functionalized graphene aerogel (FGA) was derived from the FGH by removing all the solvent. The FGA was further treated with MWI, thus leading to ULGA. After being treated with MWI, the aerogel had change in color from black to metallic gray, while the 3D network was

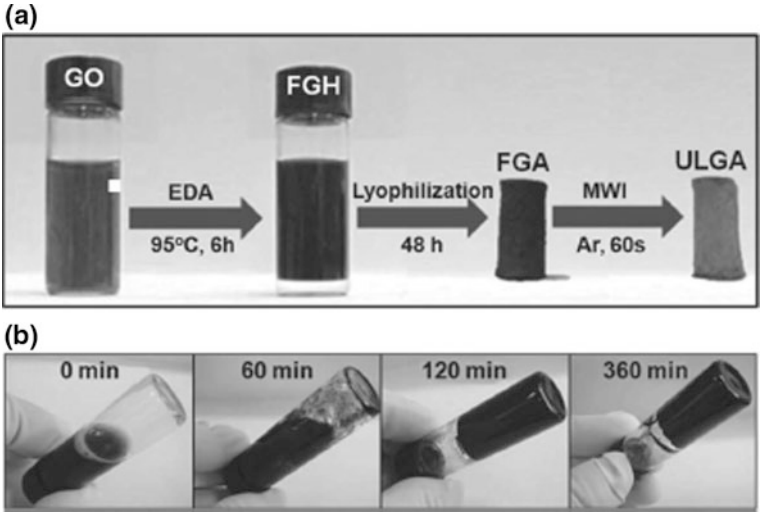

Fig. 8.15 **a** Illustration of the fabrication process of the ultralight graphene aerogel (ULGA). **b** Photographs of time-dependent formation process of the functionalized graphene hydrogel (FGH). Reproduced with permission from [168], Copyright © 2013, WILEY-VCH Verlag GmbH & Co. KGaA, Weinheim

well retained, which implied that the ULGA was sufficiently strong to survive the MWI treatment. It was readily attributed to the strong interconnection of graphene nanosheet building blocks.

A special synthetic route was devised to fabricate 3D GO hydrogels and aerogels, through self-assembly of 2D GO nanosheets that were cross-linked by using layered double hydroxides (LDHs) [169]. Recently, LDHs have formed a new class of multifunctional materials, with inorganic nanolamellar and positively charged frameworks, which have found various potential applications [170–175]. The LDH + GO hydrogels were fabricated through a one-step method, without using any hydrothermal processing or other additives. With an optimal ratio of organic and inorganic components, the Mg–Al LDHs served as a cross-linking agent, which effectively suppressed the restacking of the GO nanosheets. Instead, uniformly cross-linked GO nanosheets were assembled into 3D network structures, through various interactions, including strong hydrogen bonds and relatively weak electrostatic and cation–π interactions. The GO-based hybrid aerogels possessed strong hydrophilic behaviors and demonstrated extraordinary structural stability in aqueous solutions, thus making them for potential applications as absorbents. As a consequence, the LDH + GO hybrid aerogels exhibited strong capability to remove dyes and heavy metal pollutants from water. Due to their well-retained 3D monolithic structures, they could be easily separated, recovered, and reused.

Two sets of experiments were conducted to synthesize the LDH + GO hydrogels. In the first experiment, the amount of LDH powder was controlled at 5 mg ml^{-1}, while concentration of the homogeneous GO suspension was decreased from 5 to 1 mg ml^{-1}, so that five samples were obtained with LDH:GO ratios of 1:1, 2:1, 3:1, 4:1, and 5:1. In the second experiment, the GO concentration was fixed at 5 mg ml^{-1}, whereas the concentration of the LDH was increased from 1 to 5 mg ml^{-1}, which also led to five samples, with LDH:GO ratios of 1:5, 1:4, 1:3, 1:2, and 1:1. Once the LDHs wereadded to the GO suspensions, the mixtures were heavily shaken for homogenization and then sonicated for 1 h. The mixtures were kept at room temperature for 1 h to obtain LDH + GO hydrogels, as 3D dark-brown monoliths, which were further freeze-dried to form LDH + GO aerogels.

Figure 8.16 shows representative SEM images of the hydrogels, indicating that they consisted of porous randomly oriented 3D GO frameworks. Micro-scale morphology of the LDH + GO aerogels had a close relation to the concentration of the LDHs. It was found that the higher the concentration of the LDHs, the larger the assembled GO layers would be. For example, the pure GO aerogels contained numerous smaller GO pieces with small-sized fractals, whereas the presence of the LDHs obviously led to larger pieces, and the size was increased with increasing amount of LDHs. For instance, in the 1:1 LDH + GO aerogel, large pieces of flat sheets were observed. Therefore, it could be concluded that the LDHs had played an important role in assembling of the GO nanosheets into hydrogels with strong 3D network structures.

Additive-free GO hydrogels have been prepared by tuning pH value [157] and using ultrasonication of the GO aqueous suspensions [159]. As mentioned earlier,

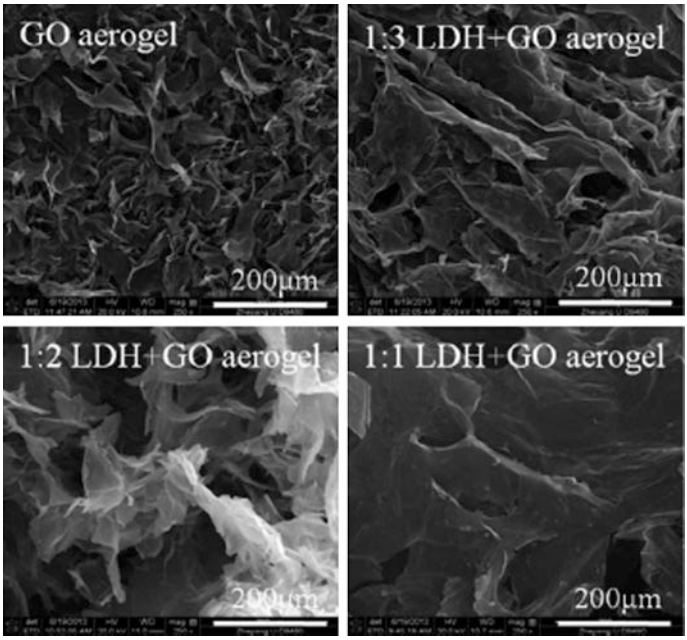

Fig. 8.16 SEM images of the pure GO aerogel and LDH + GO aerogels with various ratios of LDH and GO. Reproduced with permission from [169], Copyright © 2014, The Royal Society of Chemistry

the ionized carboxyl groups on the edges allowed the GO nanosheets to be dispersed in water through the electrostatic repulsion among them. In this case, acidification of the GO suspension would weaken the repulsion force, owing to the protonation of the carboxyl groups. It has been confirmed that GO nanosheets became unstable in a strong acidic aqueous environment, due to the insufficient mutual repulsion forces [157, 176]. As the GO concentration was sufficiently high, hydrogel could be formed, instead of the presence of an amorphous precipitation [157]. More recently, it was found that ultrasonication could be used to convert aqueous GO suspensions into hydrogels, which had much smaller channels as compared with the aerogels derived from the parent GO suspension [159]. The sonication fractured the GO aggregates into smaller fragments, so that new sheet edges were present, but without the stabilizing carboxyl groups. This surface chemistry change triggered the gelation of the GO suspensions. More importantly, such GO hydrogels exhibited very low critical gelation concentrations (CGC), in the range 0.050–0.125 mg ml^{-1}, which was dependent on the power of the ultrasonic treatment.

Purified GO aqueous suspensions (50 ml) were diluted to concentration of 2 mg ml^{-1} and sonicated with a probe sonicator set at 30% amplitude with alternating pulse and rest periods of 10 s each for different time durations (30–120 min). GO nanosheets are electrostatically stable in water due the edge-bound carboxylic

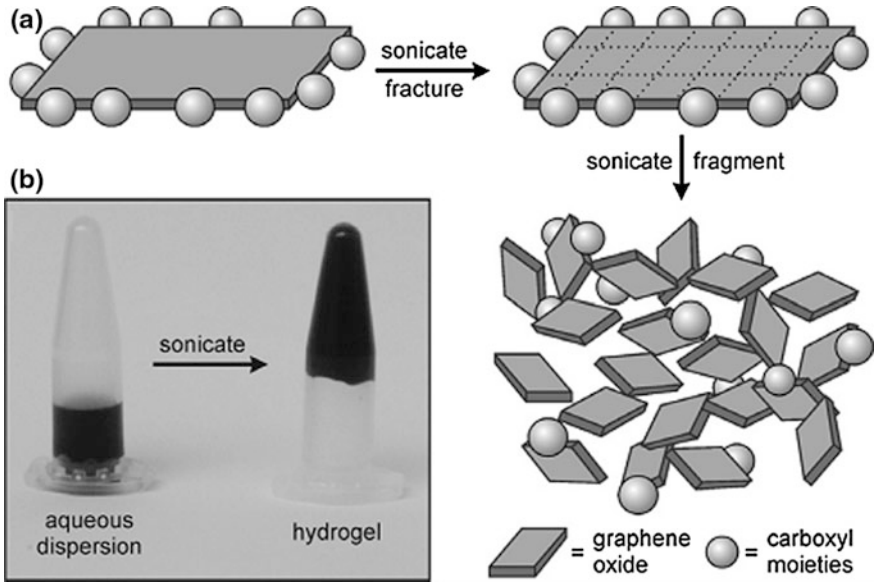

Fig. 8.17 **a** Schematic diagram illustrating the fracture and fragmentation of the GO nanosheet due to the ultrasonication, thus decreasing the coverage of carboxyl moieties (*spheres*) at the edges of the GO nanosheet fragments responsible for the gelation. **b** Photograph demonstrating the conversion of the GO aqueous suspension (*left*) into hydrogel (*right*) after the sonication treatment. Reproduced with permission from [159], Copyright © 2012, Elsevier

acid moieties. The aqueous dispersibility of GO nanosheets can be further enhanced by oxidizing the hydroxyl moieties into carboxyl groups on the basal planes. It was hypothesized that fracturing of the GO nanosheets to smaller fragments without the carboxylic acid groups along their freshly exposed edges would lead to decrease in dispersion capability, while irreversible aggregation was not induced, as shown in Fig. 8.17a.

After ultrasonication for 30 min, the dilute GO aqueous dispersion of 2 mg ml^{-1} was gelated, as shown in Fig. 8.17b. Dynamic light scattering (DLS) results indicated that average hydrodynamic diameter of the GO nanosheets was decreased from 590 to 250 nm after the ultrasonic treatment. As the sonication duration was increased to 120 min, stronger gel was formed. At the same time, hydrodynamic diameters of the GO nanosheets were further decreased to 80 nm. Although the lateral dimension of the GO nanosheets was decreased due to the ultrasonic treatment, zeta potentials of the GO suspension and the resultant hydrogels were kept almost constant at 56 ± 4 mV, which was still above the value of 30 mV required to prevent particle aggregation [154]. This suggested that the ultrasonic treatment caused negligible loss of the negatively charged functional groups. Therefore, it was more likely that the gelation was attributed to the fragmentation of the GO nanosheets that created new unfunctionalized edges which destabilized the suspensions.

In addition to the reduction in lateral size, surface chemistry of the GO nanosheets was also altered by the sonication treatment, which could be another factor to trigger the gelation of the suspensions. However, spectral characterization results, including XPS, FT-IR, and NMR, indicated that no obvious change was observed in chemical composition of GO after sonication for 120 min. This further confirmed that the destabilization of the GO nanosheets was caused by reduced carboxyl coverage at the edges of the newly formed fragments. Driving forces for the gelation included van der Waals attraction, hydrogen bonding between the functional groups, and π–π stacking of the residual sp^2-hybridized regions on the GO nanosheet basal plane. The hydrogels were fragile in nature, suggesting the weak balance between the hydrophobic interactions and hydrogen bonding.

8.4.1.2 Centrifugal Evaporation-Induced Assembly of GO

Vacuum centrifugal evaporation has been demonstrated as a strategy to fabricate additive-free GO hierarchical structures [177]. It can be used produce large-scale GO sponges with a 3D interconnected network structure. The combination of vacuum evaporation and centrifugal force sped up the solvent evaporation while retaining the sample shape and morphology due to the effect of foaming or bumping. Once 1 ml GO colloidal suspension was formed in 2 ml Eppendorf tube (Fig. 8.18a), evaporation process was initiated in a speed vacuum concentrator, so that possible sedimentation of the GO nanosheets was effectively prevented.

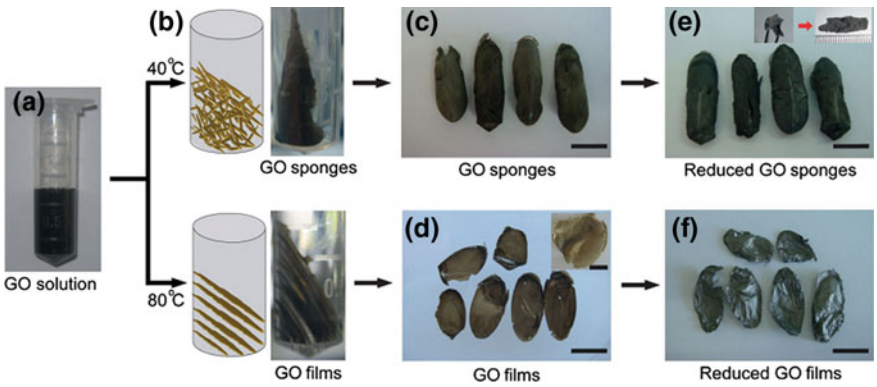

Fig. 8.18 Synthetic process of the fabrication of GO sponges and thin sheets by using the rapid vacuum centrifugation. **a** 1 ml GO solution (3 mg ml^{-1}) in a 2-ml microtube. **b** Schematic diagram showing production of the GO sponges and films at different temperatures, each with a photograph of the sample. **c** Photographs of GO sponges. **d** Free-standing GO thin sheets, with the *inset* showing photograph of the GO thin sheet with diameter of 3 cm. **e** Photographs of the rGO sponges derived from the GO sponges after thermal annealing in H_2/Ar at 800 °C for 12. **f** Free-standing graphene thin sheets. Scale bars = 1 cm (**c**–**f**). Reproduced with permission from [177], Copyright © 2010, WILEY-VCH Verlag GmbH & Co. KGaA, Weinheim

Concentration of the GO colloidal suspension was varied in the range from 2 to 5 mg ml^{-1}, at temperatures of 40, 60, and 80 °C. At the low temperature of 40 °C, the GO nanosheets were assembled into sponges with 3D porous networks. The driving force for the assembly was van der Waals forces, because during the water evaporation the outward centrifugal force was dominant over the upward evaporation force. After thermal annealing in H_2/Ar (50 cc min^{-1}) at 800 °C for 12 h, the GO sponges were reduced to graphene sponges, with large surface area and porous structure.

Figure 8.18 shows the formation process of the GO sponges and thin sheets. The experiments were started from homogeneous suspensions of single-layered GO nanosheets. The suspensions were placed on the rotor plate fixed in the vacuum chamber, with the vacuum centrifugal evaporator be operated at a rotating speed of 1800 rpm at a vacuum level of 10^{-4} torr. The as-formed GO sponges could be directly collected from the microtube by using a tweezer, which were brown in color and of a cotton-like soft morphology, as shown in Fig. 8.18c. Higher temperatures at 60 and 80 °C led to a sponge-sheet mixtures and sheets, respectively. The sponge and film morphologies were well retained after thermal reduction, with graphitic color and metallic luster, as shown in Fig. 8.18e, f. The rGO sponge exhibited high mechanical strength, as shown in the inset of Fig. 8.18e, which was obviously ascribed to the strong network structure formed by the GO nanosheets.

The individual GO nanosheets, with sizes in the range from 200 nm to 5 μm, were cross-linked to form GO-assembled network with a size of about 30 μm. The network was constructed through mainly edge-to-edge and partially edge-to-surface interactions. In the near inner wall regions of the GO sponges, there were GO nanosheets that were stacked in parallel fashion, with a relatively uniform thickness and narrow size distribution, caused by the centrifugal force. After thermal reduction, porosity of the GO sponges was reduced, while the porous structure was somehow collapsed, due to removal of the functional groups. The randomly connected morphology of the GO sponges was still retained, while the large surface area was not destroyed.

8.4.1.3 In Situ Gelation of RGO

3D rGO architecture would have more functions as compared with their GO counterparts, due to the recovered aromatic structure and thus enhanced conductivity. One of the simplest methods to develop 3D rGO architectures is self-assembly of rGO in situ. The reduction in GO increases the van der Waals forces between adjacent graphene basal planes, resulting in rGO gelation or precipitation. As stated earlier, the force balance between electrostatic repulsion and interplanar van der Waals interaction dominates the formation of rGO gels. Various reduction methods have been employed to reduce GO and trigger in situ gelation of rGO hydrogels.

Hydrothermal Reduction in GO

Hydrothermal or solvothermal reduction has been the most widely used method for such a purpose [13, 178–181]. For example, 3D rGO interconnected networks were fabricated by using a hydrothermal process with the aid of noble-metal nanocrystals (Au, Ag, Pd, Ir, Rh, Pt, etc.) [179]. The hydrothermal treatment was conducted with GO suspensions (1.0 mg ml^{-1}), together with noble-metal salt and glucose in a Teflon-lined stainless steel autoclave. The as-synthesized 3D microstructures were then freeze-dried to have good mechanical strength. Microstructures of the 3D structures, including porosity and pore size, are controlled by adjusting the GO concentration.

A simple yet effective approach has been reported to produce nanoscaled pores on graphene nanosheets by activating the graphene aerogels (GA) with H_3PO_4 [182]. Due to its mild characteristics, H_3PO_4 could be used to generate nanopores, while preventing the severe corrosion to the experimental facilities and thus mitigating the environmental problems. As schematically shown in Fig. 8.19a, the hydrothermally derived GAs in the presence of urea were impregnated with H_3PO_4 solution of different concentrations (Fig. 8.19b, c). The GAs were then subject to the activation treatment at 800 °C in the flowing N_2 gas for 90 min. The activated GA (aGA) (Fig. 8.19d) retained the macroscopic morphology of the original aerogel (Fig. 8.19c), while exhibiting an enormously enlarged specific surface area (SSA). The aGA possessed extraordinary electrochemical performance when used as electrodes of supercapacitors. They were much superior to respect to the pristine GA, in terms of specific capacitance, rate capability, and other parameters.

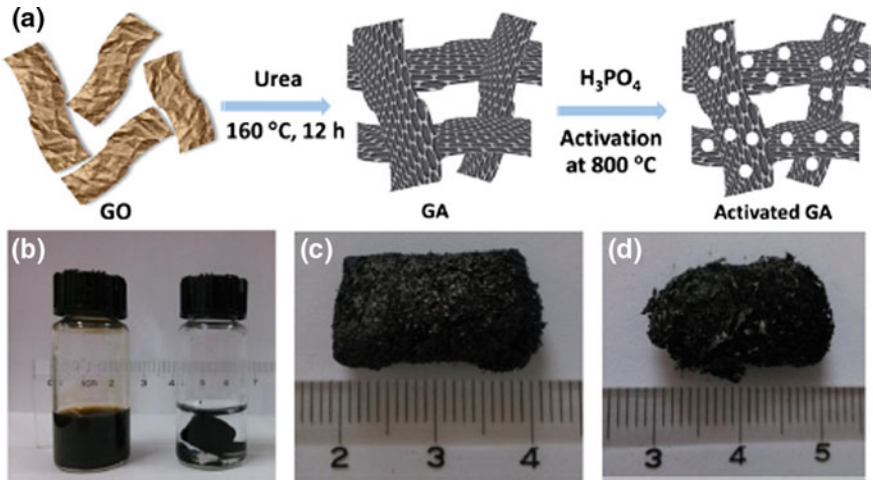

Fig. 8.19 **a** Schematic diagram showing formation process of the aGA monoliths with H_3PO_4. **b** Photographs of the GO dispersion (1 mg ml^{-1}) before and after hydrothermal reduction with urea. Photograph of the as-obtained GA (**c**) and aGA-0.5 (**d**). Reproduced with permission from [182], Copyright © 2015, Elsevier

GO suspension with a concentration of 4 mg ml^{-1} was used for the experiments. Monolith GA was first obtained by hydrothermal gelation of GO with the aid of urea. For example, 0.85 g urea and 10 ml GO suspension (4 mg ml^{-1}) were added into 30 ml water to form a diluted GO dispersion of 1 mg ml^{-1}. After stirring for 1 h, the suspension was hydrothermally treated at 160 °C for 12 h. The products were thoroughly washed with water until the pH value of the filtrate was close to 7. They were then freeze-dried for 24 h to obtain free-standing GA monoliths. The GA monoliths were impregnated with H_3PO_4 solution at concentrations of 0.2, 0.5, 1.0, and 1.2 M. After that, the samples were dried and then activated at 800 °C for 90 min in flowing N_2. The activated GA samples were labeled as aGA-x, where x is the concentration of the H_3PO_4 solution used in the impregnation experiments. In comparison, the GA sample without the H_3PO_4 impregnation was thermally annealed at 800 °C, which denoted aGA-800.

A simple hydrothermal method was developed to prepare rGO aerogels with variable and controllable surface wettability by using different amino acids as both cross-linkers and reducing agents [183]. For example, the cys-rGO aerogels obtained in the presence of L-cysteine (L-cys) were hydrophobic with extraordinary adsorption capacity to treat oil and organic solvent contaminated water, while the lys-rGO aerogels derived from L-lysine (L-lys) were hydrophilic, so as to be potential adsorbents to remove heavy metal ions from water.

It has been reported that rGO hydrogels could be directly obtained by hydrothermally treating GO aqueous suspension at appropriate concentrations without using any other reagents [13]. To prepare the self-assembled graphene hydrogels (SGH), a 2.0 mg ml^{-1} aqueous dispersion was sealed in a Teflon-lined autoclave and hydrothermally heated at 180°C for 12 h. Figure 8.20a shows the photographs of the sample before and after the hydrothermal experiment. The resulting rGO hydrogel contained 97.4 wt% water and 2.6 wt% rGO, with an interconnected 3D porous structure. The rGO hydrogels had an electrical conductive of 5×10^{-3} S cm^{-1}, high thermal stability over 25–100 °C, and high mechanical strength with storage modulus of 470 ± 20 kPa. Furthermore, its structure and properties can be easily tuned by changing the concentration of GO dispersion and hydrothermal reaction time.

Figure 8.20b shows the photographs of three SGH columns with a diameter of about 0.8 cm each, which were mechanically strong to support 100 g weight with almost no deformation. SEM images of the SGHs after freeze-drying are shown in Fig. 8.20c–e, demonstrating that they had well-developed interconnected 3D porous network structure. The pores exhibited sizes in the range from submicrometer to several micrometers, while the wall of the pore walls consisted of thin layers of tightly stacked graphene nanosheets. The formation of the physical cross-linking sites of the framework in the SGH was attributed to the partial overlapping or coalescing of the highly flexible graphene nanosheets, as shown in Fig. 8.20e. Therefore, it was the inherent flexibility of the graphene nanosheets that led to the porous 3D macrostructures.

I–V curve of the SGH is shown in Fig. 8.20f, with an Ohmic linear relationship and high electrical conductivity, due to the recovery of the π-conjugated system,

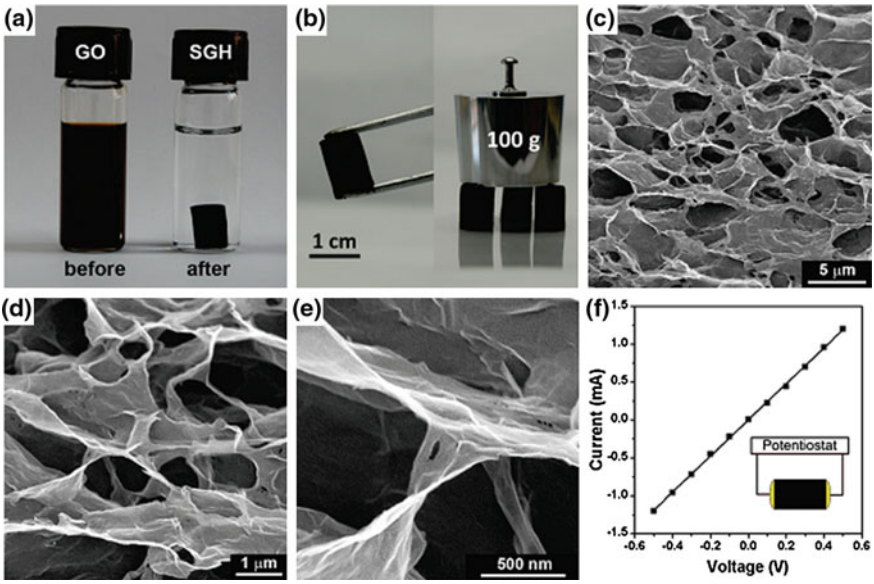

Fig. 8.20 **a** Photographs of the 2 mg ml^{-1} homogeneous GO aqueous suspension before and after hydrothermal reduction at 180 °C for 12 h. **b** Photographs of the strong SGH that could support a heavy weight. **c–e** SEM images at different magnifications of the SGHs showing their interior porous microstructures. **f** Room temperature *I–V* curve of the SGH exhibiting Ohmic characteristic, with inset showing the two-probe method for the conductivity measurement. Reproduced with permission from [13], Copyright © 2010, American Chemical Society

because the GO nanosheets were hydrothermally reduced to rGO, as confirmed by XRD patterns. The freeze-dried SGH possessed an interlayer spacing of about 3.76 Å, which was much smaller than that of the GO precursor (6.94 Å) but slightly larger than that of natural graphite (3.36 Å). This observation implied that the graphene nanosheets in the SGH took π–π stacking, while there were still residual oxygenated functional groups. With these residual hydrophilic oxygenated groups, the rGO nanosheets would encapsulate water molecules during the self-assembly process. The freeze-dried SGH exhibited a broad XRD peak, suggesting the decreased ordering of the graphene nanosheets and the presence of few-layer stacked graphene nanosheets.

Chemical Reduction in GO

Self-assembly of in situ-formed rGO through chemical reduction in GO has been extensively studied. Various reducing agents, such as sodium ascorbate [184], L-ascorbic acid [185], hypophosphorous acid–iodine [186], $NaHSO_3$ [187, 188], Na_2S, HI, and hydroquinone [187], have been used to fabricate 3D graphene architectures through the in situ self-assembly of rGO nanosheets. Similar to the

hydrothermal approaches, chemical reduction in GO promoted hydrophobic and π–π interactions between the graphene nanosheets, so as to trigger the self-assembly to 3D framework structures, with pore sizes ranging from sub-micrometer to several micrometers. Examples are discussed as follows.

High-performance 3D self-assembled graphene hydrogels (SGHs) have been fabricated through chemical reduction in aqueous GO dispersions by using sodium ascorbate as the reducing agent [184]. Pure SGHs exhibited a high specific capacitance of 240 F g^{-1}, when they were used as electrodes of supercapacitors. To prepare the SGHs, 6 ml GO aqueous suspension with a concentration of 2 mg ml^{-1} was loaded in a 15-ml glass vial, into which 24 mg sodium ascorbate was added. The sodium ascorbate was dissolved completely after sonication for 5 min, leading to a homogeneous yellow-brown solution, which was then heated at 90 °C for 1.5 h to obtain the SGH. The excess sodium ascorbate was removed through dialysis.

Figure 8.21a shows the photographs of the GO aqueous suspension (2 mg ml^{-1}), with the addition of sodium ascorbate (left), along with a piece of SGH (right). The SGHs exhibited were mechanically strong, so that they appeared as free-standing cylinders. Interior microstructures of the as-prepared SGHs were characterized by

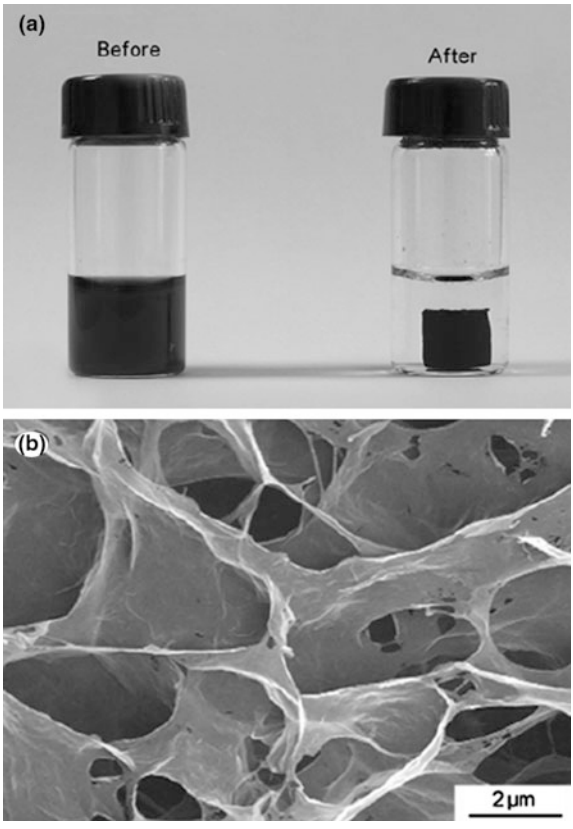

Fig. 8.21 **a** Photograph of an aqueous mixture of GO (2 mg ml^{-1}) and sodium ascorbate before (*left*) and after (*right*) chemical reduction at 90 °C for 1.5 h. **b** SEM image of SGHs. Reproduced with permission from [184], Copyright © 2011, Elsevier

using SEM. Figure 8.21b shows a representative SEM of the graphene hydrogels, in which a well-developed cross-linked 3D porous structure was clearly observed, with pores having sizes ranging from submicrometer to several micrometers.

Both microstructure and properties of the SGH were strongly dependent on several factors, including concentration (c_{GO}) of the starting GO suspensions, heating temperature, and reaction time. Among them, c_{GO} played the most important role. As the concentration of the GO suspension was too low, e.g., c_{GO} = 0.5 mg ml^{-1}, only black-colored rGO powder was formed. At intermediate concentration, e.g., c_{GO} = 0.5 mg ml^{-1}, although SGHs could be obtained, they were mechanically weak. As the concentration of the GO suspensions was increased to 2 mg ml^{-1} and above, the SGHs would have sufficiently high mechanical strength. Rheological testing results indicated that the samples derived from the suspensions with c_{GO} = 2 and 3 mg ml^{-1} had almost the same mechanical strength. Therefore, the optimal c_{GO} was 2 mg ml^{-1}. The heating temperature and reaction time could be combined to prepare mechanically strong SGHs. The heating temperature could be from room temperature to 90 °C. The higher the reaction temperature, the shorter the reaction time required.

A facile method was employed to produce chemically converted graphene xerogel (CCGX) through chemical reduction in GO suspension with the presence of hypophosphorous acid and iodine (HPA-I) at 90 °C for 12 h [186]. The reduction in GO in an aqueous solution of HPA-I resulted in stable graphene hydrogel (GH), which was then freeze-dried to form the CCGX with very low density. The CCGX possessed a C/O atomic ratio of 14.7. Due to high degree of reduction, the CCGX exhibited extraordinary electrical properties, with an electrical conductivity (EC) of about 500 S m^{-1}. More importantly, by using HPA-I as the reducing agent, the hydrogelation could be observed at a very low GO concentration of 0.5 mg ml^{-1}, so that ultralow density xerogel could be obtained by using this method.

A method to prepare 3D architectures of graphene was developed, through in situ self-assembly of graphene nanosheets that were reduced from GO by using mild chemical reduction at 95 °C and ambient pressure without stirring [187]. The reducing agents used to reduce the GO included $NaHSO_3$, Na_2S, Vitamin C, HI, and hydroquinone. Both graphene hydrogels and aerogels with 3D architectures could be fabricated by the method, while their shapes could be controlled by simply using reactors with desirable shapes. The graphene 3D architectures exhibited low density, high mechanical strength, thermal stability, electrical conductivity, and specific capacitance, thus making them promising candidates for applications in supercapacitors, hydrogen storage, and supports of catalysts.

Aqueous GO suspensions at concentrations of 0.1–2.0 mg ml^{-1} were added with various reducing agents, including $NaHSO_3$, Na_2S, Vitamin C, HI, and hydroquinone, at contents of 27–54 mmol ml^{-1}. The resultant suspensions were heated at 95 °C for 30 min or 3 h without stirring to form graphene hydrogels. The as-obtained graphene hydrogels were dialyzed against deionized water for 3 days to remove the residual inorganic compounds. To obtain aerogels, the dried graphene hydrogels were freeze-dried to remove the absorbed water molecules.

$NaHSO_3$ can be used to reduce GO in aqueous suspension, which is considered as a mild reducing agent [189]. If the reduction is conducted under stirring, the final products are aggregates or precipitates, due to the crude self-assembly of the quickly formed hydrophobic rGO nanosheets. Given the steric hindrance effect of rGO nanosheets with micrometer sizes, if the reaction is not disturbed, it is expected to produce 3D rGO architecture. With increasing degree of reduction, the partially reduced GO nanosheets would start to aggregate, owing to the increase in hydrophobicity. Some rGO nanosheets were assembled with high degree of orientation, while others could be aggregated randomly. Finally, as more and more water molecules were driven out from the aggregates, compact 3D architectures were obtained consequently.

More recently, a one-step strategy was developed to prepare macroscopic graphene–iron oxide hydrogels with 3D interconnected network structures, by using the synergistic effects of self-assembly of GO nanosheets and in situ deposition of the metal oxide nanoparticles, including α-FeOOH nanorods and magnetic Fe_3O_4 nanoparticles [190]. The GO nanosheets were reduced by the ferrous ions that acted as a reducing agent under mild conditions. The compositions of the graphene hydrogels could be readily controlled by adjusting the pH value of the starting GO suspensions. As the oil-saturated graphene–α-FeOOH superhydrophobic aerogel was burnt directly, 3D hematite α-Fe_2O_3 monoliths with porous microstructures were formed. More importantly, the separable and cost-effective graphene/metal oxide hydrogels and aerogels exhibited extraordinary capability to remove heavy metal ions and oils from water, thus making them potential candidates as efficient adsorbents in water purification and other waster-related applications.

In the experiments, a certain amount of $FeSO_4$ (0.0625–1 mmol) was quickly added into 10 ml GO aqueous suspension of 2 mg ml^{-1} in a 25-ml cylindrical sampler vial. The suspensions were then adjusted to pH = 3–11 with ammonia. All the reactions were carried out at 90 °C in an oil bath for 6 h without stirring, leading the appearance of 3D black monoliths. The samples were thoroughly washed with distilled water and freeze-dried into aerogels.

Figure 8.22a shows the photographs of the mixture of 10 ml GO suspension (2 mg ml^{-1}) and $FeSO_4$ (0.5 mmol) that was sealed in an oil bath at 90 °C for different time durations. After reaction for 0.5 h, the GO suspension became black, due to the reduction in the GO nanosheets, which were still dispersible in water. Therefore, no aggregate was observed, but the sample was slightly floating from bottom of the vessel. As the reaction time was prolonged, graphene monolith was formed and floated on top of the water. Finally, the black aggregate was further shrunk, leading to the formation of a columnar hydrogel. After reaction for 6 h, a well-developed black columnar hydrogel a diameter of 10 mm and height of 7 mm was obtained, as shown in Fig. 8.22b. No isolated graphene nanosheets were present elsewhere, so the transparent liquid was left in the vessel.

The as-synthesized graphene hydrogel contained about 95.8 wt% water, with a microstructure of well-defined and interconnected 3D network, as shown in Fig. 8.22c. The 3D network was uniformly dispersed with pores of several micrometers in size. A large number of nanoparticles were homogenously

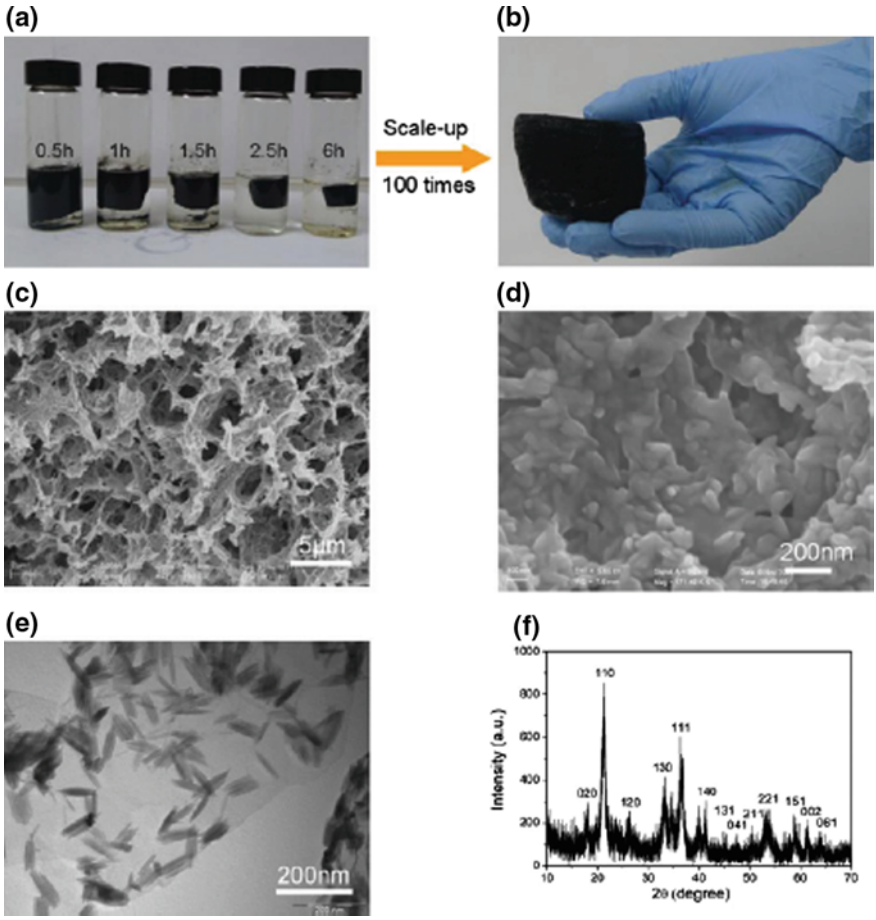

Fig. 8.22 **a** Photographs of samples after reaction for different times, showing the time-dependent formation process of the hydrogels derived from 10 ml of GO (2 mg ml^{-1}) suspensions at pH = 3 in the presence of 0.5 mmol $FeSO_4$. **b** Photograph of the hydrogels prepared by using 1000 ml GO suspension and 50 mmol $FeSO_4$. **c**, **d** Low- and high-magnification SEM images of the hydrogel. **e** TEM image of the freeze-dried graphene–α-FeOOH hydrogel. **f** XRD pattern of the graphene/α-FeOOH aerogel. Reproduced with permission from [190], Copyright © 2012, American Chemical Society

distributed on the graphene nanosheets, as shown in Fig. 8.22d. Figure 8.22e shows TEM image of the nanoparticles, which had a rod-like morphology with a size of about 60 nm. XRD pattern in Fig. 8.22f indicated that the nanoparticles were orthorhombic α-FeOOH.

Properties of the graphene–α-FeOOH hydrogels were closely dependent on the amount of the reducing agent Fe(II). The higher the content of $FeSO_4$ used in the GO suspension, the more the α-FeOOH nanorods produced in the 3D network graphene hydrogels. It was found that the graphene/α-FeOOH hydrogels were

superhydrophobic and highly porous. When they adsorbed oils and nonpolar organic solvents, water was left, so that they could be used as a suction skimmer in marine oil-spill recovery.

8.4.2 *Interface Self-Assembly*

Interface self-assembly has been shown to be an effective way to fabricate G/GO thin sheets, as discussed in last chapter. In this section, porous graphene-layered free-standing films, which have been classified as a new type of 3D architectures, are presented. These porous films have shown various advantages as compared with 3D porous scaffolds. For example, porous films can be directly used as active electrode materials for electrochemical applications without the requirement of tailoring their dimensions [191]. Various methods have been developed to fabricate graphene-based porous free-standing films, which are discussed as follows.

8.4.2.1 Breath-Figure-Templated Assembly

Breath-figure, a widely used procedure for fabricating large-area porous polymer films, has been applied to the self-assembly of polystyrene-grafted GO (PS–GO) into macroporous films [192]. GO nanosheets were self-assembled into mechanically flexible, macroporous 3D free-standing large-scale films with tunable porous microstructures. Figure 8.23a shows schematic diagram of the breath-figure method. The polymer-grafted GO nanosheets were synthesized and dispersed in an organic solvent. The dispersion was then cast onto proper substrates, which were exposed to a stream of humid air flow. Due to the evaporation of the volatile organic solvent, spontaneous condensation and close packing of aqueous droplets occurred at surface of the organic solution. Polymer-grafted GO-based macroporous films were developed on the substrates after completely drying, from which flexible robust macroporous films consisting of rGO nanosheets were derived after pyrolysis. In addition, electrical properties and chemical reactivity of the 3D rGO assemblies could be further increased by using nitrogen doping (N-doping).

The polymer-grafted GO nanosheets were prepared by using the surface-initiated atom transfer radical polymerization (ATRP) [193–195]. The polystyrene-grafted graphene oxide (PS-GO) nanosheets could be well dispersed in benzene. Drop casting the PS-GO/benzene dispersion with a concentration of 5 mg ml^{-1} onto a SiO_2 substrate resulted in highly flexible macroporous film after the evaporation of the solvent, which could be transferred to the flexible poly(ethylene terephalate) (PET) substrate, as shown in Fig. 8.23b. The film had a thickness of 3.8 μm. After pyrolysis, the GO was thermally reduced to rGO, which thus became superhydrophobic, as shown in Fig. 8.23c.

SEM images of the rGO macroporous films are shown in Fig. 8.23d, e. The sample was characterized by closely packed macropores with a nanoscale rim

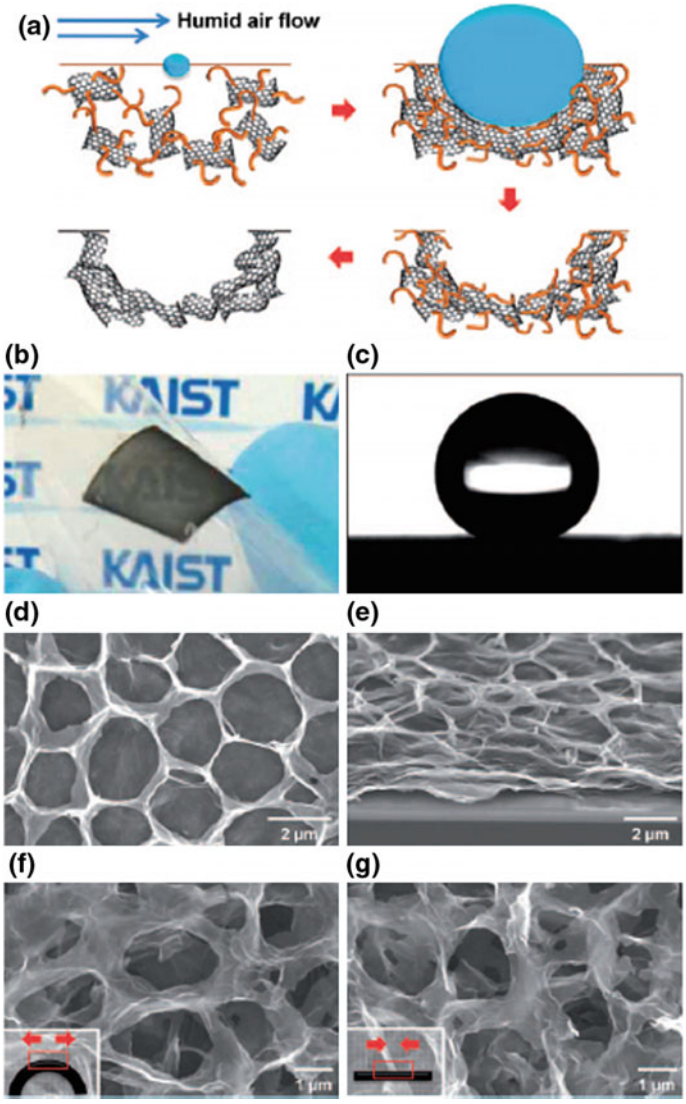

Fig. 8.23 **a** Self-assembly procedure of the rGO into macroporous free-standing films. **b** Photograph of the flexible semi-transparent macroporous rGO film on PET. **c** A water contact angle of 152° was observed for the superhydrophobic macroporous rGO film. **d** Plane view and **e** 60-tilted SEM images of the rGO film. **f**, **g** Plane view SEM images of the porous rGO film upon (**f**) and after (**g**) deformation. Reproduced with permission from [192], Copyright © 2010, Wiley-VCH Verlag GmbH & Co. KGaA, Weinheim

thickness. The rGO-assembled films were highly flexible and robust. Figure 8.23f shows a plane view SEM image of a concave film with a radius of curvature of about 2 mm, in which the pores were slightly elongated, but without damaging the macropore morphology. The porous structure was quickly recovered as the film was return to flat state, as shown in Fig. 8.23g.

8.4.2.2 Flow-Directed Self-Assembly

Leavening Strategy

More recently, another approach based on flow-directed self-assembly of GO followed by a leavening strategy was developed to prepare rGO film with 3D interconnected macroporous structures [12]. Leavening is usually a process applied for increasing the volume of breads or cakes before or during baking or steaming by forming porous structures. Leavening has been demonstrated to be an effective approach to transfer compact graphene structures into porous one, by finding a proper leavening procedure. Because unstable GO can be chemically reduced with mild heating to yield rGO, accompanied by the production of gaseous species such as H_2O and CO_2 [163, 196–198]; if the gas released during the chemical reduction in the GO could be controlled properly, rGO foams could be obtained, similar to the formation of leavened bread. It was found that the rGO foams prepared in this way possessed structures with open pores and continuous cross-links of the rGO nanosheets. They could find potential applications as electrodes of supercapacitors and absorbents for selective absorption of oil and organic solvents for clean environment.

Figure 8.24 shows a schematic diagram of the experimental procedure. In the experiment, GO aqueous dispersions with a concentration of about 2.5 mg ml^{-1} were prepared. With the suspensions, nacre-like layer-structured films were fabricated by using flow-directed assembly of the GO nanosheets. A porous anodized aluminum oxide (AAO) membrane with a pore diameter of 20 nm was used to filter the GO aqueous suspension to obtain desired samples. Therefore, thickness of GO films could be controlled by controlling concentration and volume of the GO suspensions. The films were the peeled off from the AAO membranes. The free-standing GO films were put into a Teflon (polytetrafluoroethylene) vessel of 50 ml together with 80 μl hydrazine monohydrate. To avoid direct contact, the GO films were suspended well above the hydrazine monohydrate level. Hydrothermal treatment was carried out at 90 °C for 10 h. The foam structured film experienced a 50-fold volume expansion and 30% mass loss. During the reduction in GO to rGO by the hydrazine vapor, rapid evolution of gaseous species occurred, leading the formation of the porous films. Porosity of the rGO foams could be controlled by controlling the amount of hydrazine used in the reduction reaction.

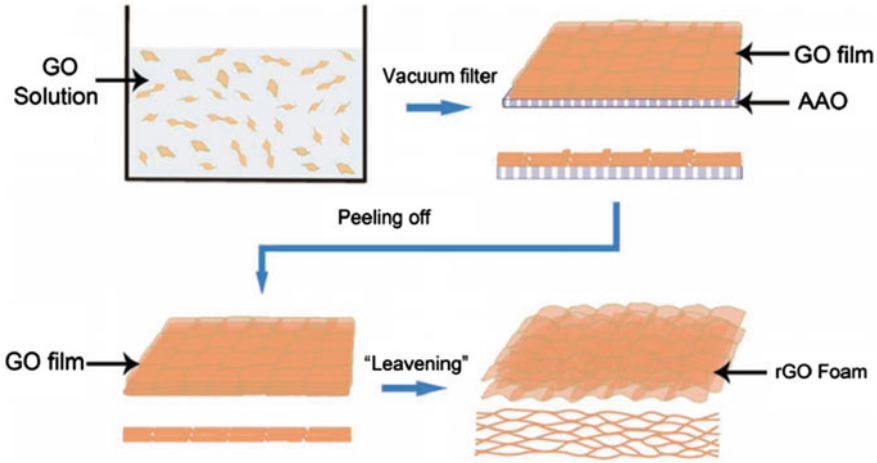

Fig. 8.24 Schematic diagram showing the leavening process to prepare the rGO foams. Reproduced with permission from [12], Copyright © 2012, Wiley-VCH Verlag GmbH & Co. KGaA, Weinheim

KOH Activation of RGO Porous Structures

Chemical activation has been shown to be a useful procedure to produce porous carbon-based materials, which has also been employed to create highly conductive and porous rGO films [199, 200]. To realize the activation, GO suspensions were added with KOH at certain concentrations. The suspensions were then heated at 100 °C to evaporate the water, thus leading to the formation a thickened "ink paste." After that, GO/KOH composite films were deposited by using vacuum filtration. After drying, the precursor films were activated in argon at 800 °C for 1 h. The activated rGO films were free standing with a smooth surface and uniform thicknesses. The flexible activated rGO porous films had a high in-plane electrical conductivity and high specific surface area. One example is discussed in more detailed way as follows.

The activated reduced graphene oxide films were named aGO [200]. The aGO films were mechanically flexible, physically free-standing, and highly porous, with an extremely high specific surface areas of 2400 $m^2\ g^{-1}$ and a very high in-plane electrical conductivity of 5880 S m^{-1}. They had a very low H content of <0.5 wt% and a high C/O atomic ratio of 14. The C/O atomic ratio was higher than that of typical chemically converted graphene nanosheets. Figure 8.25 shows schematic diagram to describe the processing steps of the film-like aGO porous thin sheets. Firstly, GO aqueous colloidal suspensions with a typical concentration of 1 mg ml^{-1} were added with 1 M KOH dropwise, which were then heated in an oil bath at 100 °C under constant stirring to evaporate the water, until an ink pastes were obtained. The pastes contained GO nanosheets evenly dispersed with KOH

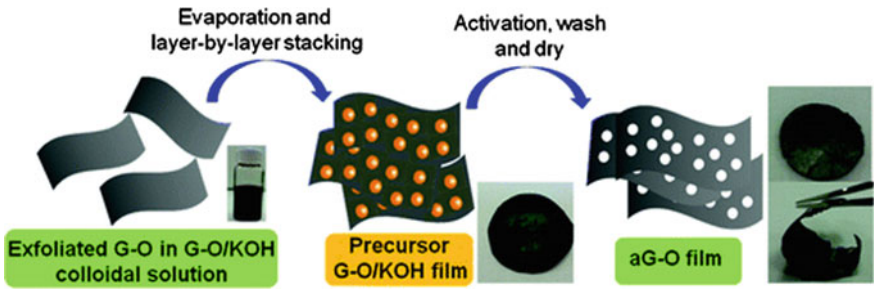

Fig. 8.25 Schematic diagram depicting the experimental steps to produce the aGO film. Reproduced with permission from [200], Copyright © 2012, American Chemical Society

together with small amount of water, which were then used to deposit films by using brief vacuum filtration with PTFE membrane.

8.4.3 Templating Approaches

Template-guided methods are also effective to develop 3D graphene architectures. This type of approaches can be used to fabricate 3D porous graphene networks, with well-defined and shaped structures in the forms of either 3D scaffolds or layered films [201–206]. The methods will be demonstrated and discussed by using four groups of samples, including template-directed CVD, ice-templating, PS colloidal temperate, and lithography method, in a detailed way.

8.4.3.1 Templated Chemical Vapor Deposition (CVD)

Various rGO samples have been fabricated by different methods, some of which could be used to produce large-scale products. However, most the rGO materials still have a relatively low electrical conductivity, which has limited their applications in some areas, especially those that require high electrical conductivity. The main reason for that is the poor quality of the graphene nanosheets made by using those methods. Chemical vapor deposition (CVD) has been acknowledged to be an effective approach to produce high-quality graphene nanosheets [207–213].

A 3D graphene macroscopic structure with a foam-like network, i.e., graphene foam (GF), has been fabricated by using a template-directed CVD method [202]. Unlike the structures formed with the chemically derived graphene nanosheets of relatively small lateral sizes, the GF fabricated by using the templated CVD method was a monolithic graphene 3D network, which facilitated charge carriers to migrate with remarkably low resistance, due to the high-quality continuous CVD-derived graphene nanosheets. Therefore, this type of GFs would have excellent electrical and mechanical properties.

8.4.3.2 Ice-Templated Unidirectional Freezing

Unidirectional freezing, also described as ice-segregation-induced self-assembly (ISISA), is a well-known wet shaping technique to form porous materials, with unique porous microstructures [214–219]. This technique has also been applied to fabricate 3D graphene macroporous scaffolds, as well as their hybrids [201, 220, 221]. Several examples are presented in the following section to demonstrate the versatility of the technique.

A template-directed method has been used to prepare graphene–polymer nanocomposites with highly ordered 3D architectures, including sponge-like macroporous scaffolds and hollow micrometer-sized spheres [201]. The sponge-like macroporous scaffolds were obtained by using the ice-segregation-induced self-assembly (ISISA) of frozen aqueous dispersions, where were homogeneous mixtures of polystyrene sulfonate grafted graphene nanosheets (PSS-G) and poly (vinylalcohol) (PVA), as shown in Fig. 8.26i. By directionally freeze casting the PSS-G or GO aqueous dispersions, free-standing monoliths with a high surface area were obtained, which were constructed by internally aligned macro- and mesoscale pores. Also, PSS-G-coated polymer microparticles or hollow micrometer-sized

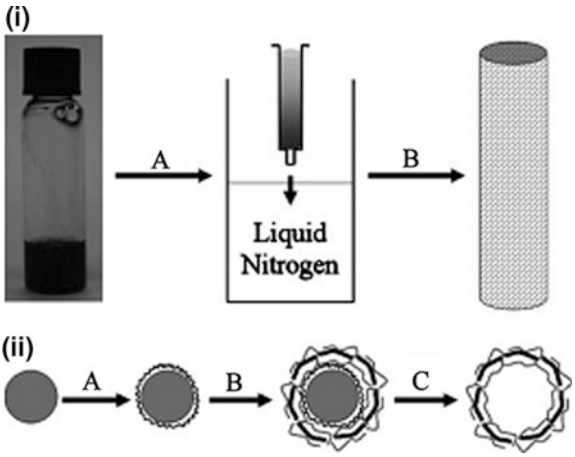

Fig. 8.26 Fabrication of the graphene–polymer nanocomposites with highly ordered 3D architectures. **i** Schematic diagram showing the formation process of the macroporous PSS-G/PVA monoliths by using the ice-segregation-induced self-assembly (ISISA): (*A*) homogeneous aqueous mixture of PVA and PSS-G (optical image) was transferred into an insulin syringe and unidirectionally frozen by immersing into liquid nitrogen at dipping rates of 2 and 5.9 mm min^{-1}, whereas (*B*) the frozen scaffold was then freeze-dried to sublime the ice crystals to produce macroporous monolith. **ii** Schematic diagram showing colloidal templating process to form the hollow PSS-G microspheres: (*A*) functionalization of the polystyrene beads with poly(allylamine hydrochloride) (PAH), (*B*) electrostatically induced templating of the negatively charged PSS-G nanosheets on the positively charged bead surface, and (*C*) removal of the core template by treatment with toluene to create hollow PSS-G microspheres. Reproduced with permission from [201], Copyright © 2009, WILEY-VCH Verlag GmbH & Co. KGaA, Weinheim

PSS-G spheres were fabricated by depositing the negatively charged PSS-G dispersions on surface of the positively charged polymer beads, as shown in Fig. 8.26ii. The PSS-G nanosheets had lateral sizes in the range from 500 nm to >1 μm and thickness of 1.5–2 nm.

In a separate study, the ISISA approach was extended to fabricate macroporous rGO–Pt/Nafion hybrid films and 3D scaffolds, in which two steps were engaged [203]. Firstly, a porous network was derived from the aqueous suspensions of Nafion, GO, and chloroplatinic acid, by using ice-templating. Secondly, the porous network was reduced to result in graphene-supported Pt nanoparticles on Nafion scaffolds. Figure 8.26i shows a schematic diagram illustrating the formation process of the ice-templating technique. The porous hybrids exhibited both ionic and electronic conductivities along with catalytic activity, making them potential candidates for fuel cell and biosensor applications.

More recently, ice-templating strategy has been employed to realize uniform distribution of nitrogen-doped graphene nanosheets, in order to achieve unique three-dimensional morphology of graphene-based materials, with enhanced electrochemical stability and ion transport network specifically for superior capacitor applications [220]. To synthesize nitrogen-doped rGO (N-rGO), 20 ml GO solution with a concentration of 5 mg ml^{-1} was diluted by adding 10 ml deionized water and sonicated for 1 h to develop a homogeneous suspension. Melamine was used as the source of nitrogen, which was dissolved in deionized water by heating at 80 °C for 30 min to form melamine solution. The GO and melamine solutions were mixed thoroughly with a mass ratio of 1:5 and then frozen in liquid nitrogen. After that, the samples were thawed following the phase diagram of water. To obtain N-rGO powder, the GO/melamine sponge type monoliths were annealed at 900 °C for 30 min in Ar. Undoped samples of rGO were prepared similarly for comparison. During annealing process, oxygen molecules were detached, which created active sites for nitrogen atoms to be incorporated into the honeycomb lattice of graphene.

8.4.4 3D Printing

The conventional manufacturing is known as subtractive process, in which unwanted portion was removed from a work piece in order to fabricate an item with desired shapes. In contrast, additive manufacturing (AM), also called 3D printing, is to create objects from 3D model data by joining materials, generally in a layer-by-layer way [222]. Therefore, 3D printing is superior over the traditional subtractive manufacturing [223–228]. For example, it can be used produce complex items and parts that are made of expensive materials. Complex items are those that have special characteristics, such as complicated geometries, internal features, engineered porosity, and material gradients. Also, it is suitable high-level customization with small scale production. More recently, 3D printing has been employed to produce graphene-based complicated items with special functionalities [229–234]. Representative examples are discussed in the following section.

Recently, electrically conductive, mechanically resilient and biocompatible scaffolds with a high graphene content of 60 vol% in solid have been developed by using 3D printing, with printable graphene inks [232]. The 3D graphene (3DG) inks were synthesized with graphene nanosheets and the biocompatible, biodegradable, and hyperelastic polyester polylactide-co-glycolide (PLG). The 3D printing was conducted at room temperature by using an extrusion method to obtain self-supporting user-defined structures with high fidelity and precision. The graphene-based structures were mechanically strong while maintaining high flexibility. Moreover, the structures had pretty high electrical conductivity, which could be used as electrically conducting scaffolds for potential applications in tissue regenerative engineering.

A 3D printing strategy has been demonstrated to fabricate 3D graphene aerogels with designed macroscopic architectures [233]. The approach was based on the precise deposition of GO ink filaments on a pre-defined tool path. Two key challenges were encountered in this process, i.e., (i) development of printable graphene-based inks and (ii) retaining the intrinsic properties of single graphene nanosheets in the final 3D printed structures, such as large specific surface area, strong mechanical properties, and high electrical conductivity.

The printed 3D graphene aerogel microlattices exhibited extraordinary structural stability and micro-architecture accuracy, as shown in Fig. 8.27a, b, which suggested that the inks possessed high quality for the 3D printing process. After the removal of the silica fillers, randomly distributed large-sized pores were left in the graphene aerogels, as shown in Fig. 8.27c, d. It also indicated that the microstructure of the 3D printed graphene aerogels could be tailored by modifying the compositions of the GO inks. It has been accepted that gelation chemistry has a significant effect on microstructural of the final hydrogels [235]. To confirm this in the 3D printed structures, two gelation reactions were examined, i.e., (i) basic solution of $(NH4)_2CO_3$ to directly cross-link the graphene nanosheets through the functional groups and (ii) resorcinol (R) and formaldehyde (F) with sodium carbonate to catalyze and link the graphene nanosheets. With the organic solgel chemistry (R–F solution), the GO networks had more open pores (Fig. 8.27d), as compared to those through the gelation based on native functionality of the GO nanosheets (Fig. 8.27c). A series of graphene aerogel microlattices with varying thickness and large area graphene aerogel honeycomb have been printed to demonstrate the versatility of the technique, as shown in Fig. 8.27e, f.

8.4.5 Miscellaneous

Spark plasma sintering (SPS) has recently been widely used to consolidate nanostructured ceramics, metals, and CNT-reinforced composites [236–240]. SPS is a sintering method that applies high pressure, high temperature, along with a pulsing current through the material during sintering [241]. The current leads to the formation of plasma in the form of micro-discharge, due to impurities on the

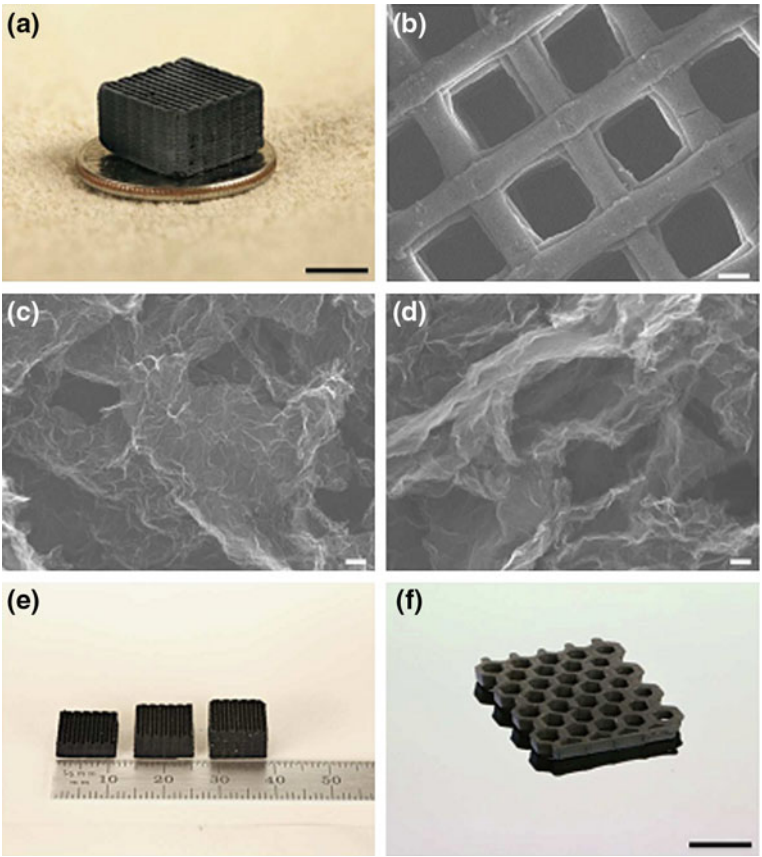

Fig. 8.27 Morphology and structure of the graphene aerogels. **a** Photograph of the 3D printed graphene aerogel microlattice. SEM images of the samples: **b** 3D printed graphene aerogel microlattice, **c** graphene aerogel without R–F after etching and **d** graphene aerogel with 4 wt% R–F after etching. **f** Photograph of the 3D printed graphene aerogel microlattices with varying thickness and **f** the 3D printed graphene aerogel honeycomb. Scale bars = 5 mm (**a**), 200 μm (**b**), 100 nm (**c**, **d**), and 1 cm (**f**). Reproduced with permission from [233], Copyright © 2015, Macmillan Publishers Limited

particle surfaces. The plasma provides with an enhanced heat transfer effect, so as to produce better bonding of the sintered materials. This technique has various advantages over the conventional sintering technologies, including high densification rate, short sintering times, controlled grain growth, and enhanced bonding between composite components. More recently, SPS has been used to consolidate graphene-reinforced composites based on aluminum oxide [242–244] and silicon nitride [245], at pressures of 35–60 MPa and temperatures of 1000–1650 °C. It was found that the SPS processing had no any negative effect on the graphene nanosheets, which were almost defect free in the composites.

Inspired by those observations, a bulk sample of graphene nanosheets has been prepared by using SPS technique at an extremely high temperature of 1850 °C and a pressure of 80 MPa [246]. Structure of the graphene nanosheets remained unchanged after the SPS processing at such an extremely high temperature. Graphene nanosheets were less vulnerable, as compared with CNTs, due probably to the special structure [247–250]. Graphene nanosheets are 2D-like, while CNTs are tubular-like. Comparatively, tubular-like structured CNTs are vulnerable to buckling and collapse at high pressures.

8.5 Concluding Remarks

Various strategies have been developed to fabricate graphene fibers, graphene papers, and bulk-like structures. Although significant progress has been made, we are facing various challenges. For instance, mechanical strength and electric conductivity of the GFs are still below the expected levels for high-performance applications. There is also a lack of standard to guide or regulate the processing of the GFs.

Obviously, the majority of free-standing 2D graphene materials have been developed by using vacuum membrane filtration, which, however, has several serious shortcomings, such as low deposition rate and limited sizes. This could restrict their practical applications, especially when large area samples are required. Therefore, solution casting or evaporation methods are expected to be more applicable in terms of large-scale production, which should be deserved for more exploration.

Various strategies and approaches have been developed to fabricate 3D graphene-based architectures, such as self-assembly, templated growth, solgel synthesis, and lithography patterning technology. There are also challenges that need to be addressed in the near future in terms of practical applications of the 3D graphene-based structures. For example, the capability of synthesizing high-quality nanosheets with desired physical and chemical properties should be established. Also, problems of restacking of the single-layer graphene building blocks, porosity and mechanical strength, purity and electrical conductivity, formation mechanisms of the 3D structures, especially for those derived from solutions or suspensions, should be paid more attention. Nevertheless, it is quite optimistic that this new group of materials will continuously be among the hot topics in terms of research.

References

1. K.S. Novoselov, A.K. Geim, S.V. Morozov, D. Jiang, Y. Zhang, S.V. Dubonos et al., Electric field effect in atomically thin carbon films. Science **306**, 666–669 (2004)

2. A. Bianco, H.M. Cheng, T. Enoki, Y. Gogotsi, R.H. Hurt, N. Koratkar et al., All in the graphene family—a recommended nomenclature for two-dimensional carbon materials. Carbon **65**, 1–6 (2013)
3. A.K. Geim, K.S. Novoselov, The rise of graphene. Nat. Mater. **6**, 183–191 (2007)
4. O.C. Compton, S.T. Nguyen, Graphene oxide, highly reduced graphene oxide, and graphene: versatile building blocks for carbon-based materials. Small **6**, 711–723 (2010)
5. J.Y. Luo, H.D. Jang, T. Sun, L. Xiao, Z. He, A.P. Katsoulidis et al., Compression and aggregation-resistant particles of crumpled soft sheets. ACS Nano **5**, 8943–8949 (2011)
6. H.H. Cheng, C.G. Hu, Y. Zhao, L.T. Qu, Graphene fiber: a new material platform for unique applications. NPG Asia Mater. **6**, e113 (2014)
7. D.Q. Wu, F.B. Zhang, H.W. Liang, X.L. Feng, Nanocomposites and macroscopic materials: assembly of chemically modified graphene sheets. Chem. Soc. Rev. **41**, 6160–6177 (2012)
8. G. Eda, M. Chhowalla, Chemically derived graphene oxide: towards large-area thin-film electronics and optoelectronics. Adv. Mater. **22**, 2392–2415 (2010)
9. J.H. Du, S.F. Pei, L.P. Ma, H.M. Cheng, 25th anniversary article: carbon nanotube- and graphene-based transparent conductive films for optoelectronic devices. Adv. Mater. **26**, 1958–1991 (2014)
10. Q.W. Chen, L.Y. Zhang, G.H. Chen, Facile preparation of graphene-copper nanoparticle composite by in situ chemical reduction for electrochemical sensing of carbohydrates. Anal. Chem. **84**, 171–178 (2012)
11. F. Yavari, Z.P. Chen, A.V. Thomas, W.C. Ren, H.M. Cheng, N. Koratkar, High sensitivity gas detection using a macroscopic three-dimensional graphene foam network. Sci. Rep. **1**, 166 (2011)
12. Z.Q. Niu, J. Chen, H.H. Hng, J. Ma, X.D. Chen, A leavening strategy to prepare reduced graphene oxide foams. Adv. Mater. **24**, 4144–4150 (2012)
13. Y.X. Xu, K.X. Sheng, C. Li, G.Q. Shi, Self-assembled graphene hydrogel via a one-step hydrothermal process. ACS Nano **4**, 4324–4330 (2010)
14. Z. Xu, C. Gao, Graphene chiral liquid crystals and macroscopic assembled fibres. Nat. Commun. **2**, 571 (2011)
15. B. Dan, N. Behabtu, A. Martinez, J.S. Evans, D.V. Kosynkin, J.M. Tour et al., Liquid crystals of aqueous, giant graphene oxide flakes. Soft Matter **7**, 11154–11159 (2011)
16. B. Konkena, S. Vasudevan, Glass, gel, and liquid crystals: arrested states of graphene oxide aqueous dispersions. J. Phys. Chem. C **118**, 21706–21713 (2014)
17. Z. Xu, C. Gao, Aqueous liquid crystals of graphene oxide. ACS Nano **5**, 2908–2915 (2011)
18. D.A. Dikin, S. Stankovich, E.J. Zimney, R.D. Piner, G.H.B. Dommett, G. Evmenenko et al., Preparation and characterization of graphene oxide paper. Nature **448**, 457–460 (2007)
19. Z. Xu, Y. Zhang, P.G. Li, C. Gao, Strong, conductive, lightweight, neat graphene aerogel fibers with aligned pores. ACS Nano **6**, 7103–7113 (2012)
20. X.Z. Hu, Z.P. Xu, Z. Liu, C. Gao, Liquid crystal self-templating approach to ultrastrong and tough biomimic composites. Sci. Rep. **3**, 2374 (2013)
21. H.B. Yao, H.Y. Fang, X.H. Wang, S.H. Yu, Hierarchical assembly of micro-/nano-building blocks: bio-inspired rigid structural functional materials. Chem. Soc. Rev. **40**, 3764–3785 (2011)
22. J.F. Wang, Q.F. Cheng, Z.Y. Tang, Layered nanocomposites inspired by the structure and mechanical properties of nacre. Chem. Soc. Rev. **41**, 1111–1129 (2012)
23. R. Jalili, S.H. Aboutalebi, D. Esrafilzadeh, R.L. Shepherd, J. Chen, S. Aminorroaya-Yamini et al., Scalable one-step wet-spinning of graphene fibers and yarns from liquid crystalline dispersions of graphene oxide: towards multifunctional textiles. Adv. Func. Mater. **23**, 5345–5354 (2013)
24. H.P. Cong, X.C. Ren, P. Wang, S.H. Yu, Wet-spinning assembly of continuous, neat, and macroscopic graphene fibers. Sci. Rep. **2**, 613 (2012)
25. L. Chen, Y.L. He, S.G. Chai, H. Qiang, F. Chen, Q. Fu, Toward high performance graphene fibers. Nanoscale **5**, 5809–5815 (2013)

26. C.S. Xiang, C.C. Young, X. Wang, Z. Yan, C.C. Hwang, G. Cerioti et al., Large flake graphene oxide fibers with unconventional 100% knot efficiency and highly aligned small flake graphene oxide fibers. Adv. Mater. **25**, 4592–4597 (2013)
27. Y. Zhao, C.C. Jiang, C.G. Hu, Z.L. Dong, J.L. Xue, Y.N. Meng et al., Large-scale spinning assembly of neat, morphology-defined, graphene-based hollow fibers. ACS Nano **7**, 2406–2412 (2013)
28. J.K. Sun, Y.H. Li, Q.Y. Peng, S.C. Hou, D.C. Zou, Y.Y. Shang et al., Macroscopic, flexible, high-performance graphene ribbons. ACS Nano **7**, 10225–10232 (2013)
29. Z.L. Dong, C.C. Jiang, H.H. Cheng, Y. Zhao, G.Q. Shi, L. Jiang et al., Facile fabrication of light, flexible and multifunctional graphene fibers. Adv. Mater. **24**, 1856–1861 (2012)
30. C.G. Hu, Y. Zhao, H.H. Cheng, Y.H. Wang, Z.L. Dong, C.C. Jiang et al., Graphene microtubings: controlled fabrication and site-specific functionalization. Nano Lett. **12**, 5879–5884 (2012)
31. X.M. Li, T.S. Zhao, K.L. Wang, Y. Yang, J.Q. Wei, F.Y. Kang et al., Directly drawing self-assembled, porous, and monolithic graphene fiber from chemical vapor deposition grown graphene film and its electrochemical properties. Langmuir **27**, 12164–12171 (2011)
32. X. Li, P.Z. Sun, L.L. Fan, M. Zhu, K.L. Wang, M.L. Zhong et al., Multifunctional graphene woven fabrics. Sci. Rep. **2**, 395 (2012)
33. C.G. Hu, X.Q. Zhai, L.L. Liu, Y. Zhao, L. Jiang, L.T. Qu, Spontaneous reduction and assembly of graphene oxide into three-dimensional graphene network on arbitrary conductive substrates. Sci. Rep. **3**, 2065 (2013)
34. D.V. Kosynkin, A.L. Higginbotham, A. Sinitskii, J.R. Lomeda, A. Dimiev, B.K. Price et al., Longitudinal unzipping of carbon nanotubes to form graphene nanoribbons. Nature **458**, 872–876 (2009)
35. L.Y. Jiao, X.R. Wang, G. Diankov, H.L. Wang, H.J. Dai, Facile synthesis of high-quality graphene nanoribbons. Nat. Nanotechnol. **5**, 321–325 (2010)
36. L.Y. Jiao, L. Zhang, X.R. Wang, G. Diankov, H.J. Dai, Narrow graphene nanoribbons from carbon nanotubes. Nature **458**, 877–880 (2009)
37. A.G. Cano-Marquez, F.J. Rodriguez-Macias, J. Campos-Delgado, C.G. Espinosa-Gonzalez, F. Tristan-Lopez, D. Ramirez-Gonzalez et al., Ex-MWNTs: graphene sheets and ribbons produced by lithium intercalation and exfoliation of carbon nanotubes. Nano Lett. **9**, 1527–1533 (2009)
38. J. Carretero-Gonzalez, E. Castillo-Martinez, M. Dias-Lima, M. Acik, D.M. Rogers, J. Sovich et al., Oriented graphene nanoribbon yarn and sheet from aligned multi-walled carbon nanotube sheets. Adv. Mater. **24**, 5695–5701 (2012)
39. C.S. Xiang, N. Behabtu, Y.D. Liu, H.G. Chae, C.C. Young, B. Genorio et al., Graphene nanoribbons as an advanced precursor for making carbon fiber. ACS Nano **7**, 1628–1637 (2013)
40. M.L. Minus, S. Kumar, The processing, properties, and structure of carbon fibers. JOM **57**, 52–58 (2005)
41. E.Y. Jang, J. Carretero-Gonzalez, A. Choi, W.J. Kim, M.E. Kozlov, T. Kim et al., Fibers of reduced graphene oxide nanoribbons. Nanotechnology **23**, 235601 (2012)
42. Z.S. Tian, C.X. Xu, J.T. Li, G.Y. Zhu, Z.L. Shi, Y. Lin, Self-assembled free-standing graphene oxide fibers. ACS Appl. Mater. Interfaces **5**, 1489–1493 (2013)
43. R.H. Baughman, C.X. Cui, A.A. Zakhidov, Z. Iqbal, J.N. Barisci, G.M. Spinks et al., Carbon nanotube actuators. Science **284**, 1340–1344 (1999)
44. F. Hennrich, S. Lebedkin, S. Malik, J. Tracy, M. Barczewski, H. Rosner et al., Preparation, characterization and applications of free-standing single walled carbon nanotube thin films. Phys. Chem. Chem. Phys. **4**, 2273–2277 (2002)
45. H. Chen, M.B. Muller, K.J. Gilmore, G.G. Wallace, D. Li, Mechanically strong, electrically conductive, and biocompatible graphene paper. Adv. Mater. **20**, 3557–3561 (2008)
46. W.B. Hu, C. Peng, W.J. Luo, M. Lv, X.M. Li, D. Li et al., Graphene-based antibacterial paper. ACS Nano **4**, 4317–4323 (2010)

47. G.Y. He, H.Q. Chen, J.W. Zhu, F.L. Bei, X.Q. Sun, X. Wang, Synthesis and characterization of graphene paper with controllable properties via chemical reduction. J. Mater. Chem. **21**, 14631–14638 (2011)
48. M. Lian, J.C. Fan, Z.X. Shi, S. Zhang, H. Li, J. Yin, Gelatin-assisted fabrication of graphene-based nacre with high strength, toughness, and electrical conductivity. Carbon **89**, 279–289 (2015)
49. H. Gwon, H.S. Kim, K.U. Lee, D.H. Seo, Y.C. Park, Y.S. Lee et al., Flexible energy storage devices based on graphene paper. Energy Environ. Sci. **4**, 1277–1283 (2011)
50. X.W. Yang, L. Qiu, C. Cheng, Y.Z. Wu, Z.F. Ma, D. Li, Ordered gelation of chemically converted graphene for next-generation electroconductive hydrogel films. Angew. Chem. Int. Ed. **50**, 7325–7328 (2011)
51. Q.F. Cheng, M.X. Wu, M.Z. Li, L. Jiang, Z.Y. Tang, Ultratough artificial nacre based on conjugated cross-linked graphene oxide. Angew. Chem. Int. Ed. **52**, 3750–3755 (2013)
52. S.J. Park, K.S. Lee, G. Bozoklu, W.W. Cai, S.T. Nguyen, R.S. Ruoff, Graphene oxide papers modified by divalent ions—enhancing mechanical properties via chemical cross-linking. ACS Nano **2**, 572–578 (2008)
53. K.W. Putz, O.C. Compton, C. Segar, Z. An, S.T. Nguyen, L.C. Brinson, Evolution of order during vacuum-assisted self-assembly of graphene oxide paper and associated polymer nanocomposites. ACS Nano **5**, 6601–6609 (2011)
54. A. Sumboja, C.Y. Foo, X. Wang, P.S. Lee, Large areal mass, flexible and free-standing reduced graphene oxide/manganese dioxide paper for asymmetric supercapacitor device. Adv. Mater. **25**, 2809–2815 (2013)
55. Y. Tian, Y.W. Cao, Y. Wang, W.L. Yang, J.C. Feng, Realizing ultrahigh modulus and high strength of macroscopic graphene oxide papers through crosslinking of mussel-inspired polymers. Adv. Mater. **25**, 2980–2983 (2013)
56. W. Guo, C. Cheng, Y.Z. Wu, Y.N. Jiang, J. Gao, D. Li et al., Bio-inspired two-dimensional nanofluidic generators based on a layered graphene hydrogel membrane. Adv. Mater. **25**, 6064–6068 (2013)
57. H.Y. Liu, H.T. Wang, X.W. Zhang, Facile fabrication of freestanding ultrathin reduced graphene oxide membranes for water purification. Adv. Mater. **27**, 249–254 (2015)
58. D.D. Han, Y.L. Zhang, H.B. Jiang, H. Xia, J. Feng, Q.D. Chen et al., Moisture-responsive graphene paper prepared by self-controlled photoreduction. Adv. Mater. **27**, 332–338 (2015)
59. S.H. Ha, Y.S. Jeong, Y.J. Lee, Free standing reduced graphene oxide film cathodes for lithium ion batteries. ACS Appl. Mater. Interfaces **5**, 12295–12303 (2013)
60. Z.L. Hou, W.L. Song, P. Wang, M.J. Meziani, C.Y. Kong, A. Anderson et al., Flexible graphene-graphene composites of superior thermal and electrical transport properties. ACS Appl. Mater. Interfaces **6**, 15026–15032 (2014)
61. Y.F. Li, Y.Z. Liu, W.Z. Shen, Y.G. Yang, M.Z. Wang, Y.F. Wen, Free-standing optoelectronic graphene-CdS-graphene oxide composite paper produced by vacuum-assisted self-assembly. Appl. Phys. A-Mater. Sci. Process. **106**, 779–784 (2012)
62. J.L. Xiang, L.T. Drzal, Thermal conductivity of exfoliated graphite nanoplatelet paper. Carbon **49**, 773–778 (2011)
63. C. Valles, J.D. Nunez, A.M. Benito, W.K. Maser, Flexible conductive graphene paper obtained by direct and gentle annealing of graphene oxide paper. Carbon **50**, 835–844 (2012)
64. S. Park, J.W. Suk, J.H. An, J. Oh, S. Lee, W. Lee et al., The effect of concentration of graphene nanoplatelets on mechanical and electrical properties of reduced graphene oxide papers. Carbon **50**, 4573–4578 (2012)
65. W. Lee, J.U. Lee, B.M. Jung, J.H. Byun, J.W. Yi, S.B. Lee et al., Simultaneous enhancement of mechanical, electrical and thermal properties of graphene oxide paper by embedding dopamine. Carbon **65**, 296–304 (2013)
66. D.Y. Kim, M.K. Kim, D.W. Kim, J.D. Suk, O.O. Park, Y.K. Kang, Flexible binder-free graphene paper cathodes for high-performance Li-O_2 batteries. Carbon **93**, 625–635 (2015)

67. L. Paliotta, G. De Bellis, A. Tamburrano, F. Marra, A. Rinaldi, S.K. Balijepalli et al., Highly conductive multilayer-graphene paper as a flexible lightweight electromagnetic shield. Carbon **89**, 260–271 (2015)
68. P. Kumar, F. Shahzad, S.G. Yu, S.M. Hong, Y.H. Kim, C.M. Koo, Large-area reduced graphene oxide thin film with excellent thermal conductivity and electromagnetic interference shielding effectiveness. Carbon **94**, 494–500 (2015)
69. S. Stankovich, D.A. Dikin, O.C. Compton, G.H.B. Dommett, R.S. Ruoff, S.T. Nguyen, Systematic post-assembly modification of graphene oxide paper with primary alkylamines. Chem. Mater. **22**, 4153–4157 (2010)
70. P. He, J. Sun, S.Y. Tian, S.W. Yang, S.J. Ding, G.Q. Ding et al., Processable aqueous dispersions of graphene stabilized by graphene quantum dots. Chem. Mater. **27**, 218–226 (2015)
71. X.Q. Zhang, S.H. Wan, J.B. Pu, L.P. Wang, X.Q. Liu, Highly hydrophobic and adhesive performance of graphene films. J. Mater. Chem. **21**, 12251–12258 (2011)
72. C. Zhang, W.W. Tjiu, W. Fan, Z. Yang, S. Huang, T.X. Liu, Aqueous stabilization of graphene sheets using exfoliated montmorillonite nanoplatelets for multifunctional free-standing hybrid films via vacuum-assisted self-assembly. J. Mater. Chem. **21**, 18011–18017 (2011)
73. S.D. Zhang, Q.H. Tao, Z.Y. Wang, Z.P. Zhang, Controlled heat release of new thermal storage materials: the case of polyethylene glycol intercalated into graphene oxide paper. J. Mater. Chem. **22**, 20166–20169 (2012)
74. G.Q. Ning, C.G. Xu, Y.M. Cao, X. Zhu, Z.M. Jiang, Z.J. Fan et al., Chemical vapor deposition derived flexible graphene paper and its application as high performance anodes for lithium rechargeable batteries. J. Mater. Chem. A **1**, 408–414 (2013)
75. K.W. Shu, C.Y. Wang, S. Li, C. Zhao, Y. Yang, H.K. Liu et al., Flexible free-standing graphene paper with interconnected porous structure for energy storage. J. Mater. Chem. A **3**, 4428–4434 (2015)
76. C. Cheng, J.W. Zhu, X.W. Yang, L. Qiu, Y.F. Wang, D. Li, Dynamic electrosorption analysis: a viable liquid-phase characterization method for porous carbon? J. Mater. Chem. A **1**, 9332–9340 (2013)
77. J.U. Lee, W. Lee, J.W. Yi, S.S. Yoon, S.B. Lee, B.M. Jung et al., Preparation of highly stacked graphene papers via site-selective functionalization of graphene oxide. J. Mat. Chem. A **1**, 12893–12899 (2013)
78. Z.Q. Jiang, Y.L. Shi, Z.J. Jiang, X.N. Tian, L.J. Luo, W.H. Chen, High performance of a free-standing sulfonic acid functionalized holey graphene oxide paper as a proton conducting polymer electrolyte for airbreathing direct methanol fuel cells. J. Mater. Chem. A **2**, 6494–6503 (2014)
79. W.L. Song, X.T. Guan, L.Z. Fan, W.Q. Cao, C.Y. Wang, Q.L. Zhao et al., Magnetic and conductive graphene papers toward thin layers of effective electromagnetic shielding. J. Mater. Chem. A **3**, 2097–2107 (2015)
80. Q. Liu, L.Q. Liu, K. Xie, Y.N. Meng, H.P. Wu, G.R. Wang et al., Synergistic effect of a rGO/PANI nanocomposite electrode based air working ionic actuator with a large actuation stroke and long-term durability. J. Mater. Chem. A. **3**, 8380–8388 (2015)
81. J.F. Ping, Y.X. Wang, K. Fan, W.Z. Tang, J. Wu, Y.B. Ying, High-performance flexible potentiometric sensing devices using free-standing graphene paper. J. Mater. Chem. B **1**, 4781–4791 (2013)
82. I.W.P. Chen, S.H. Saint Jhou, W. Chen, Preparation of high-quality graphene sheets and their applications in highly conductive papers and a high-performance electromechanical actuator. J. Mater. Chem. C **1**, 5970–5975 (2013)
83. A. Abouimrane, O.C. Compton, K. Amine, S.T. Nguyen, Non-annealed graphene paper as a binder-free anode for lithium-ion batteries. J. Phys. Chem. C **114**, 12800–12804 (2010)
84. J.Q. Liu, R. Wang, L. Cui, J.G. Tang, Z. Liu, Q.S. Kong et al., Using molecular level modification to tune the conductivity of graphene papers. J. Phys. Chem. C **116**, 17939–17946 (2012)

85. J.M. Zhu, L.W. Zhu, Z.F. Lu, L. Gu, S.L. Cao, X.B. Cao, Selectively expanding graphene oxide paper for creating multifunctional carbon materials. J. Phys. Chem. C **116**, 23075–23082 (2012)
86. T. Cetinkaya, S. Ozcan, M. Uysal, M.O. Guler, H. Akbulut, Free-standing flexible graphene oxide paper electrode for rechargeable Li-O_2 batteries. J. Power Sources **267**, 140–147 (2014)
87. M.H. Yang, S.H. Ko, J.S. Im, B.G. Choi, Free-standing molybdenum disulfide/graphene composite paper as a binder- and carbon-free anode for lithium-ion batteries. J. Power Sources **288**, 76–81 (2015)
88. H.B. Huang, Z.G. Song, N. Wei, L. Shi, Y.Y. Mao, Y.L. Ying et al., Ultrafast viscous water flow through nanostrand-channelled graphene oxide membranes. Nat. Communi. **4**, 2979 (2013)
89. Y.X. Xu, C.Y. Chen, Z.P. Zhao, Z.Y. Lin, C. Lee, X. Xu et al., Solution processable holey graphene oxide and Its derived macrostructures for high-performance supercapacitors. Nano Lett. **15**, 4605–4610 (2015)
90. D. Zhong, Q.L. Yang, L. Guo, S.X. Dou, K.S. Liu, L. Jiang, Fusion of nacre, mussel, and lotus leaf: bio-inspired graphene composite paper with multifunctional integration. Nanoscale **5**, 5758–5764 (2013)
91. A.B. Dichiara, T.J. Sherwood, J. Benton-Smith, J.C. Wilson, S.J. Weinstein, R.E. Rogers, Free-standing carbon nanotube/graphene hybrid papers as next generation adsorbents. Nanoscale **6**, 6322–6327 (2014)
92. X.Y. Huang, C.Y. Zhi, P.K. Jiang, D. Golberg, Y. Bando, T. Tanaka, Temperature-dependent electrical property transition of graphene oxide paper. Nanotechnology **23**, 455705 (2012)
93. H. Bi, J. Chen, W. Zhao, S.R. Sun, Y.F. Tang, T.Q. Lin et al., Highly conductive, free-standing and flexible graphene papers for energy conversion and storage devices. RSC Adv. **3**, 8454–8460 (2013)
94. S.J. Park, J.H. An, J.W. Suk, R.S. Ruoff, Graphene-Based Actuators. Small **6**, 210–212 (2010)
95. J.W. Zhang, G. Shi, C. Jiang, S. Ju, D.Z. Jiang, 3D bridged carbon nanoring/graphene hybrid paper as a high-performance lateral heat spreader. Small **11**, 6197–6204 (2015)
96. F. Xiao, Y.Q. Li, H.C. Gao, S.B. Ge, H.W. Duan, Growth of coral-like PtAu-MnO_2 binary nanocomposites on free-standing graphene paper for flexible nonenzymatic glucose sensors. Biosens. Bioelectron. **41**, 417–423 (2013)
97. F. Xiao, J.B. Song, H.C. Gao, X.L. Zan, R. Xu, H.W. Duan, Coating graphene paper with 2D-assembly of electrocatalytic nanoparticles: a modular approach toward high-performance flexible electrodes. ACS Nano **6**, 100–110 (2012)
98. W. Cui, M.Z. Li, J.Y. Liu, B. Wang, C. Zhang, L. Jiang et al., A strong integrated strength and toughness artificial nacre based on dopamine cross-linked graphene oxide. ACS Nano **8**, 9511–9517 (2014)
99. F. Xiao, Y.Q. Li, X.L. Zan, K. Liao, R. Xu, H.W. Duan, Growth of metal-metal oxide nanostructures on freestanding graphene paper for flexible biosensors. Adv. Func. Mater. **22**, 2487–2494 (2012)
100. B. Shen, W.T. Zhai, W.G. Zheng, Ultrathin flexible graphene film: An excellent thermal conducting material with efficient EMI shielding. Adv. Func. Mater. **24**, 4542–4548 (2014)
101. M. Zhang, L. Huang, J. Chen, C. Li, G.Q. Shi, Ultratough, ultrastrong, and highly conductive graphene films with arbitrary sizes. Adv. Mater. **26**, 7588–7592 (2014)
102. S.J. Yang, J.H. Kang, H.S. Jung, T.H. Kim, C.R. Park, Preparation of a freestanding, macroporous reduced graphene oxide film as an efficient and recyclable sorbent for oils and organic solvents. J. Mater. Chem. A **1**, 9427–9432 (2013)
103. S. Korkut, J.D. Roy-Mayhew, D.M. Dabbs, D.L. Milius, I.A. Aksay, High surface area tapes produced with functionalized graphene. ACS Nano **5**, 5214–5222 (2011)
104. G.Q. Xin, H.T. Sun, T. Hu, H.R. Fard, X. Sun, N. Koratkar et al., Large-area freestanding graphene paper for superior thermal management. Adv. Mater. **26**, 4521–4526 (2014)

105. M. Wang, D. Le Dai, J.S. Oh, M. Nguyen Thi, S.H. Kim, S.C. Hong et al., Large-area, conductive and flexible reduced graphene oxide (rGO) membrane fabricated by electrophoretic deposition (EPD). ACS Appl. Mater. Interfaces **6**, 1747–1753 (2014)
106. S.Y. Liu, K. Chen, Y. Fu, S.Y. Yu, Z.H. Bao, Reduced graphene oxide paper by supercritical ethanol treatment and its electrochemical properties. Appl. Surf. Sci. **258**, 5299–5303 (2012)
107. C.M. Chen, J.Q. Huang, Q. Zhang, W.Z. Gong, Q.H. Yang, M.Z. Wang et al., Annealing a graphene oxide film to produce a free standing high conductive graphene film. Carbon **50**, 659–667 (2012)
108. K.W. Shu, C.Y. Wang, M. Wang, C. Zhao, G.G. Wallace, Graphene cryogel papers with enhanced mechanical strength for high performance lithium battery anodes. J. Mater. Chem. A **2**, 1325–1331 (2014)
109. I.F. Cheng, Y.Q. Xie, R.A. Gonzales, P.R. Brejna, J.P. Sundararajan, B.A.F. Kengne et al., Synthesis of graphene paper from pyrolyzed asphalt. Carbon **49**, 2852–2861 (2011)
110. L. Zhang, N.T. Alvarez, M.X. Zhang, M. Haase, R. Malik, D. Mast et al., Preparation and characterization of graphene paper for electromagnetic interference shielding. Carbon **82**, 353–359 (2015)
111. N. Li, G.Z. Yang, Y. Sun, H.W. Song, H. Cui, G.W. Yang et al., Free-standing and transparent graphene membrane of polyhedron box-shaped basic building units directly grown using a NaCl template for flexible transparent and stretchable solid-state supercapacitors. Nano Lett. **15**, 3195–3203 (2015)
112. A. Lerf, A. Buchsteiner, J. Pieper, S. Schottl, I. Dekany, T. Szabo et al., Hydration behavior and dynamics of water molecules in graphite oxide. J. Phys. Chem. Solids **67**, 1106–1110 (2006)
113. R. Mukherjee, A.V. Thomas, A. Krishnamurthy, N. Koratkar, Photothermally reduced graphene as high-power anodes for lithium-ion batteries. ACS Nano **6**, 7867–7878 (2012)
114. Y.H. Hu, X.F. Li, D.S. Geng, M. Cai, R.Y. Li, X.L. Sun, Influence of paper thickness on the electrochemical performances of graphene papers as an anode for lithium ion batteries. Electrochim. Acta **91**, 227–233 (2013)
115. X. Zhao, C.M. Hayner, M.C. Kung, H.H. Kung, Flexible holey graphene paper electrodes with enhanced rate capability for energy storage applications. ACS Nano **5**, 8739–8749 (2011)
116. Z.H. Jin, P. Owour, S.D. Lei, L.H. Ge, Graphene, graphene quantum dots and their applications in optoelectronics. Curr. Opin. Colloid Interface Sci. **20**, 439–453 (2015)
117. X.J. Zhou, S.W. Guo, J.Y. Zhang, Solution-processable graphene quantum dots. ChemPhysChem **14**, 2627–2640 (2013)
118. I. Ozfidan, M. Korkusinski, P. Hawrylak, Electronic properties and electron-electron interactions in graphene quantum dots. Phys. Status Solidi-Rapid Res. Lett. **10**, 13–23 (2016)
119. J. Peng, W. Gao, B.K. Gupta, Z. Liu, R. Romero-Aburto, L.H. Ge et al., Graphene puantum dots derived from carbon fibers. Nano Lett. **12**, 844–849 (2012)
120. S.W. Yang, J. Sun, X.B. Li, W. Zhou, Z.Y. Wang, P. He et al., Large-scale fabrication of heavy doped carbon quantum dots with tunable-photoluminescence and sensitive fluorescence detection. J. Mater. Chem. A **2**, 8660–8667 (2014)
121. N.V. Medhekar, A. Ramasubramaniam, R.S. Ruoff, V.B. Shenoy, Hydrogen bond networks in graphene oxide composite paper: structure and mechanical properties. ACS Nano **4**, 2300–2306 (2010)
122. K.W. Putz, O.C. Compton, M.J. Palmeri, S.T. Nguyen, L.C. Brinson, High-nanofiller-content graphene oxide-polymer nanocomposites via vacuum-assisted self-assembly. Adv. Func. Mater. **20**, 3322–3329 (2010)
123. X.W. Yang, C. Cheng, Y.F. Wang, L. Qiu, D. Li, Liquid-mediated dense integration of graphene materials for compact capacitive energy storage. Science **341**, 534–537 (2013)

124. O.C. Compton, D.A. Dikin, K.W. Putz, L.C. Brinson, S.T. Nguyen, Electrically conductive "alkylated" graphene paper via chemical reduction of amine-functionalized graphene oxide paper. Adv. Mater. **22**, 892–896 (2010)
125. I. Dekany, R. Kruger-Grasser, A. Weiss, Selective liquid sorption properties of hydrophobized graphite oxide nanostructures. Colloid Polym. Sci. **276**, 570–576 (1998)
126. S. Park, N. Mohanty, J.W. Suk, A. Nagaraja, J.H. An, R.D. Piner et al., Biocompatible, robust free-standing paper composed of a TWEEN/graphene composite. Adv. Mater. **22**, 17361740 (2010)
127. J.J. Liang, Y.F. Xu, D. Sui, L. Zhang, Y. Huang, Y.F. Ma et al., Flexible, magnetic, and electrically conductive graphene/Fe_3O_4 paper and its application for magnetic-controlled switches. J. Phys. Chem. C **114**, 17465–17471 (2010)
128. R. Rozada, J.I. Paredes, S. Villar-Rodil, A. Martinez-Alonso, J.M.D. Tascon, Towards full repair of defects in reduced graphene oxide films by two-step graphitization. Nano Res. **6**, 216–233 (2013)
129. T. Ghosh, C. Biswas, J.S. Oh, G. Arabale, T.S. Hwang, L. Nguyen Dang et al., Solution-processed graphite membrane from reassembled graphene oxide. Chem. Mater. **24**, 594–599 (2012)
130. Y. Almog, J. Klein, Interactions between mica surfaces in a polystyrene-cyclopentane solution near the theta-temperature. J. Colloid Interface Sci. **106**, 33–44 (1985)
131. P. Alexandridis, T.A. Hatton, Poly(ethylene oxide)-poly(propylene oxide)-poly(ethylene oxide) block-copolymer surfactants in aqueous-solutions and at interfaces—thermodynamics, structure, dynamics, and modeling. Colloids Surfaces A Physicochem. Eng. Aspects **96**, 1–46 (1995)
132. K.W. Ebagninin, A. Benchabane, K. Bekkour, Rheological characterization of poly(ethylene oxide) solutions of different molecular weights. J. Colloid Interface Sci. **336**, 360–367 (2009)
133. I. Bihannic, C. Baravian, J.F.L. Duval, E. Paineau, F. Meneau, P. Levitz et al., Orientational order of colloidal disk-shaped particles under shear-flow conditions: a rheological-small-angle X-ray scattering study. J. Phys. Chem. B **114**, 16347–16355 (2010)
134. E.L. Decker, S. Garoff, Contact line structure and dynamics on surfaces with contact angle hysteresis. Langmuir **13**, 6321–6332 (1997)
135. A. Jaworek, A.T. Sobczyk, Electrospraying route to nanotechnology: An overview. J. Electrostat. **66**, 197–219 (2008)
136. M. Pal, U. Pal, Y. Gracia, J.M. Jimenez, F. Perez-Rodriguez, Effects of crystallization and dopant concentration on the emission behavior of TiO_2: Eu nanophosphors. Nanoscale Res. Lett. **7**, 1 (2012)
137. Y.N. Meng, G.Q. Xin, J.W. Nam, S.M. Cho, H.Y. Chae, Electrospray deposition of carbon nanotube thin films for flexible transparent electrodes. J. Nanosci. Nanotechnol. **13**, 6125–6129 (2013)
138. M. Mustafa, M.N. Awais, G. Pooniah, K.H. Choi, J.B. Ko, Y.H. Doh, Electrospray deposition of a graphene-oxide thin film, its characterization and investigation of its resistive switching performance. J. Korean Phys. Soc. **61**, 470–475 (2012)
139. C.K. Lee, K.W. Park, S.W. Hwang, S.B. Lee, J.K. Shim, Direct electrospray deposition of graphene onto paper and effect of binder on its surface resistance. J. Nanosci. Nanotechnol. **13**, 7108–7111 (2013)
140. M.H. Jin, T.H. Kim, S.C. Lim, D.L. Duong, H.J. Shin, Y.W. Jo et al., Facile physical route to highly crystalline graphene. Adv. Func. Mater. **21**, 3496–3501 (2011)
141. L. Song, F. Khoerunnisa, W. Gao, W.H. Dou, T. Hayashi, K. Kaneko et al., Effect of high-temperature thermal treatment on the structure and adsorption properties of reduced graphene oxide. Carbon **52**, 608–612 (2013)
142. C.M. Chen, Q.H. Yang, Y.G. Yang, W. Lv, Y.F. Wen, P.X. Hou et al., Self-assembled free-standing graphite oxide membrane. Adv. Mater. **21**, 3007–3011 (2009)
143. J.Y. Kim, L.J. Cote, F. Kim, W. Yuan, K.R. Shull, J.X. Huang, Graphene oxide sheets at interfaces. J. Am. Chem. Soc. **132**, 8180–8186 (2010)

144. L. Chen, L.L. Huang, J.H. Zhu, Stitching graphene oxide sheets into a membrane at a liquid/liquid interface. Chem. Commun. **50**, 15944–15947 (2014)
145. F. Kim, L.J. Cote, J.X. Huang, Graphene oxide: Surface activity and two-dimensional assembly. Adv. Mater. **22**, 1954–1958 (2010)
146. H. Bai, C. Li, G.Q. Shi, Functional composite materials based on chemically converted graphene. Adv. Mater. **23**, 1089–1115 (2011)
147. X.J. Wan, Y. Huang, Y.S. Chen, Focusing on energy and optoelectronic applications: a journey for graphene and graphene oxide at large scale. Acc. Chem. Res. **45**, 598–607 (2012)
148. X. Huang, X.Y. Qi, F. Boey, H. Zhang, Graphene-based composites. Chem. Soc. Rev. **41**, 666–686 (2012)
149. B. Luo, S.M. Liu, L.J. Zhi, Chemical approaches toward graphene-based nanomaterials and their applications in energy-related areas. Small **8**, 630–646 (2012)
150. Y.Q. Sun, Q. Wu, G.Q. Shi, Graphene based new energy materials. Energy Environ. Sci. **4**, 1113–1132 (2011)
151. W.R. Yang, K.R. Ratinac, S.P. Ringer, P. Thordarson, J.J. Gooding, F. Braet, Carbon nanomaterials in biosensors: Should you use nanotubes or graphene? Angew. Chem. Int. Ed. **49**, 2114–2138 (2010)
152. Y.X. Xu, G.Q. Shi, Assembly of chemically modified graphene: methods and applications. J. Mater. Chem. **21**, 3311–3323 (2011)
153. D. Li, R.B. Kaner, Materials science—graphene-based materials. Science **320**, 1170–1171 (2008)
154. D. Li, M.B. Mueller, S. Gilje, R.B. Kaner, G.G. Wallace, Processable aqueous dispersions of graphene nanosheets. Nat. Nanotechnol. **3**, 101–105 (2008)
155. H. Bai, C. Li, X.L. Wang, G.Q. Shi, A pH-sensitive graphene oxide composite hydrogel. Chem. Commun. **46**, 2376–2378 (2010)
156. Y.X. Xu, Q. Wu, Y.Q. Sun, H. Bai, G.Q. Shi, Three-dimensional self-assembly of graphene oxide and DNA into multifunctional hydrogels. ACS Nano **4**, 7358–7362 (2010)
157. H. Bai, C. Li, X.L. Wang, G.Q. Shi, On the gelation of graphene oxide. J. Phys. Chem. C **115**, 5545–5551 (2011)
158. C.C. Huang, H. Bai, C. Li, G.Q. Shi, A graphene oxide/hemoglobin composite hydrogel for enzymatic catalysis in organic solvents. Chem. Commun. **47**, 4962–4964 (2011)
159. O.C. Compton, Z. An, K.W. Putz, B.J. Hong, B.G. Hauser, L.C. Brinson et al., Additive-free hydrogelation of graphene oxide by ultrasonication. Carbon **50**, 3399–3406 (2012)
160. A. Sahu, W.I. Choi, G.Y. Tae, A stimuli-sensitive injectable graphene oxide composite hydrogel. Chem. Commun. **48**, 5820–5822 (2012)
161. J. Zhang, Y.W. Cao, J.C. Feng, P.Y. Wu, Graphene-oxide-sheet-induced gelation of cellulose and promoted mechanical properties of composite aerogels. J. Phys. Chem. C **116**, 8063–8068 (2012)
162. X. Wang, L.L. Lu, Z.L. Yu, X.W. Xu, Y.R. Zheng, S.H. Yu, Scalable template synthesis of resorcinol-formaldehyde/graphene oxide composite aerogels with tunable densities and mechanical properties. Angew. Chem. Int. Ed. **54**, 2397–2401 (2015)
163. D.R. Dreyer, S. Park, C.W. Bielawski, R.S. Ruoff, The chemistry of graphene oxide. Chem. Soc. Rev. **39**, 228–240 (2010)
164. Y.R. Lin, G.J. Ehlert, C. Bukowsky, H.A. Sodano, Superhydrophobic functionalized graphene aerogels. ACS Appl. Mater. Interfaces **3**, 2200–2203 (2011)
165. N. Mohanty, V. Berry, Graphene-based single-bacterium resolution biodevice and DNA transistor: interfacing graphene derivatives with nanoscale and microscale biocomponents. Nano Lett. **8**, 4469–4476 (2008)
166. A.J. Patil, J.L. Vickery, T.B. Scott, S. Mann, Aqueous stabilization and self-assembly of graphene sheets into layered bio-nanocomposites using DNA. Adv. Mater. **21**, 3159–3164 (2009)

167. S.J. He, B. Song, D. Li, C.F. Zhu, W.P. Qi, Y.Q. Wen et al., A graphene nanoprobe for rapid, sensitive, and multicolor fluorescent DNA analysis. Adv. Func. Mater. **20**, 453–459 (2010)
168. H. Hu, Z.B. Zhao, W.B. Wan, Y. Gogotsi, J.S. Qiu, Ultralight and highly compressible graphene aerogels. Adv. Mater. **25**, 2219–2223 (2013)
169. Q.L. Fang, B.L. Chen, Self-assembly of graphene oxide aerogels by layered double hydroxides cross-linking and their application in water purification. J. Mater. Chem. A **2**, 8941–8951 (2014)
170. G.L. Fan, F. Li, D.G. Evans, X.F. Duan, Catalytic applications of layered double hydroxides: recent advances and perspectives. Chem. Soc. Rev. **43**, 7040–7066 (2014)
171. C.M. Li, M. Wei, D.G. Evans, X.F. Duan, Layered double hydroxide-based nanomaterials as highly efficient catalysts and adsorbents. Small **10**, 4469–4486 (2014)
172. Li W, Yan D, Gao R, Lu J, Wei M, Duan X. Recent advances in stimuli-responsive photofunctional materials based on accommodation of chromophore into layered double hydroxide nanogallery. J. Nanomaterials. 2013:586462
173. J. Qu, Q.W. Zhang, X.W. Li, X.M. He, S.X. Song, Mechanochemical approaches to synthesize layered double hydroxides: a review. Appl. Clay Sci. **119**, 185–192 (2016)
174. Q. Wang, D. O'Hare, Recent advances in the synthesis and application of layered double hydroxide (LDH) nanosheets. Chem. Rev. **112**, 4124–4155 (2012)
175. K. Zhang, Z.P. Xu, J. Lu, Z.Y. Tang, H.J. Zhao, D.A. Good et al., Potential for layered double hydroxides-based, innovative drug delivery systems. Int. J. Mol. Sci. **15**, 7409–7428 (2014)
176. X.L. Wang, H. Bai, G.Q. Shi, Size fractionation of graphene oxide sheets by pH-assisted selective sedimentation. J. Am. Chem. Soc. **133**, 6338–6342 (2011)
177. F. Liu, T.S. Seo, A controllable self-assembly method for large-scale synthesis of graphene sponges and free-standing graphene films. Adv. Func. Mater. **20**, 1930–1936 (2010)
178. J.Y. Cao, Y.M. Wang, P. Xiao, Y.C. Chen, Y. Zhou, J.H. Ouyang et al., Hollow graphene spheres self-assembled from graphene oxide sheets by a one-step hydrothermal process. Carbon **56**, 389–391 (2013)
179. Z.H. Tang, S.L. Shen, J. Zhuang, X. Wang, Noble-metal-promoted three-dimensional macroassembly of single-layered graphene oxide. Angew. Chem. Int. Ed. **49**, 4603–4607 (2010)
180. Y.Q. Sun, Q. Wu, G.Q. Shi, Supercapacitors based on self-assembled graphene organogel. Phys. Chem. Chem. Phys. **13**, 17249–17254 (2011)
181. J.P. Zhao, W.C. Ren, H.M. Cheng, Graphene sponge for efficient and repeatable adsorption and desorption of water contaminations. J. Mater. Chem. **22**, 20197–20202 (2012)
182. X.X. Sun, P. Cheng, H.J. Wang, H. Xu, L.Q. Dang, Z.H. Liu et al., Activation of graphene aerogel with phosphoric acid for enhanced electrocapacitive performance. Carbon **92**, 1–10 (2015)
183. W.J. Liu, Y.K. Wang, Z.H. Li, Tuning of surface wettability of RGO-based aerogels for various adsorbates in water using different amino acids. Chem. Commun. **50**, 10311–10314 (2014)
184. K.X. Sheng, Y.X. Xu, C. Li, G.Q. Shi, High-performance self-assembled graphene hydrogels prepared by chemical reduction of graphene oxide. New Carbon Mater. **26**, 9–15 (2011)
185. X. Zhang, Z.Y. Sui, B. Xu, S.F. Yue, Y.J. Luo, W.C. Zhan et al., Mechanically strong and highly conductive graphene aerogel and its use as electrodes for electrochemical power sources. J. Mater. Chem. **21**, 6494–6497 (2011)
186. P. Hai Dinh, P. Viet Hung, C. Tran Viet, N.P. Thuy-Duong, J.S. Chung, E.W. Shin et al., Synthesis of the chemically converted graphene xerogel with superior electrical conductivity. Chem. Commun. **47**, 9672–9674 (2011)
187. W.F. Chen, L.F. Yan, In situ self-assembly of mild chemical reduction graphene for three-dimensional architectures. Nanoscale **3**, 3132–3137 (2011)

188. W.F. Chen, S.R. Li, C.H. Chen, L.F. Yan, Self-assembly and embedding of nanoparticles by in situ reduced graphene for preparation of a 3D graphene/nanoparticle aerogel. Adv. Mater. **23**, 5679–5683 (2011)
189. W.F. Chen, L.F. Yan, P.R. Bangal, Chemical reduction of graphene oxide to graphene by sulfur-containing compounds. J. Phys. Chem. C **114**, 19885–19890 (2010)
190. H.P. Cong, X.C. Ren, P. Wang, S.H. Yu, Macroscopic multifunctional graphene-based hydrogels and aerogels by a metal ion induced self-assembly process. ACS Nano **6**, 2693–2703 (2012)
191. X.W. Yang, J.W. Zhu, L. Qiu, D. Li, Bioinspired effective prevention of restacking in multilayered graphene films: towards the next generation of high-performance supercapacitors. Adv. Mater. **23**, 2833–2838 (2011)
192. S.H. Lee, H.W. Kim, J.O. Hwang, W.J. Lee, J. Kwon, C.W. Bielawski et al., Three-dimensional self-assembly of graphene oxide platelets into mechanically flexible macroporous carbon films. Angew. Chem. International Ed. **49**, 10084–10088 (2010)
193. N. Ayres, Atom transfer radical polymerization: a robust and versatile route for polymer synthesis. Polym. Rev. **51**, 138–162 (2011)
194. K. Matyjaszewski, Atom transfer radical polymerization: From mechanisms to applications. Isr. J. Chem. **52**, 206–220 (2012)
195. K. Matyjaszewski, J.H. Xia, Atom transfer radical polymerization. Chem. Rev. **101**, 2921–2990 (2001)
196. S. Stankovich, D.A. Dikin, R.D. Piner, K.A. Kohlhaas, A. Kleinhammes, Y.Y. Jia et al., Synthesis of graphene-based nanosheets via chemical reduction of exfoliated graphite oxide. Carbon **45**, 1558–1565 (2007)
197. S.J. An, Y.W. Zhu, S.H. Lee, M.D. Stoller, T. Emilsson, S.J. Park et al., Thin film fabrication and simultaneous anodic reduction of deposited graphene oxide platelets by electrophoretic deposition. J. Phys. Chem. Lett. **1**, 1259–1263 (2010)
198. X.F. Gao, J. Jang, S. Nagase, Hydrazine and thermal reduction of graphene oxide: reaction mechanisms, product dtructures, and reaction design. J. Phys. Chem. C **114**, 832–842 (2010)
199. Y.W. Zhu, S. Murali, M.D. Stoller, K.J. Ganesh, W.W. Cai, P.J. Ferreira et al., Carbon-based supercapacitors produced by activation of graphene. Science **332**, 1537–1541 (2011)
200. L.L. Zhang, X. Zhao, M.D. Stoller, Y.W. Zhu, H.X. Ji, S. Murali et al., Highly conductive and porous activated reduced graphene oxide films for high-power supercapacitors. Nano Lett. **12**, 1806–1812 (2012)
201. J.L. Vickery, A.J. Patil, S. Mann, Fabrication of graphene-polymer nanocomposites with higher-order three-dimensional architectures. Adv. Mater. **21**, 2180–2184 (2009)
202. Z.P. Chen, W.C. Ren, L.B. Gao, B.L. Liu, S.F. Pei, H.M. Cheng, Three-dimensional flexible and conductive interconnected graphene networks grown by chemical vapour deposition. Nat. Mater. **10**, 424–428 (2011)
203. L. Estevez, A. Kelarakis, Q.M. Gong, E.H. Da'as, E.P. Giannelis, Multifunctional graphene/platinum/nafion hybrids via ice templating. J. Am. Chem. Soc. **133**, 6122–6125 (2011)
204. B.G. Choi, M. Yang, W.H. Hong, J.W. Choi, Y.S. Huh, 3D macroporous graphene frameworks for supercapacitors with high energy and power densities. ACS Nano **6**, 4020–4028 (2012)
205. H.M. Sun, L.Y. Cao, L.H. Lu, Bacteria promoted hierarchical carbon materials for high-performance supercapacitor. Energy Environ. Sci. **5**, 6206–6213 (2012)
206. X.Y. Xiao, T.E. Beechem, M.T. Brumbach, T.N. Lambert, D.J. Davis, J.R. Michael et al., Lithographically defined three-dimensional graphene structures. ACS Nano **6**, 3573–3579 (2012)
207. M. Batzill, The surface science of graphene: metal interfaces, CVD synthesis, nanoribbons, chemical modifications, and defects. Surf. Sci. Rep. **67**, 83–115 (2012)

208. P.L. Huang, S.C. Lin, C.Y. Yeh, H.H. Kuo, S.H. Huang, G.R. Lin et al., Stable mode-locked fiber laser based on CVD fabricated graphene saturable absorber. Opt. Express **20**, 2460–2465 (2012)
209. E. Kibena, M. Mooste, J. Kozlova, M. Marandi, V. Sammelselg, K. Tammeveski, Surface and electrochemical characterisation of CVD grown graphene sheets. Electrochem. Commun. **35**, 26–29 (2013)
210. J.R. Kyle, A. Guvenc, W. Wang, M. Ghazinejad, J. Lin, S.R. Guo et al., Centimeter-scale high-resolution metrology of entire CVD-grown graphene sheets. Small **7**, 2599–2606 (2011)
211. R. Munoz, C. Gomez-Aleixandre, Review of CVD synthesis of graphene. Chem. Vap. Deposition **19**, 297–322 (2013)
212. A.W. Tsen, L. Brown, R.W. Havener, J. Park, Polycrystallinity and stacking in CVD graphene. Acc. Chem. Res. **46**, 2286–2296 (2013)
213. T. Yamada, J. Kim, M. Ishihara, M. Hasegawa, Low-temperature graphene synthesis using microwave plasma CVD. J. Phys. D-Appl. Phys. **46**, 063001 (2013)
214. W.L. Li, K. Lu, J.Y. Walz, Freeze casting of porous materials: review of critical factors in microstructure evolution. Int. Mater. Rev. **57**, 37–60 (2012)
215. S. Deville, Ice-templating, freeze casting: Beyond materials processing. J. Mater. Res. **28**, 2202–2219 (2013)
216. V. Medri, D. Sciti, D.D. Fabbriche, A. Piancastelli, E. Landi, Ice templating of ZrB_2–SiC systems. Ceram. Int. **41**, 10324–10330 (2015)
217. E. Papa, V. Medri, P. Benito, A. Vaccari, S. Bugani, J. Jaroszewicz et al., Synthesis of porous hierarchical geopolymer monoliths by ice-templating. Microporous Mesoporous Mater. **215**, 206–214 (2015)
218. S. Deville, E. Saiz, A.P. Tomsia, Ice-templated porous alumina structures. Acta Mater. **55**, 1965–1974 (2007)
219. M.C. Gutierrez, M.L. Ferrer, F. del Monte, Ice-templated materials: sophisticated structures exhibiting enhanced functionalities obtained after unidirectional freezing and ice-segregation-induced self-assembly. Chem. Mater. **20**, 634–648 (2008)
220. M. Kota, X. Yu, S.H. Yeon, H.W. Cheong, H.S. Park, Ice-templated three dimensional nitrogen doped graphene for enhanced supercapacitor performance. J. Power Sources **303**, 372–378 (2016)
221. K.H. Lee, Y.W. Lee, S.W. Lee, J.S. Ha, S.S. Lee, J.G. Son, Ice-templated self-assembly of $VOPO_4$-graphene nanocomposites for vertically porous 3D supercapacitor electrodes. Sci. Rep. **5**, 13696 (2015)
222. J.A. Slotwinski, E.J. Garboczi, Metrology needs for metal additive manufacturing powders. JOM **67**, 538–543 (2015)
223. J. Deckers, J. Vleugels, J.P. Kruthl, Additive manufacturing of ceramics: a review. J. Ceram. Sci. Technol. **5**, 245–260 (2014)
224. S.M. Giannitelli, P. Mozetic, M. Trombetta, A. Rainer, Combined additive manufacturing approaches in tissue engineering. Acta Biomater. **24**, 1–11 (2015)
225. R. Gmeiner, U. Deisinger, J. Schoenherr, B. Lechner, R. Detsch, A.R. Boccaccini et al., Additive manufacturing of bioactive glasses and silicate bioceramics. J. Ceram. Sci. Technol. **6**, 75–86 (2015)
226. A.R. Studart, Additive manufacturing of biologically-inspired materials. Chem. Soc. Rev. **45**, 359–376 (2016)
227. N. Travitzky, A. Bonet, B. Dermeik, T. Fey, I. Filbert-Demut, L. Schlier et al., Additive manufacturing of ceramic-based materials. Adv. Eng. Mater. **16**, 729–754 (2014)
228. S. Yang, Y.Y.F. Zhao, Additive manufacturing-enabled design theory and methodology: a critical review. Int. J. Adv. Manuf. Technol. **80**, 327–342 (2015)
229. J.H. Kim, W.S. Chang, D.H. Kim, J.R. Yang, J.T. Han, G.W. Lee et al., 3D printing of reduced graphene oxide nanowires. Adv. Mater. **27**, 157–161 (2015)
230. D. Lin, S.Y. Jin, F. Zhang, C. Wang, Y.Q. Wang, C. Zhou, et al. 3D stereolithography printing of graphene oxide reinforced complex architectures. Nanotechnology. 2015; 26

231. Z.X. Yang, C.Z. Yan, J.H. Liu, S. Chabi, Y.D. Xia, Y.Q. Zhu, Designing 3D graphene networks via a 3D-printed Ni template. RSC Adv. **5**, 29397–29400 (2015)
232. A.E. Jakus, E.B. Secor, A.L. Rutz, S.W. Jordan, M.C. Hersam, R.N. Shah, Three-dimensional printing of high-content graphene scaffolds for electronic and biomedical applications. ACS Nano **9**, 4636–4648 (2015)
233. C.F. Zhu, T.Y.J. Han, E.B. Duoss, A.M. Golobic, J.D. Kuntz, C.M. Spadaccini et al., Highly compressible 3D periodic graphene aerogel microlattices. Nat. Commun. **6**, 6962 (2015)
234. S.S. Duan, K. Yang, Z.H. Wang, M.T. Chen, L. Zhang, H.B. Zhang et al., Fabrication of highly stretchable conductors based on 3D printed porous poly(dimethylsiloxane) and conductive carbon nanotubes/graphene network. ACS Appl. Mater. Interfaces **8**, 2187–2192 (2016)
235. M.A. Worsley, T.Y. Olson, J.R.I. Lee, Willey TrM, M.H. Nielsen, S.K. Roberts et al., High surface area, sp^2-cross-linked three-dimensional graphene monoliths. J. Phys. Chem. Lett. **2**, 921–925 (2011)
236. Z.A. Munir, U. Anselmi-Tamburini, M. Ohyanagi, The effect of electric field and pressure on the synthesis and consolidation of materials: A review of the spark plasma sintering method. J. Mater. Sci. **41**, 763–777 (2006)
237. E.A. Olevsky, S. Kandukuri, L. Froyen, Consolidation enhancement in spark-plasma sintering: impact of high heating rates. J. Appl. Phys. **102**, 114913 (2007)
238. N. Saheb, Z. Iqbal, A. Khalil, A.S. Hakeem, N. Al Aqeeli, T. Laoui et al. Spark plasma sintering of metals and metal matrix nanocomposites: a review. J. Nanomater. 2012:983470
239. L.J. Wang, J.F. Zhang, W. Jiang, Recent development in reactive synthesis of nanostructured bulk materials by spark plasma sintering. Int. J. Refract Metal Hard Mater. **39**, 103–112 (2013)
240. M.S. Yurlova, V.D. Demenyuk, L.Y. Lebedeva, D.V. Dudina, E.G. Grigoryev, E.A. Olevsky, Electric pulse consolidation: an alternative to spark plasma sintering. J. Mater. Sci. **49**, 952–985 (2014)
241. K. Lu, Sintering of nanoceramics. Int. Mater. Rev. **53**, 21–38 (2008)
242. T. He, J.L. Li, L.J. Wang, J.J. Zhu, W. Jiang, Preparation and consolidation of alumina/graphene composite powders. Mater. Trans. **50**, 749–751 (2009)
243. K. Wang, Y.F. Wang, Z.J. Fan, J. Yan, T. Wei, Preparation of graphene nanosheet/alumina composites by spark plasma sintering. Mater. Res. Bull. **46**, 315–318 (2011)
244. Y.C. Fan, L.J. Wang, J.L. Li, J.Q. Li, S.K. Sun, F. Chen et al., Preparation and electrical properties of graphene nanosheet/Al_2O_3 composites. Carbon **48**, 1743–1749 (2010)
245. L.S. Walker, V.R. Marotto, M.A. Rafiee, N. Koratkar, E.L. Corral, Toughening in graphene ceramic composites. ACS Nano **5**, 3182–3190 (2011)
246. A. Nieto, D. Lahiri, A. Agarwal, Synthesis and properties of bulk graphene nanoplatelets consolidated by spark plasma sintering. Carbon **50**, 4068–4077 (2012)
247. B. Apak, F.C. Sahin, C-CNT produced by spark plasma sintering. Acta Phys. Pol. A **127**, 1029–1031 (2015)
248. J.L. Li, G.Z. Bai, J.W. Feng, W. Jiang, Microstructure and mechanical properties of hot-pressed carbon nanotubes compacted by spark plasma sintering. Carbon **43**, 2649–2653 (2005)
249. Y. Sato, H. Nishizaka, S. Sawano, A. Yoshinaka, K. Hirano, S. Hashiguchi et al., Influence of the structure of the nanotube on the mechanical properties of binder-free multi-walled carbon nanotube solids. Carbon **50**, 34–39 (2012)
250. G. Yamamoto, Y. Sato, T. Takahashi, M. Omori, T. Hashida, A. Okubo et al., Single-walled carbon nanotube-derived novel structural material. J. Mater. Res. **21**, 1537–1542 (2006)